Theses and Dissertations

2016

Delineation Of The Lower Permian Gas Sand Via Calibrated Avo And Pre-Stack Seismic Inversions In Majhol Field, Saudi Arabia

Abdullah Alhashel
University of South Carolina

Follow this and additional works at: https://scholarcommons.sc.edu/etd

Part of the Geology Commons

DELINEATION OF THE LOWER PERMIAN GAS SAND VIA CALIBRATED AVO AND
PRE-STACK SEISMIC INVERSIONS IN MAJHOL FIELD, SAUDI ARABIA

by

Abdullah Alhashel

Bachelor of Geological Sciences
University of Tulsa, 2008

_____

Submitted in Partial Fulfillment of the Requirements

For the Degree of Master of Science in

Geological Sciences

College of Arts and Sciences

University of South Carolina

2016

Accepted by:

Camelia Knapp, Director of Thesis

James Kellogg, Reader

James Knapp, Reader

Cheryl L. Addy, Vice Provost and Dean of the Graduate School

DEDICATION

First I dedicate my thesis to my parents, for their love and support throughout my life. Thank you both for giving me strength to reach for the stars and chase my dreams. I also dedicate this work to my wife Norah. Without her love, support, patience and understanding this work would have never been completed. I would also like to dedicate this work to all my family, friends, and everyone helps me in the past two years specially My thesis committee, Dr. Camelia Knapp, Dr. James Knapp, and Dr. James Kellogg.

ACKNOWLEDGEMENTS

ABSTRACT

The lower Permian formation in the central region of Saudi Arabia is a key hydrocarbon siliciclastic reservoir. However, in Majhol field, the reservoir properties vary laterally due to diagenesis and facies changes. Conventional seismic interpretation has failed to map the heterogeneities of the reservoir properties that control the gas production of this field. Therefore, there was an opportunity to employ more advanced quantitative seismic techniques to delineate the productive gas sand facies in the field.

The Majhol field was initially planned to be developed as an unconventional tight reservoir. Well-1 was drilled based on conventional seismic interpretation on the crest of a four-way dip closure structure. Well-1 produced low rate hydrocarbon gas from the Lower Permian formation and it showed a poor reservoir quality due to diagenesis that highly affected the reservoir porosity and permeability. Well-2 was drilled on the flank of the structure to delineate and develop the field as unconventional tight reservoir. However, Well-2 showed an excellent reservoir and it successfully flowed gas and condensate naturally at high rate.

Here, a 3D quantitative seismic study was performed through amplitude vs. offset (AVO) analysis and impedance inversion techniques with constraints from the well data to delineate the properties of the reservoir and detect the productive gas sands. Seismic attributes derived from this study consistently delineated the gas sand facies as

class 2 AVO anomaly. Although this study shows that the gas charged sand reservoir was thick enough to be resolved with the conventionally acquired seismic data in the vicinity of Well-2, this layer does not seem to extend laterally all the way to Well-1, therefore the differences in gas production between the two wells.

TABLE OF CONTENTS

LIST OF TABLES

LIST OF FIGURES

CHAPTER 1

INTRODUCTION AND MOTIVATION

1.1 INTRODCUTION

Majhol field is located in the central region of Saudi Arabia (Figure 1.1). Its primary target for hydrocarbon exploration is the Lower Permian formation that was deposited in semi-arid Aeolian environment. It was described from the well cores to have four lithofacies: (1) sand dunes, (2) sand sheet, (3) interdune (4) and playa. In this research, detailed seismic investigation was performed in order to delineate those facies which have influence in the reservoir quality beside the diagenesis. Pre-stack and post-stack time migrated seismic volumes are available for this research with well logs for two wells. Well-1 was drilled on the crest of a four-way dip anticlinal closure to evaluate the lower Permian formation structure at a depth of 15,015 ft (Figure 1.2). Well-1 encountered the Lower Permian sandstone reservoir, however the section was tight due to subsequent digenesis that consisted of anhydrite, clay and silica overgrowth that was obvious in core 1 and 2. The reservoir in well-1 flowed minor amounts of gas and condensate, it was poorly developed with gross reservoir of 201 ft , net reservoir of 17 ft, average porosity of 7.5 % and permeability of only 0.2 mD. On the other hand, well-2 had excellent reservoir quality even though it was drilled on the flank of the structure. It flowed gas and condensate at high rate. The reservoir at well-2 location has a gross thickness of 159 ft, net reservoir thickness of 95 ft, average porosity of 12%, and log

1

based permeability of 69.5 mD (Figure 1.3). There is a significant need of detailed 3D seismic quantitative research to help outline the good quality reservoir sandstones. A preliminary relative impedance inversion showed a variation in impedance values between well-1 and well-2 (Figure 1.4). Advance impedance inversion methods and AVO modeling and analysis with help of rock physics were conducted in this research to better assess the lower Permian formation prospect in Majhol field.

1.2 GEOLOGICAL SETTINGS

1.2.1 Introduction

The Majhol field is located in the central part of Saudi Arabia (Figure 1.1). The Paleozoic and Jurassic petroleum systems of central Saudi Arabia form two of the most prolific petroleum-producing systems in the world. Three important factors make the central Saudi Arabia holds most of the hydrocarbon reserves in the world: (1) the great areal extent of the petroleum-system elements (source, reservoir, and seal) throughout the entire central Arabian Peninsula, and (2) the superb quality of those elements, and (3) the large and gentle structural closures that were created prior to peak oil generation and migration (Pollastro, 2003).

The Majhol field is anew Paleozoic prospect with the early Permian formation as the main reservoir. The Paleozoic formation has only become prospective in Saudi Arabia since the early 1970s when gas wells were discovered in the lower Permian reservoir in the Arabian Gulf and Zagros regions. The structural traps in the central Saudi Arabia are mostly north-south trending basement-core anticlines. (Konert et al., 2001). Those basement-core structures were reactivated and evolved by four major tectonic events: (1) the late Devonian Hercynian orogeny, (2) the Early Triassic Zagros rifting, (3)

2

the Pliocene 1st Alpine Orogeny, and (4) Oligocene 2nd Alpine Orogeny (Konert et al., 2001).

1.2.2 Main Tectonic Events and Features:

(1) Precambrian Amar collision (about 640-620 Ma)

Precambrian north-trending Amar suture collided the Arabian Peninsula at about 45°E, causing a wide and regular north- trending structure patterns as result of compression (Ziegler, 2001). A basement depth map in (Figure 1.5) shows the neighboring structures in the central of Saudi Arabia with north-, north-south trending patterns including the greater Ghawar structure, Khurais, and Qatar dome. Majhol structure also agrees with this north-south trending structure as indicated in Majhol TWT structural map (Figure 1.2). Those North-South trending anticlines stayed elevated as horsts bounded by faults after the widespread extensional collapse of the Arabian shield that followed the Amar collision between 620 and 530 Ma (Best et al., 1993).

(2) The late Devonian Hercynian orogeny (about 370-300 Ma)

The Hercynian orogeny had a great impact on the entire Arabian Peninsula. Numerous compressional phases affected the Arabian Peninsula during this period. Those compressional phases had significant changes in the Arabian basin geometry as shown in the Hercynian subcrop map in (Figure 1.6, where NE-trending basement highs are formed in the central Saudi Arabia). In addition, those compressional events caused folding and inversion in the region. The structural observations are consistent with a NW-directed principal compressive stress (Pollastro, 2003). The reverse faults around the north-trending structure are a good evident that those uplifts in central Saudi Arabia were caused by compressional stress field. The thickness and the facies variation of the

Lower Permian formation suggest that the post-Hercynian Pre-Permian erosion reduced the relief, but not completely. Many of the Hercynian faults bounding the major N-S uplifts were reactivated during the Triassic and late Cretaceous as discussed below (Senalp and Al-Duaji, 1995).

(3) The Early Triassic Zagros rifting and Opening of Neo-Tethys sea (260-240 Ma)

During the Early Triassic, a significant breaking of the Arabian-Gondwana/Iranian-Laurasia occurred and caused stretching of the Arabian plate and thermal subsidence. Thus widespread extensional faulting system were created. The opening of the Neo-Tethys Sea occurred during this period due to Zagros rifting (Figure 1.7). Earlier Hercynian structures including Majhol structure were reactivated and enhanced by those events (Pollastro, 2003).

(4) The Late Cretaceous 1st Alpine Orogeny (about 100 – 80 Ma)

Compressional stress occurred in the late cretaceous with the beginning of the Alpine Orogeny. This event caused the beginning of closing the Neo-Tethys Sea. The Hercynian structures in the central Saudi Arabia were also rejuvenated and affected during this event (Ziegler, 2001).

(5) The Second Alpine Orogeny (about 35-20 Ma)

In the middle to the late Tertiary, the second episode of the Alpine Orogeny began and caused the opening the opening of the red sea and the collision of Arabia and Eurasia (Konert et al., 2001). The collision of the Arabian plate and the Asia initiated the Zagros orogeny. The Arabian plate converged and subducted beneath Iran and caused the Arabian plate to tilt slightly to the northwest to form a series of anticlines and synclines in the Zagros Mountains. The Hercynian structures in the central Saudi Arabia were

4

influenced during this event and they were completely formed by the end of this period
(Konert et al., 2001)

1.2.3 Petroleum system and Stratigraphy of Central Saudi Arabia

(1) Early Silurian formation hot Shale (Source Rock)

In the late Ordovician the Arabian plate was in its most southerly position of about 55° south. It was characterized by the expanding of the polar glaciers across Gondwana and the western parts of Arabia (Figure 1.8). In the Early Silurian, a significant phase of global warming developed causing the seal level to rapidly rose and flooded the Arabian plate. The depositional environment during the late Silurian was dominated by shallow to open marine environment in the marginal areas while the deeper marine environment covered the inundated Arabian platform and extended southward along the subsiding intrashelf basin located in central Saud Arabia (Ziegler, 2001; Figure 1.9). Organic rich shale was preserved due to the anoxic water bottom conditions in the basin. This formed the most prolific Paleozoic source rock in the Arabian plate "the Early Silurian hot shale". (Konert et al., 2001).

(2) Early Permian formation (Reservoir)

The Lower Permian clastic deposits are the first widespread deposits following the Hercynian. The lower Permian formation rest on the Hercynian angular unconformity on older Paleozoic rocks and basement. They were partly deposited at the same time with rift tectonics along the eastern and northern margins the Arabian plate (Figure 1.10).

Generally, the Permian formation is made up of braided plain, channel fill, and Aeolian sandstones and siltstones that were deposited in semi-arid conditions (Senalp and Al-Duaji, 1995). The thickness of these clastic formations is variable due to onlap on the

5

Hercynian structures.

(3) Late Permian formation (Seal)

In the late Permian, the accommodation space increased in the Arabian Peninsula due to stretching of the Arabian crust and the formation of the Neo-Tethys Ocean along the Oman-Zagros suture. The late Permian megasequence was established as the basal sequence of continental to marine sandstones and shale (basal late Permian clastics) supplied from the west. These were followed by the deposition of widespread carbonates and anhydrites over the entire Arabian shelf in shallow marine to tidal flat environment (Figure 1.11). (Senalp and Al-Duaiji, 1995). Lateral seal is a critical risk factor in Majhol prospect, the lateral seal along the western edge of the trap relies on sealing against a predominantly north to south directed channel or paleo-wade. This paleo-wade is characterized by low acoustic impedance (Figure 1.14) interpreted as low porosity facies. A drilled well penetrated this paleo-wade in the northern field - and it showed tight siltstone and shale of Lower Permian formation equivalent.

(4) Majhol field Trap:

The Early Permian formation structural closure consists of a north-trending, four dip closure that is 39 square kilometers in areal extend with 65 feet of vertical relief. Structurally, Majhol is the southern culmination of northern structure which was proven to be a gas field. A potential stratigraphic trap in the field is based on the variation of the relative impedance map between well-1 and well-2 (Figure 1.4).

High angle faults are present on both flanks of the structure and the western one may cut above the pre-Permian unconformity (Figures 1.12 and 1.13).

6

1.3 MOTIVATION AND OBJECTIVES

Motivation:

- The high demand of gas in Saudi Arabia

- The variety of seismic impedance map between well-1 and well-2 indicate a potential structural and stratigraphic trap with heterogeneous reservoir

Objectives:

- Making detailed 3D quantitative seismic model that can be applied in similar fields.

- To extract and link the physical and elastic properties from both seismic and wells, to ultimately determine the extension of the reservoir zone and gas spot.

1.4 AVAILABLE DATA AND SOFTWARE

Available data:

3D Seismic surveys were conducted during the year of 2000. Two wells are also available with the basic logs, and six interpreted horizons. The available data for this research is summarized in Table 1.1.

Software:

Two main commercial software packages were utilized in this research. Those packages are (1) the Schlumberger's Petrel (2014) for 3-D structural seismic interpretation; (2) Hampson-Russell (HRS-10) software for well log interpretation, amplitude versus offset (AVO) modeling, AVO and AVA analysis, post-stack inversion, pre-stack and AVO inversion.

1.5 HYPOTHESIS AND METHODOLOGY

Hypothesis:

- The reservoir in Majhol field is heterogeneous due to facies and diagenesis variation

7

that control the quality of the reservoir.

- A combination of structural and stratigraphic trap is involved in Majhol field prospect.

- Petrophysically-calibrated AVO, pre-stack Seismic impedance inversion and seismic attribute analysis can outline the different stratigraphic facies and differentiate between porous and non-porous sand in the Lower Permian formation.

Methodology:

The workflow for this research went through four main phases as shown in (Figure 1.16)

Phase I: Well log interpretation and petrophysical analysis

This phase focused on well log interpretation and petrophysical analysis for determining the reservoir and calculating its properties. Two wells are available within this study area, and both of them have gamma-ray, density, neutrons, p-sonic, and shear-sonic logs.

There are essential petrophysical parameters that needed to be determined in order to identify the reservoir. Such as porosity, volume of shale, Vp/Vs, Mu-Rho and Lambda-Rho.

Phase II: AVO Modeling and analysis

(1) AVO forward modeling (Angle dependent synthetic gathers)

Forward modeling was performed to understand the AVO response differences between brine and gas saturated cases. Zoeppritz equation and Aki-Richards equations were used to create synthetic angle dependent gathers.

8

(2) AVO analysis on seismic data

By picking the amplitude in each angle of the CDP and then fit a regression line to the amplitude picks as a function of the sine of the angle squared.

(3) AVO attributes

I used Wiggin's equation to estimate the Intercept (A) and the Gradient (B) from the angle stack to use them in generating the AVO attributes and Intercept Vs Gradient cross plot (Russell, 1999)

Phase III: Impedance Inversion

Two impedance approaches were applied on the pre-stack seismic data:

(1) Elastic Impedance inversion

This approach was proposed by Patrick Connoly by inverting the range limited stacks (near and far stacks). It is based on the Aki-Richards equation. This approach showed a dramatic change in the elastic impedance responses when we inverted for elastic impedance at two different angles (Connolly, 1999).

(2) Simultaneous Inversion

This approach solves for P-impedance, S-impedance and density. This helps to differentiate between lithology, porosity and fluid effects. This approach is based on three assumptions. The first one is the linearized approximation for reflectivity holds. The second is that P and S reflectivity as a function of angle can be given by the Aki-Richards equation (Aki and Richards, 2002). The third assumption is that there is a linear relationship between the logarithm of P-Impedance, S-impedance, and density.

Lambda-Mu-Rho attribute were found from the Simultaneous inversion output. The LMR approach that was proposed by Goodway as a new AVO inversion approach.

This approach based on the Lame parameters, shear modulus, and density. (Goodway, 1997)

Phase IV: Integration/interpretation

Interpreting and integrating the different output from the AVO and the inversion by looking at the volumes and cross-plot them against each other's to help finding the good reservoir zone. Using the well logs and petrophysical evaluation to link the physical and elastic properties from the wells and the seismic.

1.6 TABLES AND FIGURES

Table 1.1: Available data for this research

Seiesmic			well logs	horizons
post-stack	Size	400 Km^2	Gamma Ray	six intrepeted horizons
	Inline	5098 to 5841	Density	
	Xline	1575 to 2182	Netrunes	
	Interval spacing	30 m	P-Sonic	
	Time	500 ms to 3500 ms	S-Sonic	
Pre-stack	angle stacks	10 degree range - 5 degree steps	Calibar	
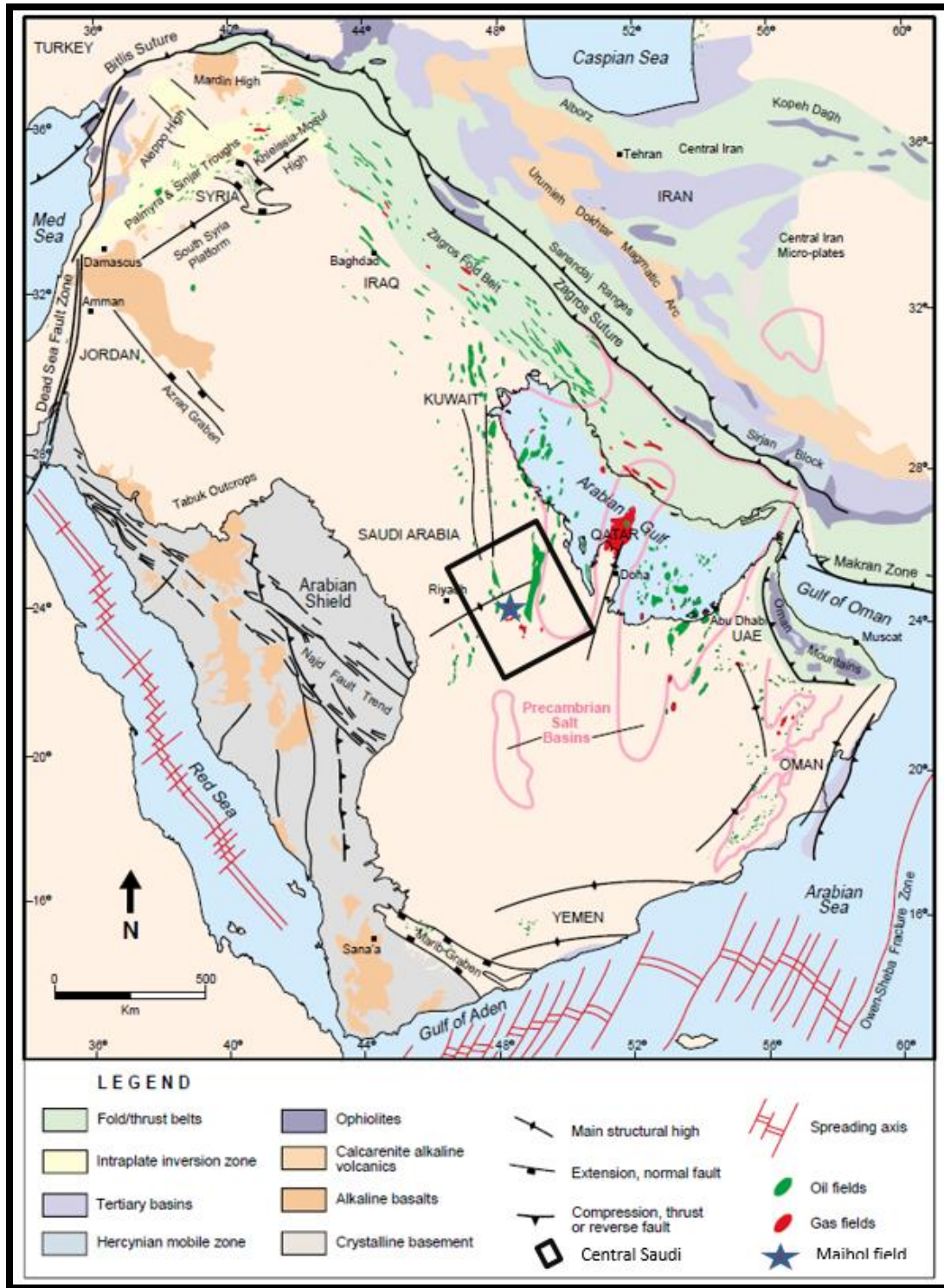
Figure 1.1: Major tectonic features of the present-day Arabian plate.
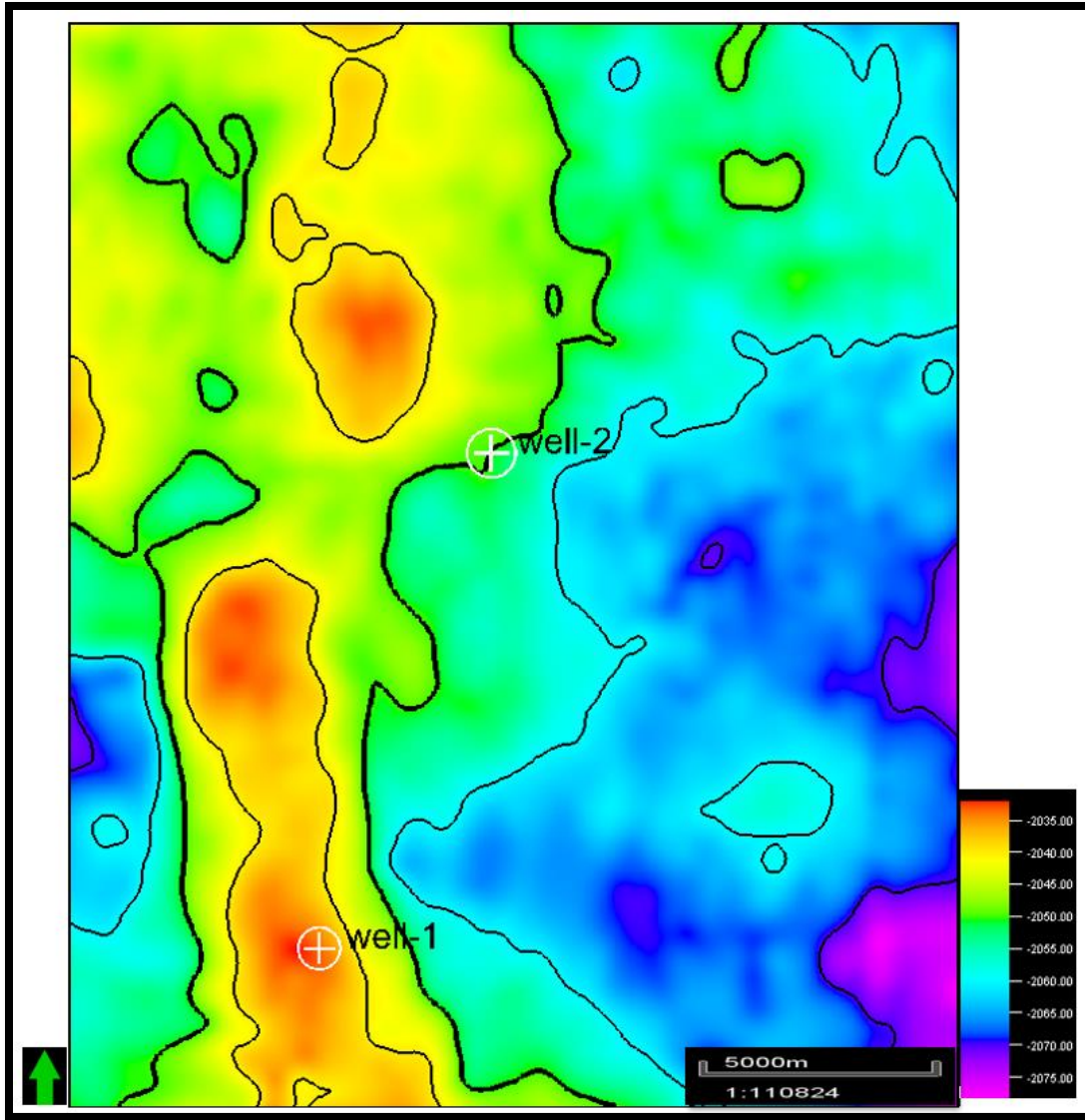
Figure 1.2: TWT Structure map of the lower Permian reservoir in Majhol field showing a N-S trending structure.
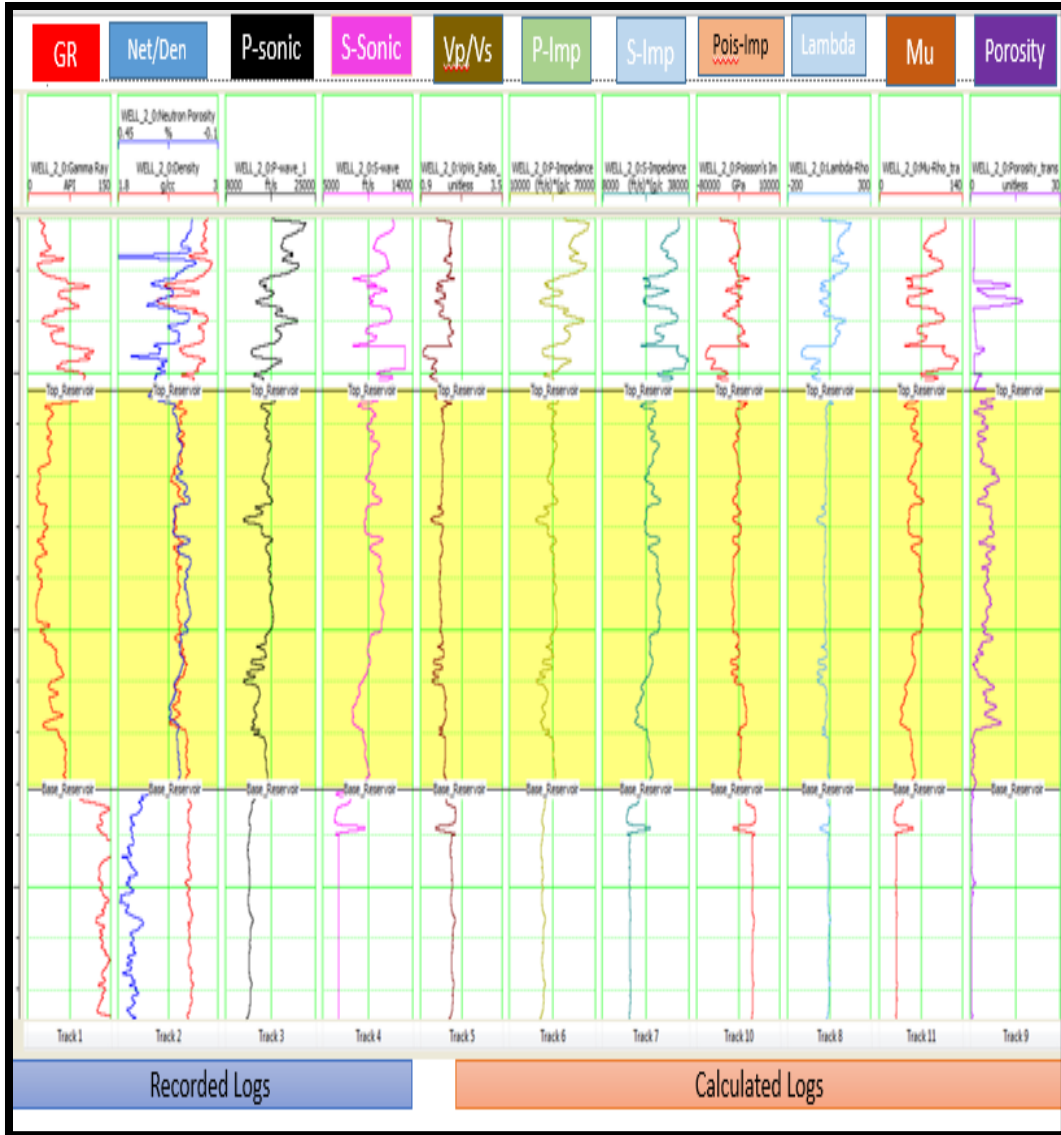
Figure 1.3: Recorded and calculated logs from well-2.
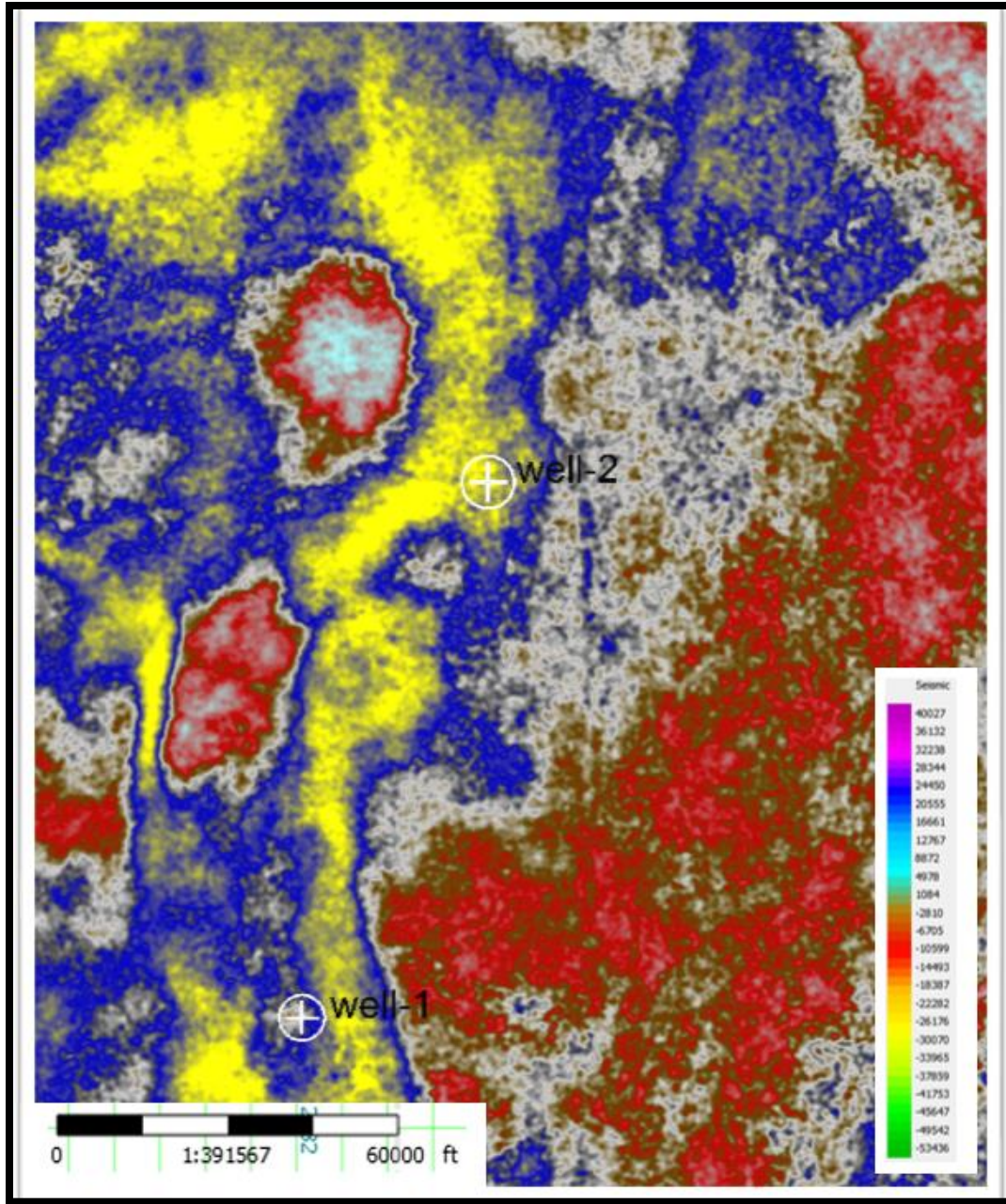
Figure 1.4: PSTM impedance horizon slice shows variation in impedance in the field.
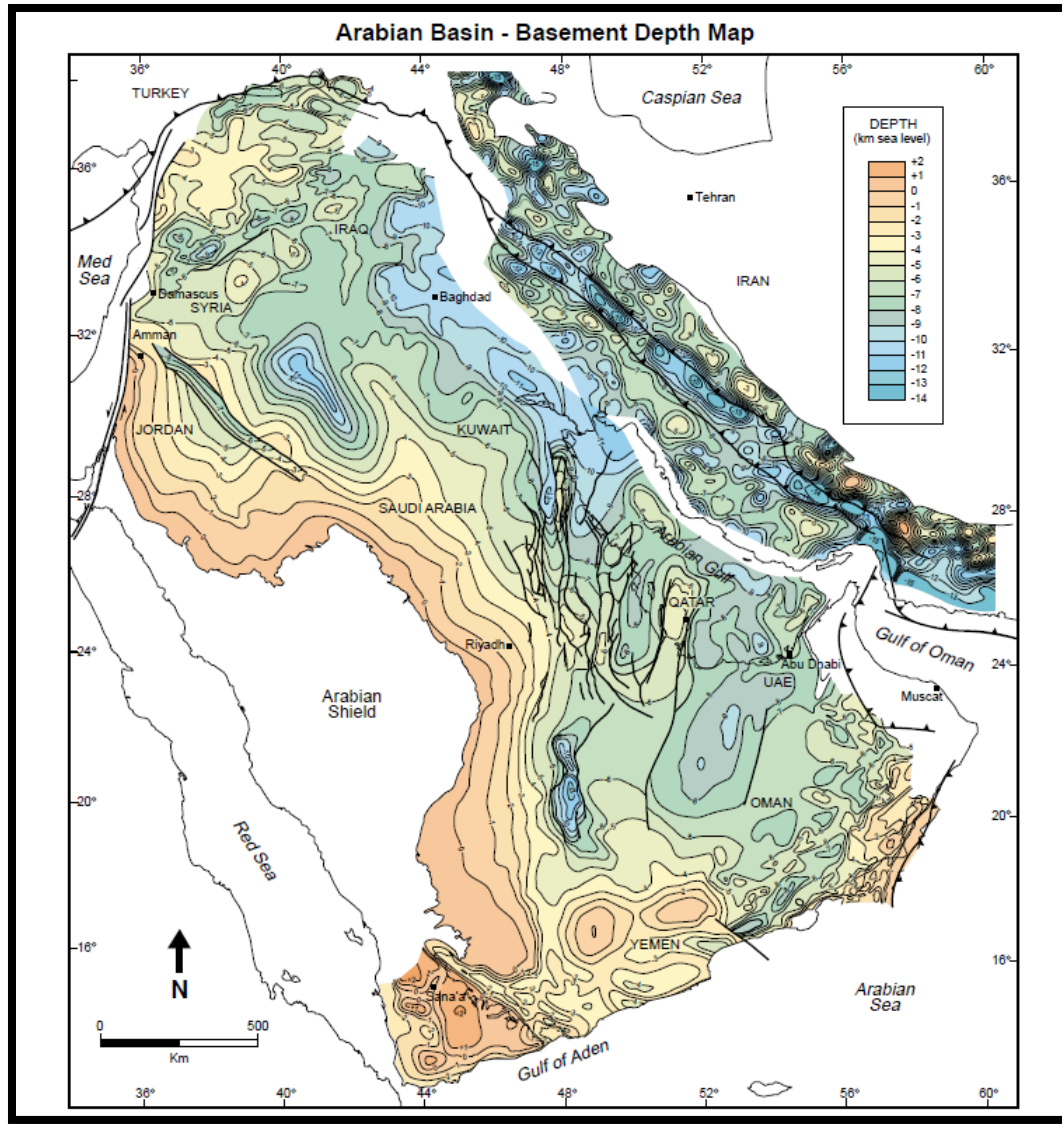
Figure 1.5: Basement depth map of the Arabian plate from published data (Best et al., 1993). The North-South trending structures in central of Saudi can be noticed.
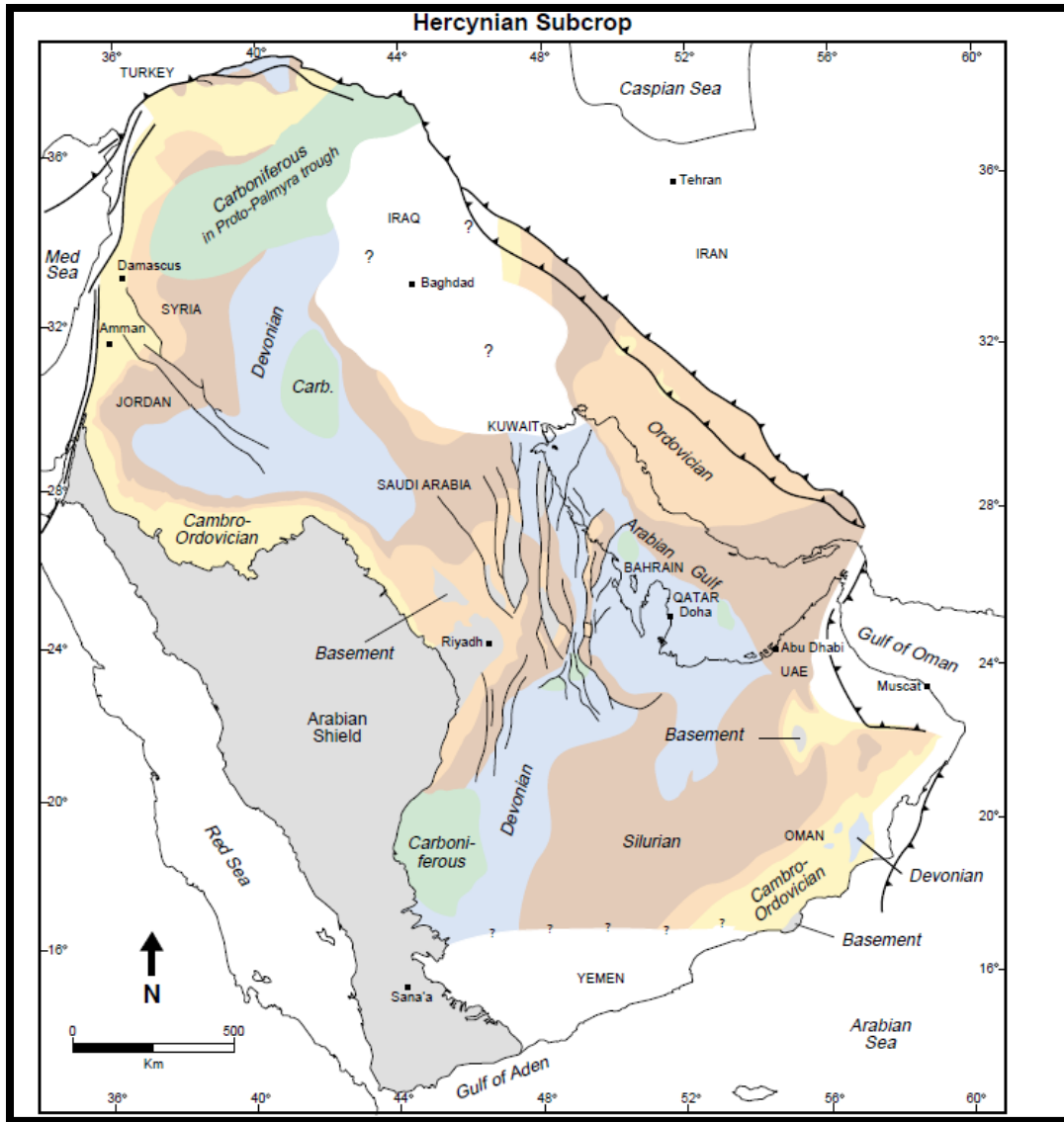
Figure 1.6: Hercynian unconformity subcrop map.
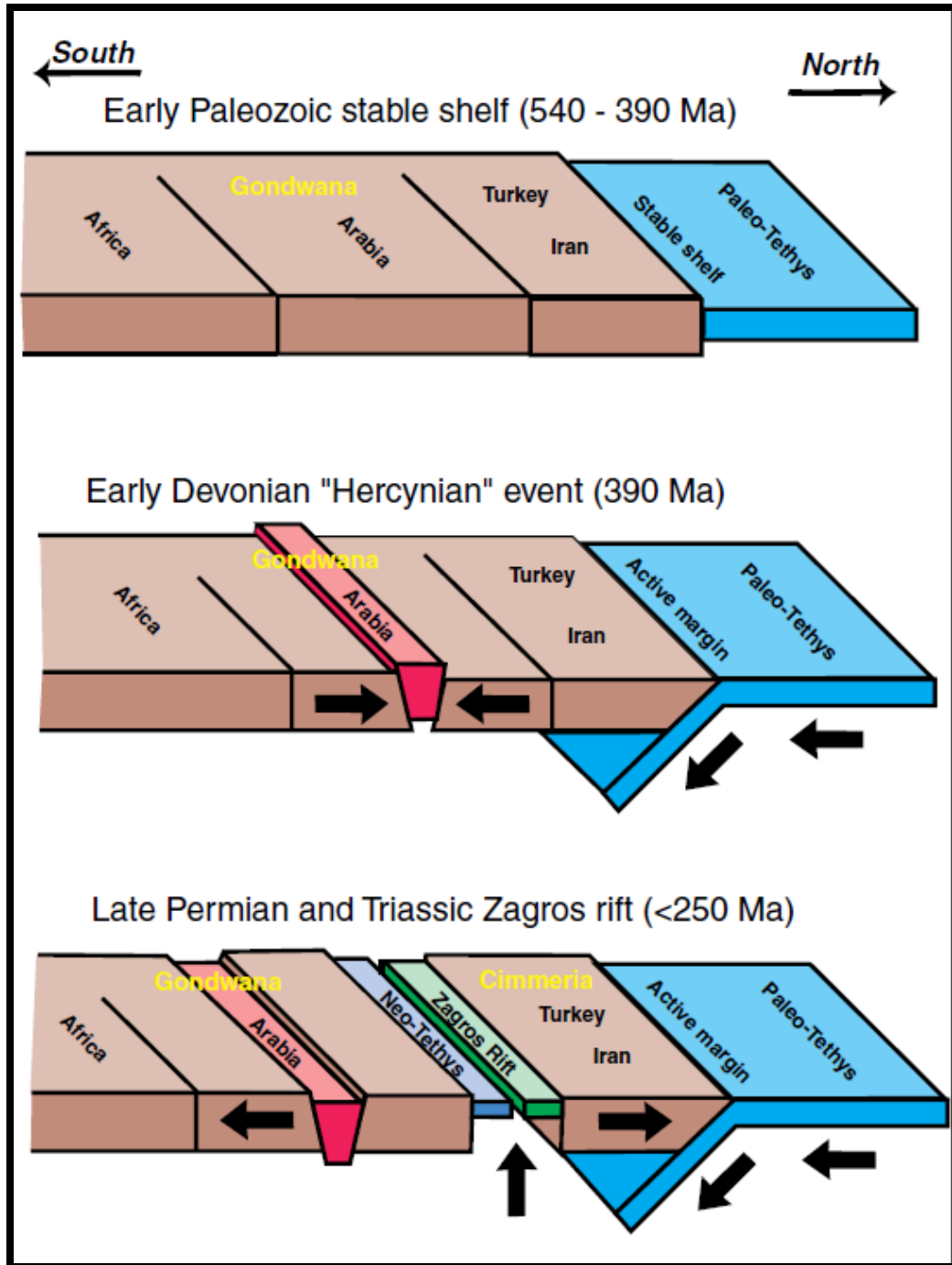
Figure 1.7: Evolution of the Arabian plate tectonics from Early Paleozoic to Late Permian and Triassic, showing the Hercynian compressional event and the Early Zagros rifting event. Modified from Pollastro (2003).
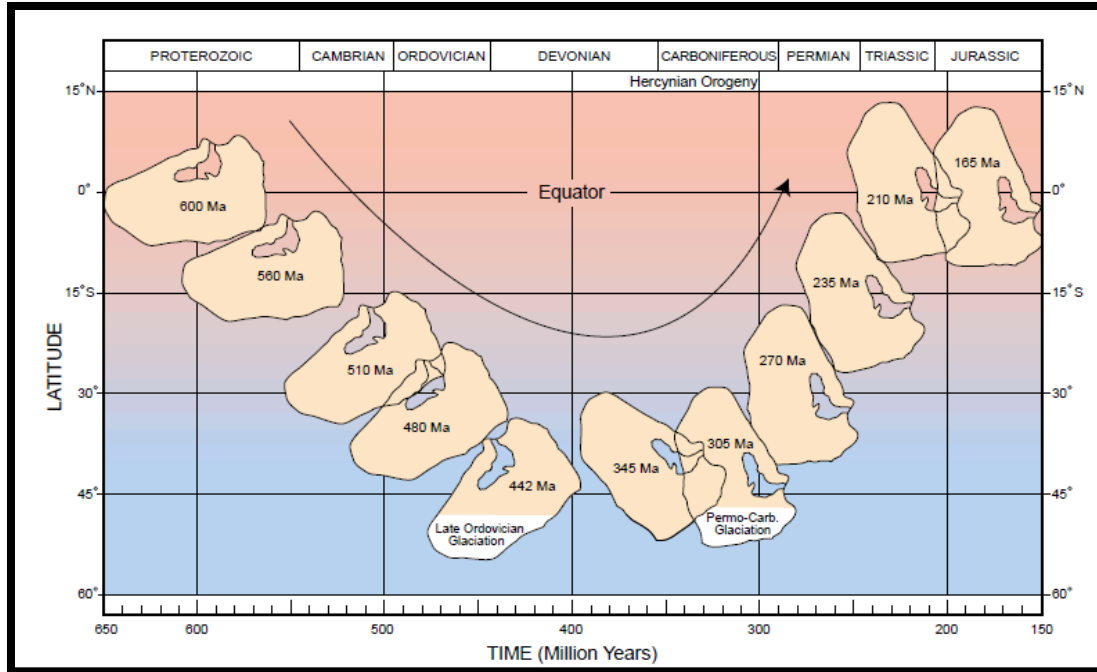
Figure 1.8: Paleolatitude position of the Arabian plate between 650 and 150 Ma.
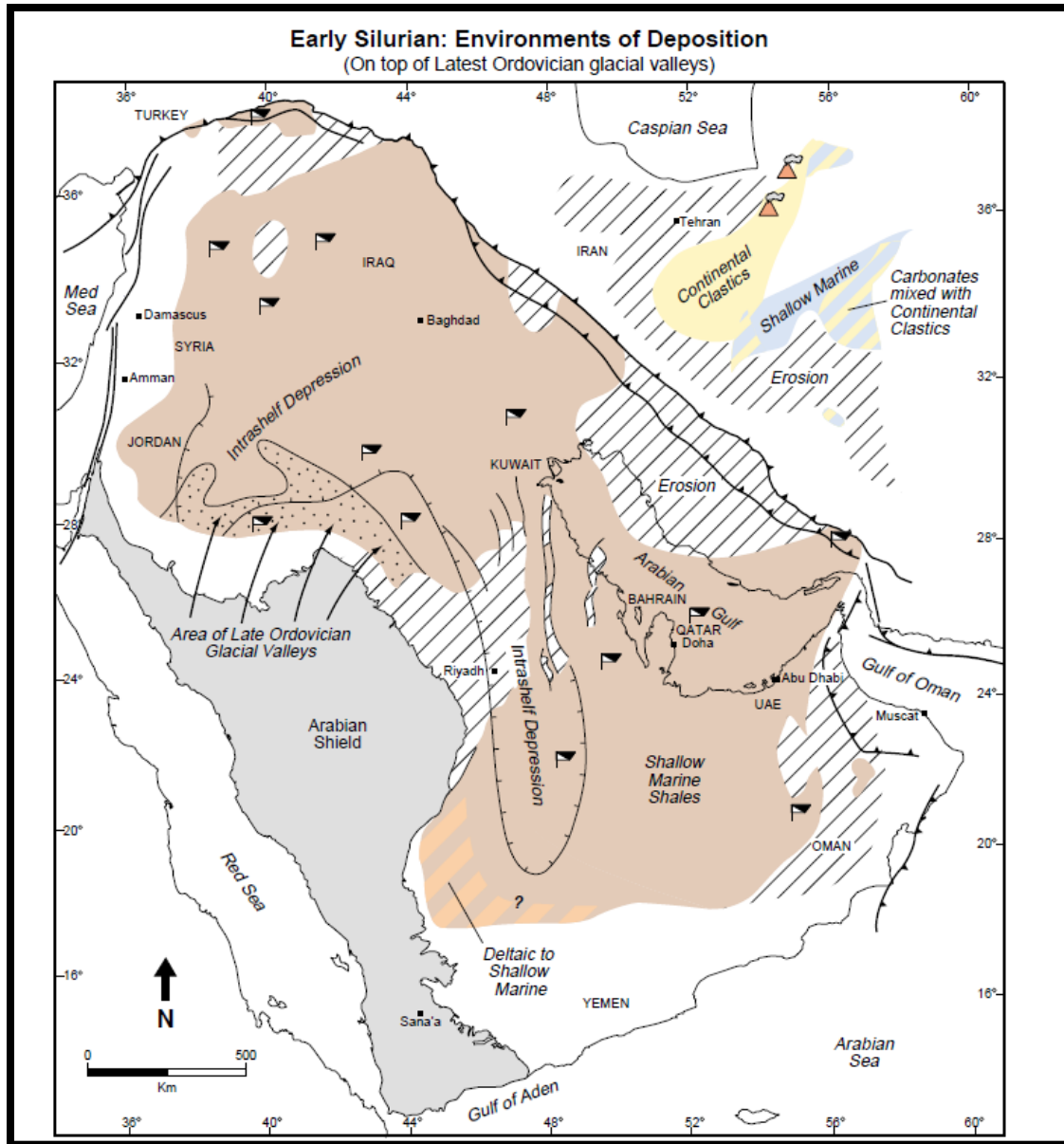
Figure 1.9: The Early Silurian Depositional environment; shallow to open marine covered the Arabian plate due to the retreat of glaciers and the rise of global sea level modified from Konert et al., (2001).
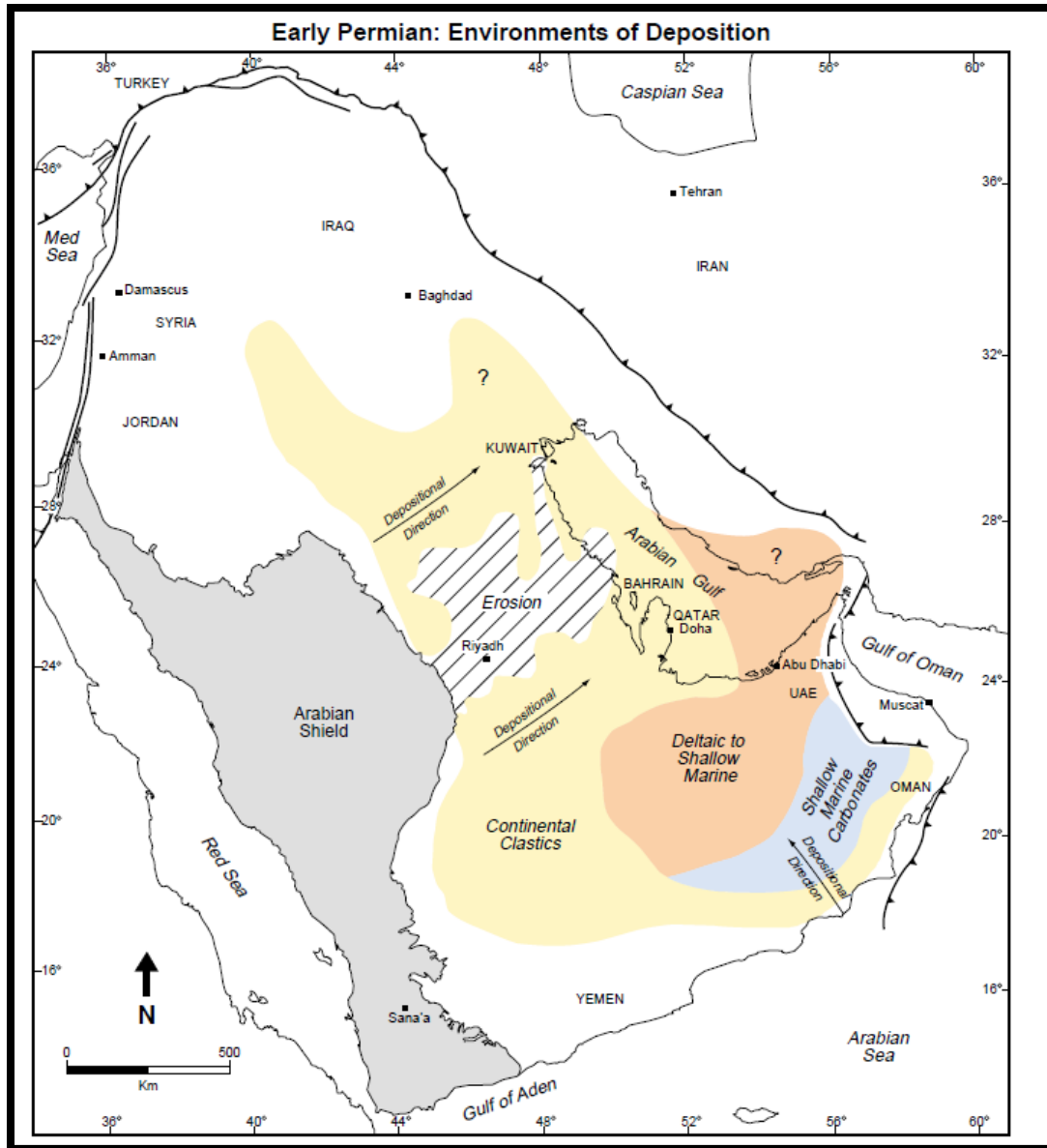
Figure 1.10: The lower Permian depositional environment.
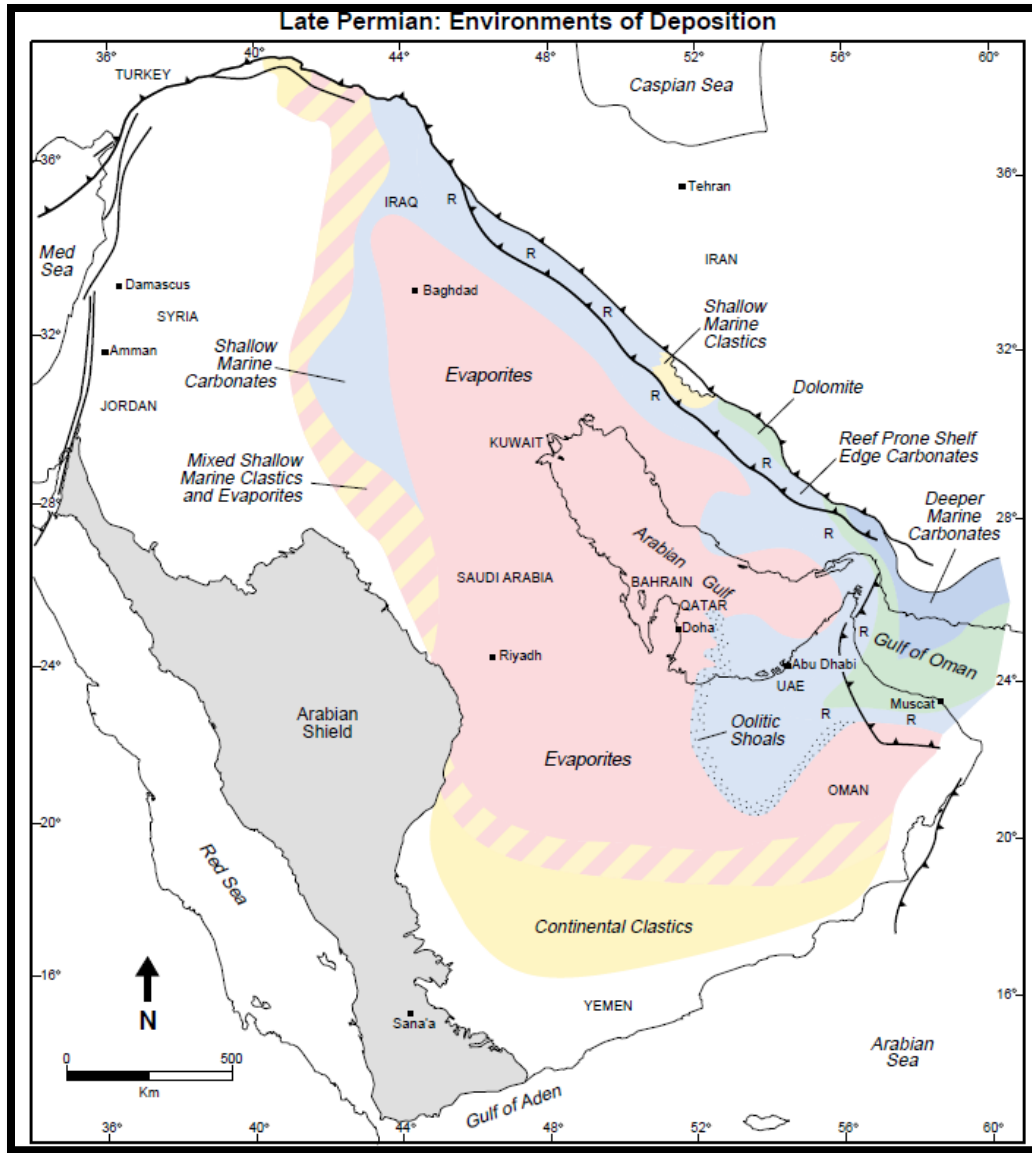
Figure 1.11: The Upper Permian depositional environment characterized by the deposition of the carbonates and anhydrites over the entire Arabian shelf in shallow marine to tidal flat environments.
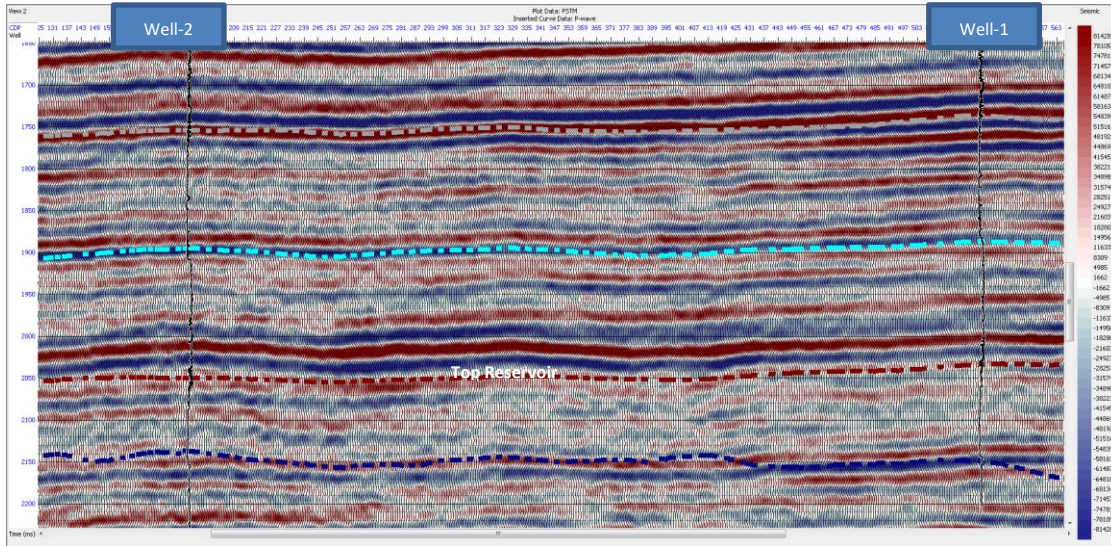
Figure 1.12: South-North composite line going through the wells.
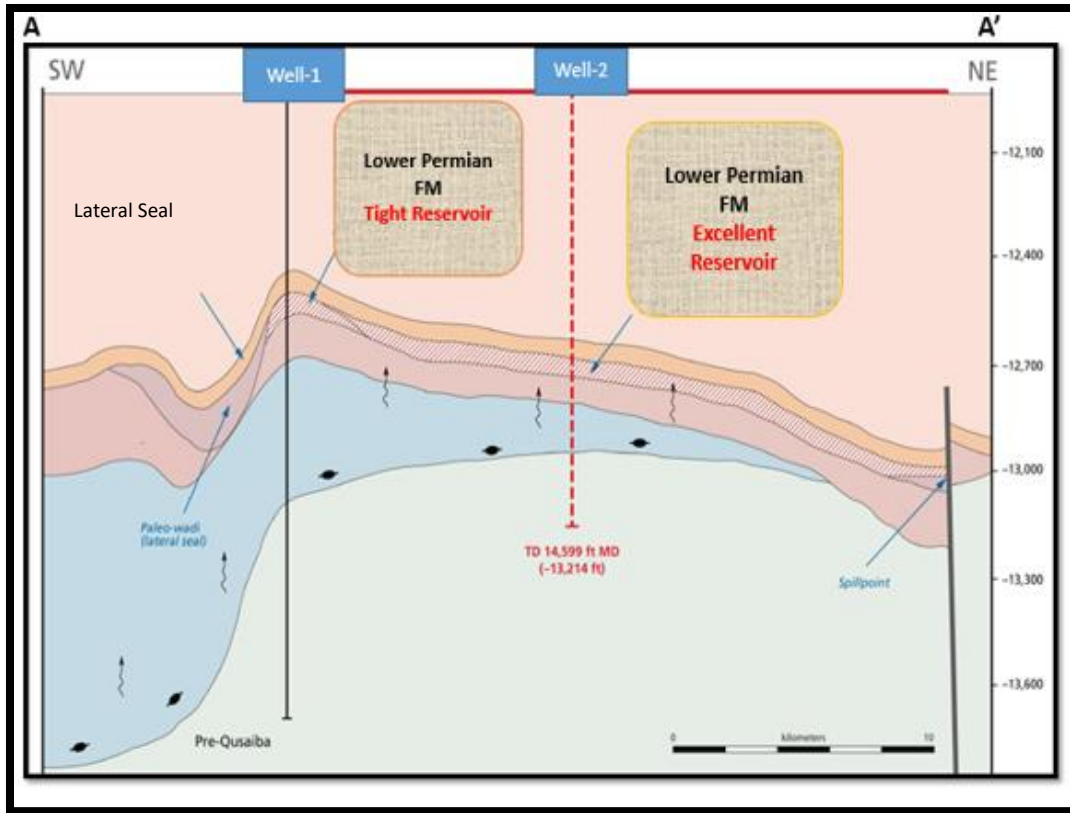
Figure 1.13: Schematic cross-section showing Majhol geologic structure and wells.
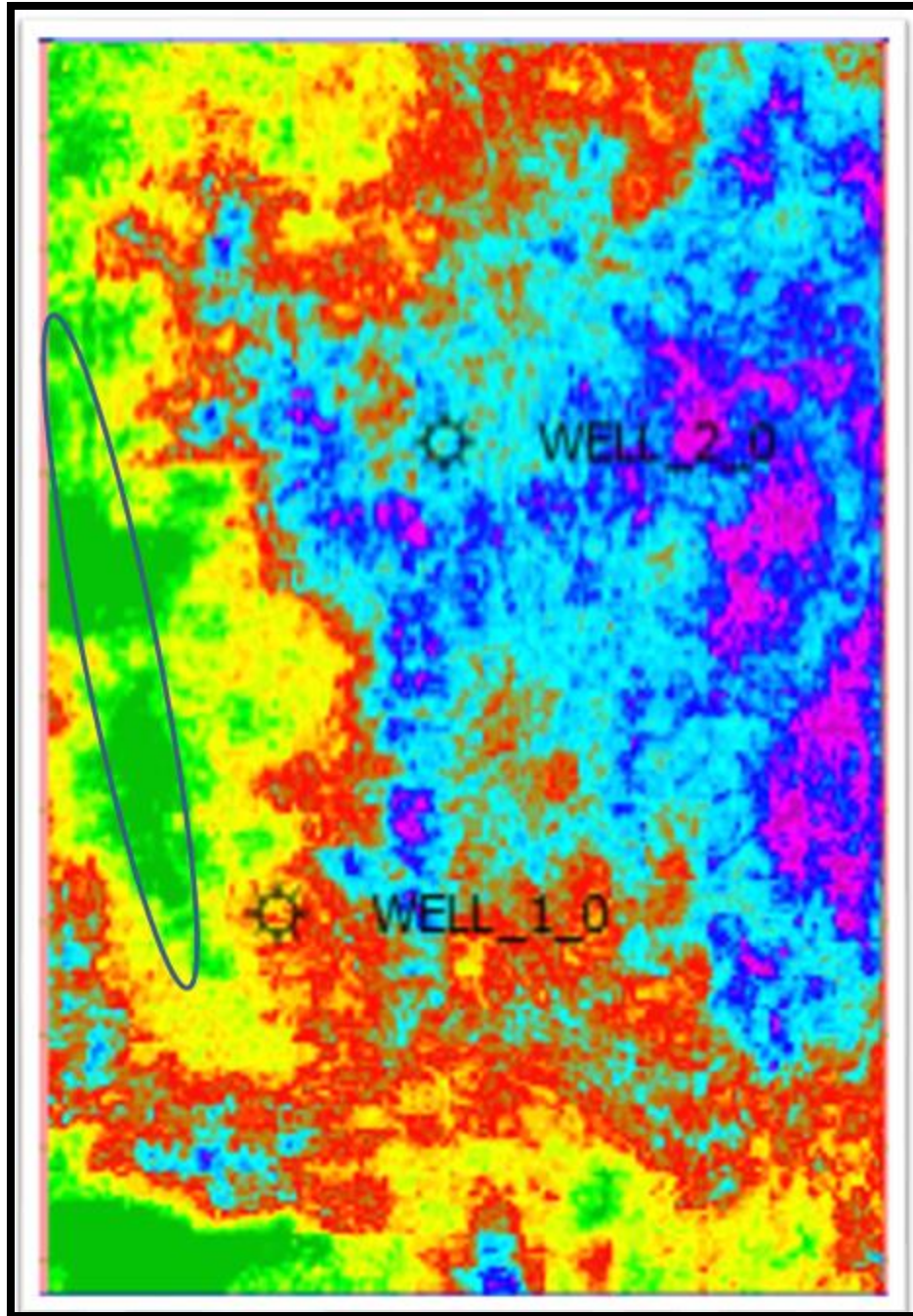
Figure 1.14: Acoustic Impedance shows S-N trending paleo-wadi that acts as a seal in the western of the field

25
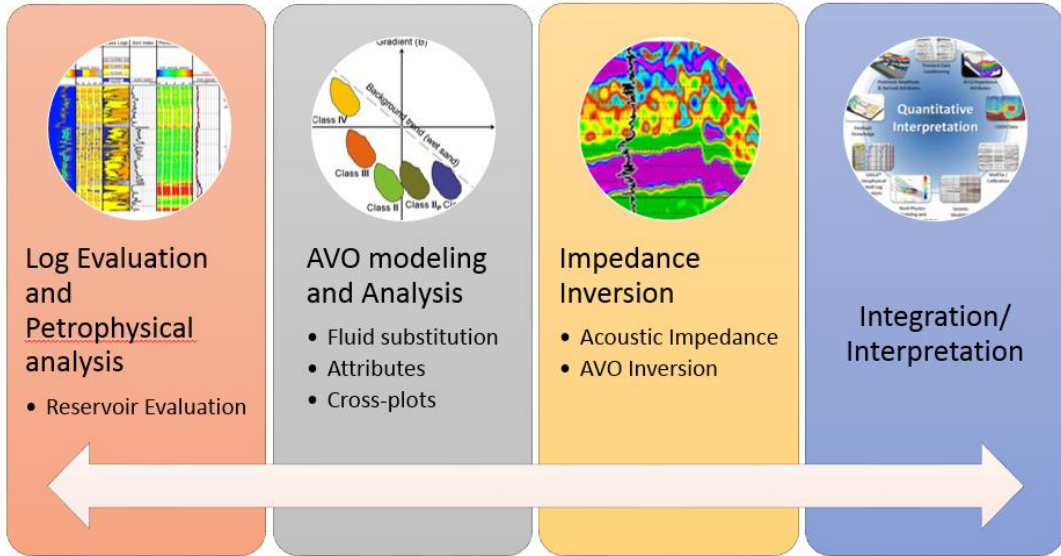
Figure 1.16: Workflow for the research

CHAPTER 2

WELL LOGS INTERPRETATION AND PETROPHYSICAL ANALYSIS

2.1 WELL LOG INTERPRETATION

This section focuses on well log interpretation and petrophysical analysis to determine the reservoir facies and properties. Two wells are available within the study area; both of them have the basic logs (Caliper, Gamma-ray, Neutron, Density, and P-wave sonic, S-wave sonic). Other logs were also calculated such as Vp/Vs ratio, P-impedance, S-impedance, and Poisson ratio, Elastic Impedance, LMR logs, Porosity, and Volume of shale (Figure 2.1)

2.1.1 Gamma-ray log

The Gamma-ray log tool measures the natural radioactivity in rocks and can be used to determine lithology and correlate stratigraphic. Pure sandstones and carbonates have very low radioactive material resulting in low gamma-ray values less than 50 API. However, shale has high radioactive material meaning that has high gamma-ray values (Asquith et al., 2004). Depending on the interpretation of the available logs, the reservoir zone was identified in well-1 to be in the depth of 13865' to 14066' and in the depth range of 14086' to 14293' for well-2.

In both wells, the gamma-ray log shows high values in the seal zone above the reservoir indicating a shale or clay seal. Those values decrease significantly from around

27

100 to 30 API when the log enters the reservoir zone (Figure 2.2). There slight variation in low gamma ray within the reservoir is caused by the clay diagenesis of the reservoir sandstone. The Gamma ray tool reads very high values, in the source rock bellow the reservoir, ranged from 170 to 490 in the Silurian hot shale formation (The source rock).

2.1.2 Density and Neutron logs (Porosity Logs)

Density log measures the formation bulk density which is dependent on fluid content of a rock, porosity of a rock, and matrix density. Neutron logs measure hydrogen concentration in a formation (Asquith et al., 2004). It provides fluid-filled porosity. The most reliable indicator of a reservoir rock can be extracted using both neutron and density logs, with a lower density and the higher neutron curve resulting in touching or crossing the two curves each other's. The greater the crossover between the density and neutron logs means the better quality of the reservoir; additionally, gas zones display a greater crossover for a given porosity than oil or water zones (Darling, 2005). Density log is used also in the process of generating the seismic synthetic in the well seismic tie process. Density and neutron also used to calculate the porosity. Well-1 showed a tight reservoir with both curves touching each other's. The best quality reservoir zone in well-1 was in the top of the reservoir from 13865 to 13878 (Figure 2.3). For well-2 the density and neutron curves shows a better reservoir quality and both curves seem to be touching and crossing from depth 14153to 14269. The best separation occurred in two zones from 14167 ft to 14183 ft and 14200 ft to 14233 ft. the bottom of the reservoir starts to get silty with clear separation between both curves (Figure 2.4).

2.1.3 P-wave and S-Wave sonic

Sonic log is another porosity log that measures interval transit time of a

compressional and shear sound wave (P-wave and S-wave) traveling through the formation along the axis of the borehole. P-wave and S-wave velocity generally increase with depth (Asquith et al., 2004).

In this research, the good sand facies (Aeolian facies) showed an increasing in both P-wave and S-wave sonic (Figure 2.5). The sonic log with density information enabled us also to create synthetic seismogram that helped to tie the seismic with the wells.

2.2 PETROPHYSICAL PARAMETERS CALCULATIONS

I used the available logs to calculate other essential petrophysical and elastic parameters such as Vp/Vs, P-Impedances, S-Impedance, Poisson Impedance, Lambda-Rho, Mu-Rho, Porosity, and volume of shale (Figure 2.6).

Porosity is a measure of void space in a material and reflects fluid storage capacity of the reservoir (Halliburton, 2001), it was calculated by two steps. First, by using the mass balance density-porosity equation (Equation 1) to calculate density derived porosity, and then I used this derived density porosity combined with the measured neutron porosity to compute the average porosity values via equation (2)

$$\emptyset d = \frac{\rho_{ma} - \rho_b}{\rho_{ma} - \rho_{fl}} \qquad (1)$$

$$\emptyset = \sqrt{\frac{(\emptyset d^2 + \emptyset n^2)}{2}} \qquad (2)$$

Where $\emptyset d$ is the density-porosity; ρ_{ma} is the matrix density; ρ_b is the bulk density; ρ_{fl} is the fluid density; $\emptyset$ is the porosity. Another critical parameter is shale volume. As a beginning, I calculated the index gamma-ray value (IGR) based on the IGR formula

(equation 3), volume of shale was then computed via equation 4 which was proposed by Larinov (1969).

$$IGR = (\frac{GR_{log} - GR_{SS}}{GR_{SH} - GR_{SS}}) \quad (3)$$

Where; IGR = gamma-ray index, GRlog = log readings, GRss = gamma-ray values for sandstone baseline, and GRsh = gamma-ray values for shale baseline.

$$V_{SH} = 0.083 * (2^{3.7*IGR} - 1) \quad (4)$$

Where; Vsh = volume of shale, and IGR = gamma-ray index.

Shale baselines are chosen as 28, and 120 API for sandstone and shale, respectively.

Other physical and elastic logs were directly calculated from the basic logs. Those logs were used in the AVO modeling and in the cross-plot analysis (Figure 2.6).

2.3 CROSS PLOTTING OF ROCK PROPERTIES

Cross plotting has been performed from well logs for fluid and lithology discrimination using well data. It a clever way for visualizing petrophysical data. It can reveal more about a formation than a standard log-depth display (Castagna and Swan, 1997).

2.3.1 Gamma Ray versus Vp/Vs Ratio Cross plot

Gamma ray and Vp/Vs logs are great lithology indicators to classify the reservoir facies, I cross-plotted the Gamma ray against the Vp/Vs ratio for both wells. Three main clusters were identified from the cross plot of well-1(Figure 2.7). The yellow zone (Aeolian Sand dunes) showed a low gamma ray (bellow 40 API) and low Vp/VS ratio (bellow 1.7). This zone is the best reservoir zone with the cleaner sandstone. The green zone showed sandstone that is affected by diagenesis with gamma ray values in range of 45 to 70 API and average Vp/Vs of 1.7. The third zone 3 (the pink circle) are shale

siltstone with high gamma ray and Vp/Vs ratio. Those three zones are displayed in the cross-section to the right of (Figure 2.7).

The same three lithofacies are identified in well-2 cross-plot of the Gamma Ray versus Vp/Vs ratio (Figure 2.8). The yellow zone (Aeolian facies) has excellent reservoir properties with low gamma ray and Vp/Vs ratio. In addition, this yellow zone has Neutron-density crossover which is an excellent indication of the gas existence in this zone (Figure 2.3). This Excellent sand has a net thickness of 52 feet in the reservoir. The green Zone (Sand sheet) has 43 feet thickness of tight sandstone that was affected by diagenesis. It has higher gamma ray and Vp/Vs ratio values than zone1. The purple zone (Playa lake Facies 14273' to 14294') is a siltstone and sandy siltstone found in the bottom of the reservoir with a thickness of around 20 feet.

2.3.2 P-Impedance Vs S-Impedance

The P-impedance vs S-impedance cross-plot, showed a deviation of the good sand cluster from the background trend. It showed higher S-impedance of the gas sand than the wet sand. Also we noticed that the good reservoir sand has high P-impedance (Figure 2.9).

2.3.3 Poisson Impedance Vs P-Impedance

The Poisson's Impedance is equal to (P-Impedance minus 3*S-Impedance). This attribute is derived from the combination of the P- and S-impedance values and is a good hydrocarbon indicator (Quackenbush, 2006). The high impedance with Low Poisson Impedance indicate the gas sand (Blue zone) the low impedance indicate the interdune zone (Figure 2.10). The gas sand has high impedance and low Poisson's impedance.

31

2.3.4 P-Impedance versus Vp/Vs

The Aeolian sand dunes appeared to have high impedance in the yellow zone with low Vp/Vs ratio. The sand sheet seemed to have low impedance and higher Vp/Vs comparing to the gas sand. The siltstone has high impedance and high Vp/Vs (Figure 2.11).

2.3.5 Lambda-Rho versus Vp/Vs

Lambda-Rho Versus Vp/Vs helped to distinguish between the three facies in which the gas sand has low Lambda and low Vp/Vs. while the sand sheet has low lambda with higher Vp/Vs and finally the shaley siltstone has high lambda and high Vp/Vs. (Figure 2.12.)

2.3.6 Lambda-Rho versus Mu-Rho

Lambda-Rho vs Mu-Rho is another great tool to discriminate the lithology and fluid of the reservoir. The best way to interpret the lambda-Rho and Mu-Rho is by crossplotting against each other's. Lambda-Rho is a good indicator for fluid while Mu is a good indicator for lithology. In our case the gas sand has low Lambda and high Mu (Figure 1.13)

2.3.7 Near versus far elastic Impedance

Near versus Far elastic impedance showed a deviation of the gas sand bellow the background trend (Figure 1.14). The far impedance became noticeably lower when going through hydrocarbon zone.

2.4 TABLES AND FIGURES

Table 2.1: Summarized petrophysical properties for the reservoir facies. Density, Vp/Vs, Lambda-Rho, and Mu-Rho were the best properties to distinguish between the good sand the tight sand.

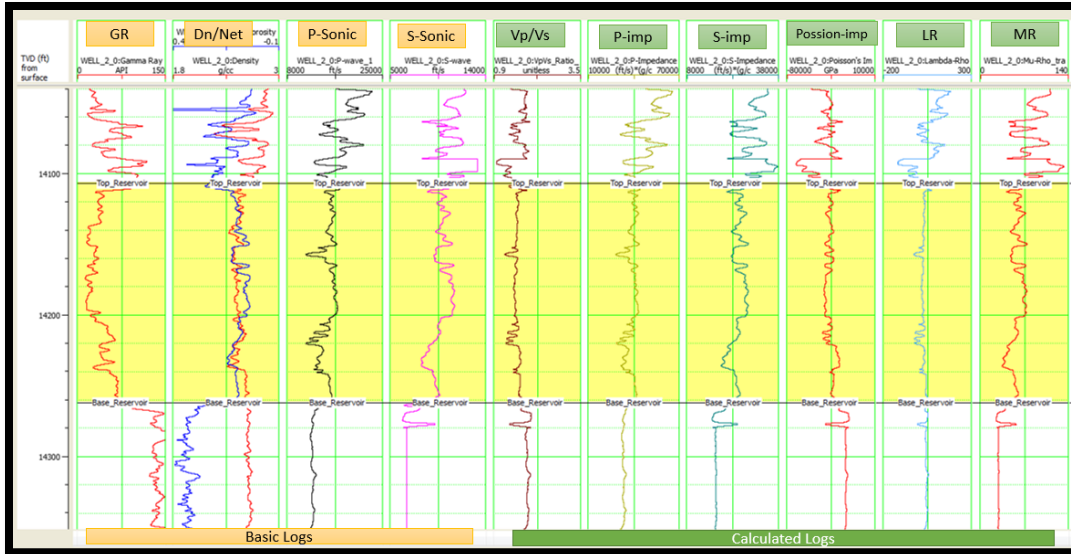|	Sand Dunes	Sand Sheet	Playa
GR	Low	Mid	High
P-wave	High	Mid	High
S-wave	High	Mid	High
Density	Low	Mid	High
P-Imp	High	Low	High
S-Imp	High	Mid	Mid
Vp/Vs	Low	Mid	High
Lambda-Rho	Low	Mid	High
Mu-Rho	High	Mid	Mid

33

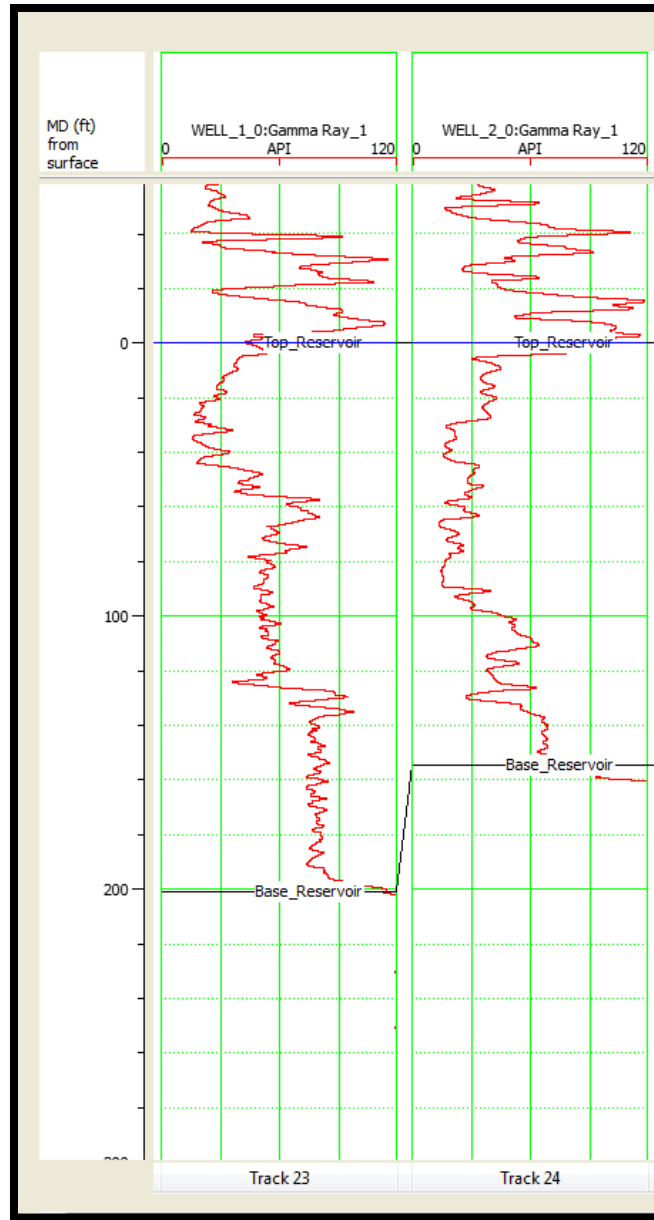Figure 2.1: Well-1 recorded and calculated logs.

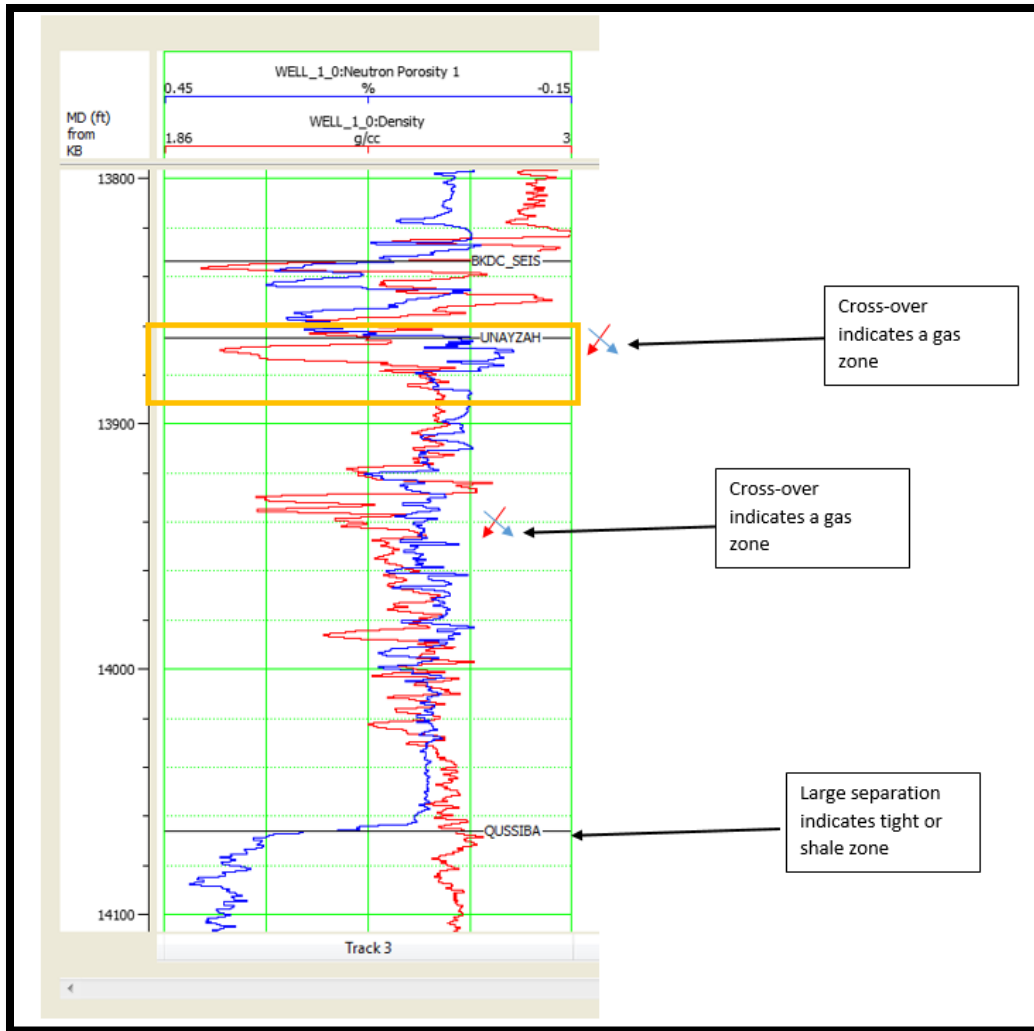Figure 2.2: Gamma ray of well-1 and well-2.

Figure 2.3: Well-1 density and neutron shows a cross-over on the top of the reservoir that may indicate existing of gas. Large separation in the seal and the source indicates tight shale.
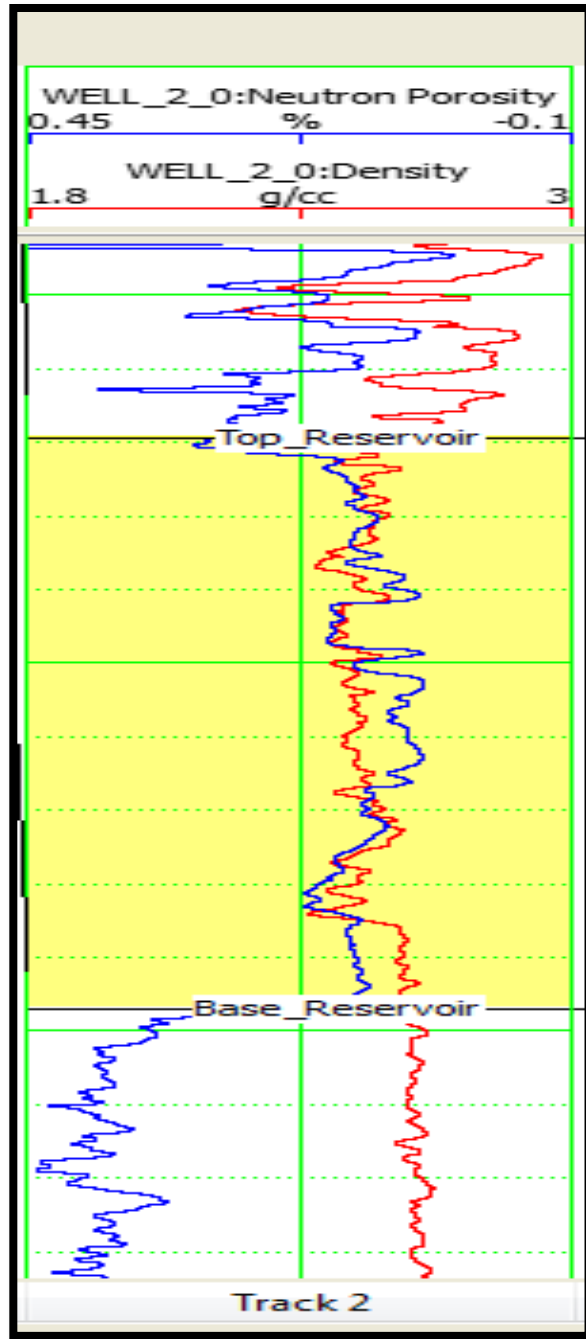
Figure 2.4: Well-2 density and neutron logs
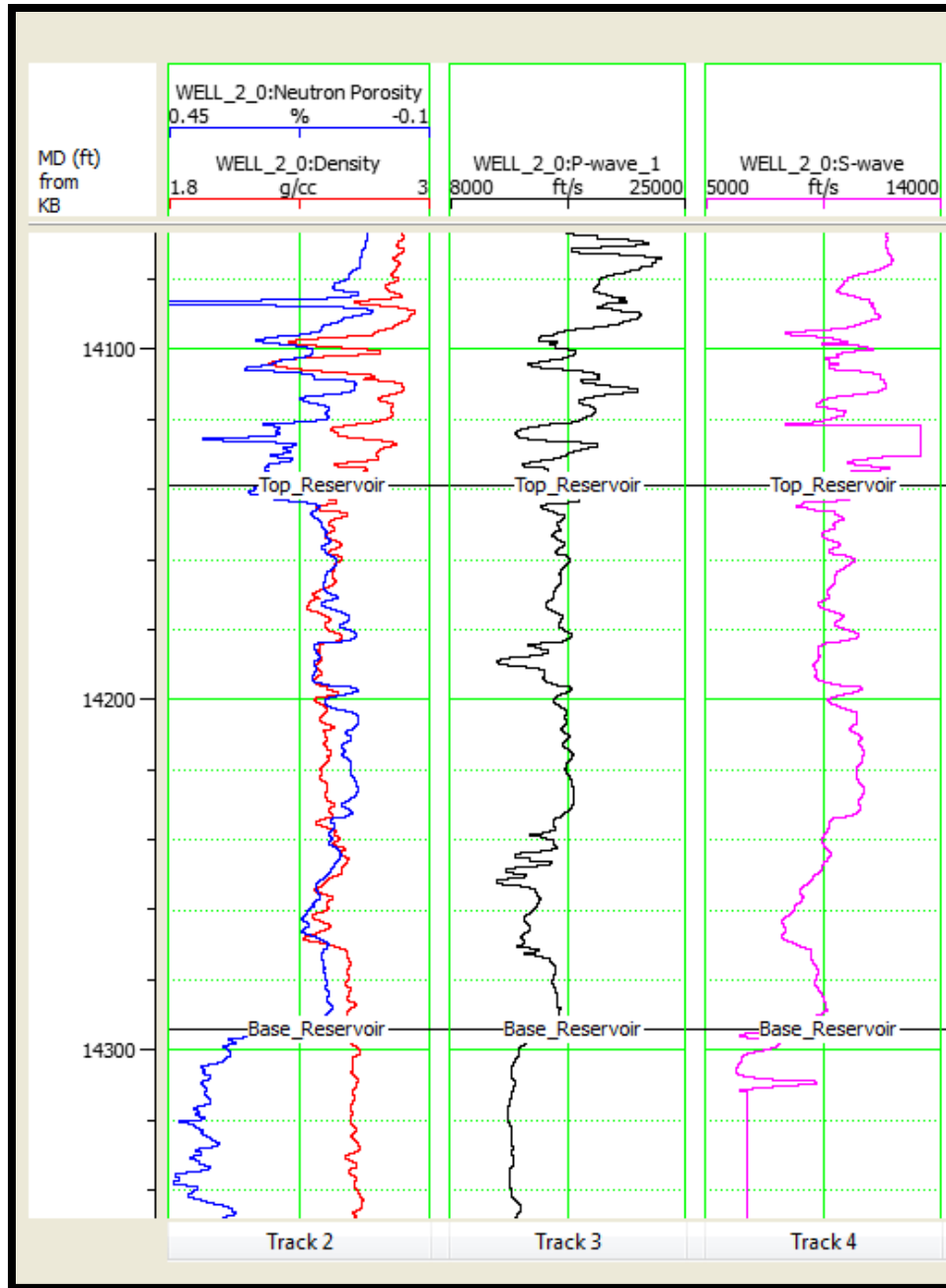
Figure 2.5: Both P-Sonic and S-Sonic increases at the gas sand zone.
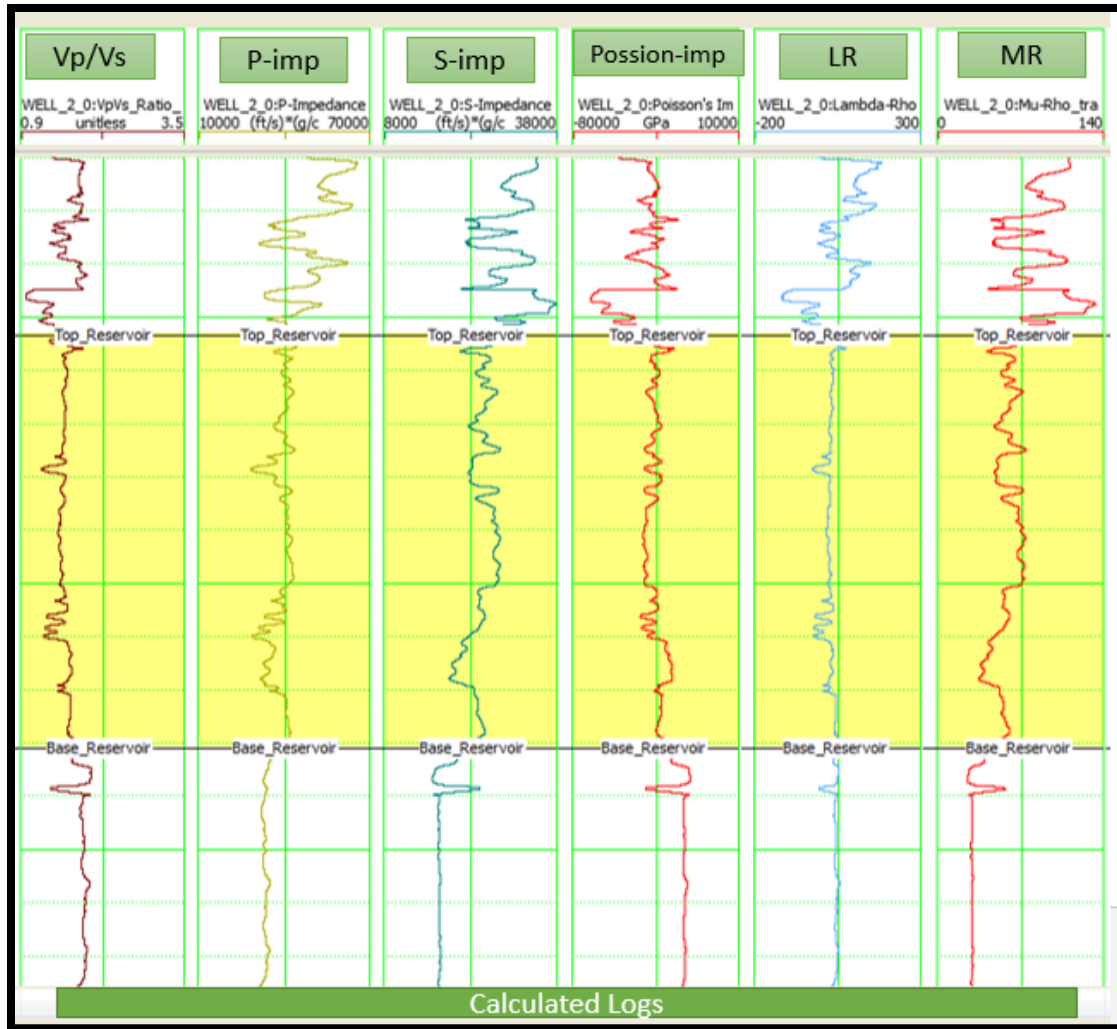
Figure 2.6: The calculated physical and elastic logs.
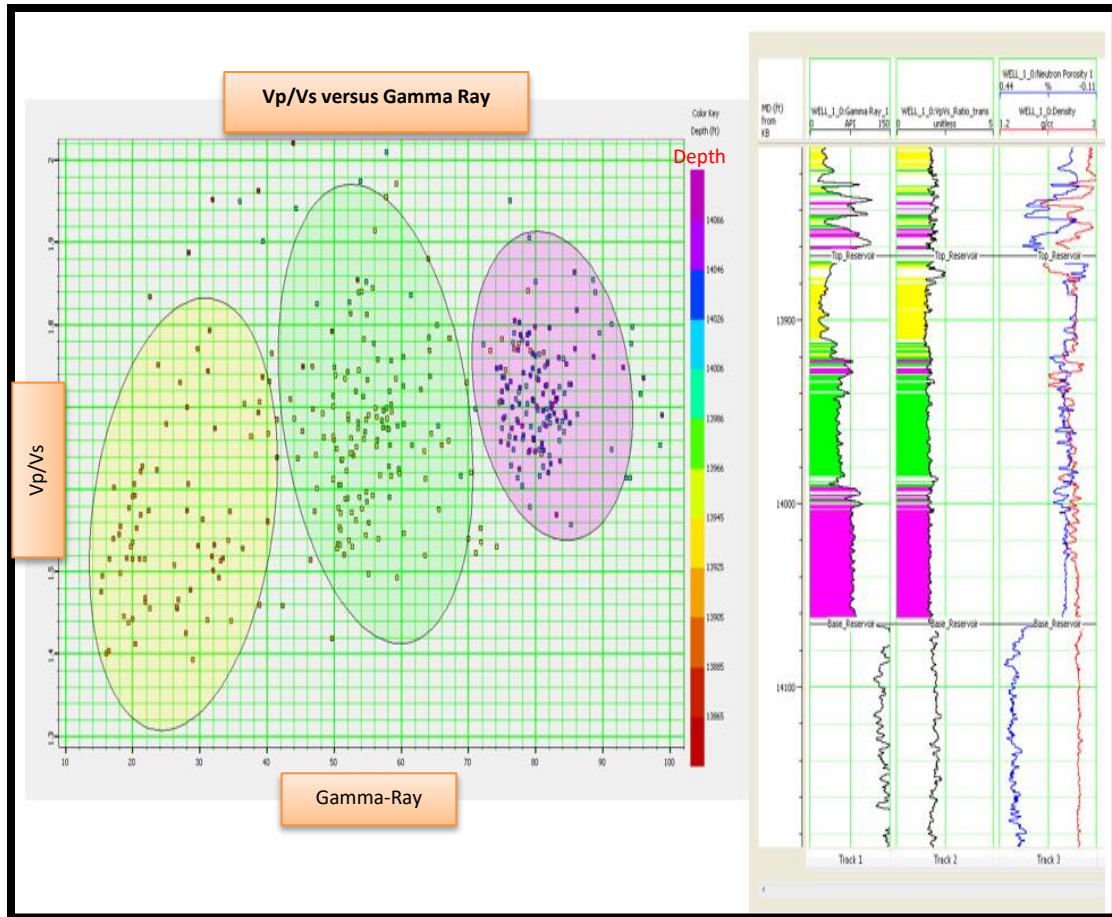
Figure 2.7: Cross-plot (left) of Vp/Vs ratio against Gamma-ray for well-1. Cross-section (right) displays the three different selected clusters (facies). The yellow zone indicates the good sandstone while the purple one is indicating the siltstone in well-1.
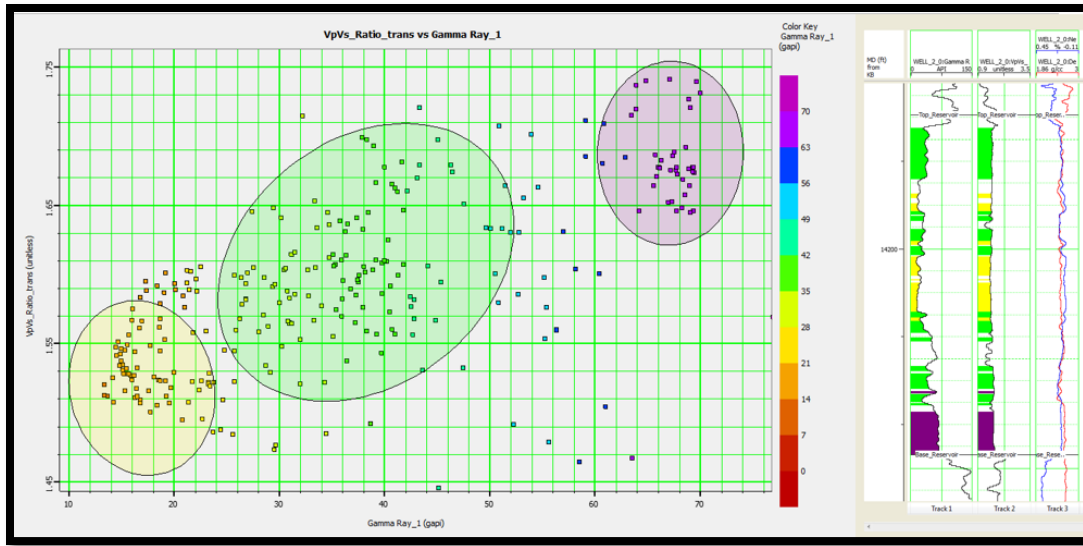
Figure 2.8: Cross-plot (left) of Vp/Vs ratio against Gamma-ray from well-2. Cross-section (right) displays the three different selected clusters (facies)
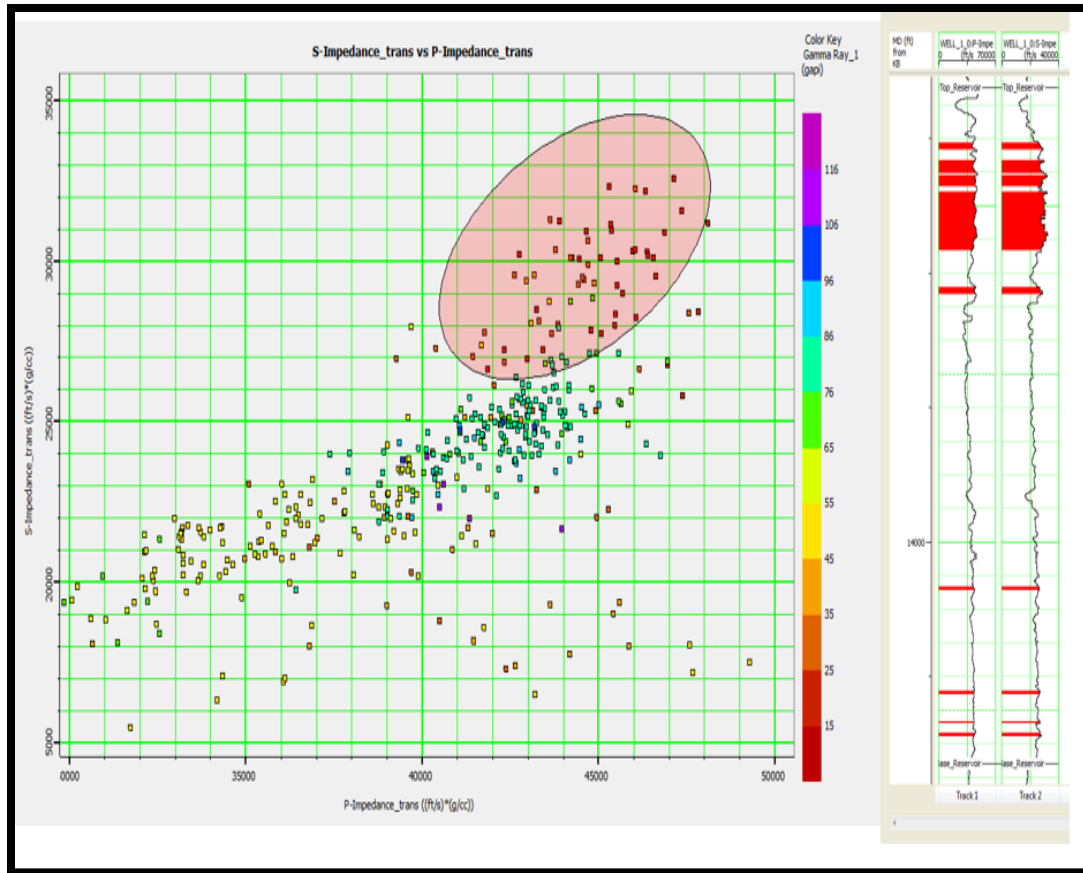
Figure 2.9: P-impedance Vs S-impedance cross-plot to the left; right the cross section shows the gas sand zone.The gas sand has higher S-impedance and deviated from the background trend.
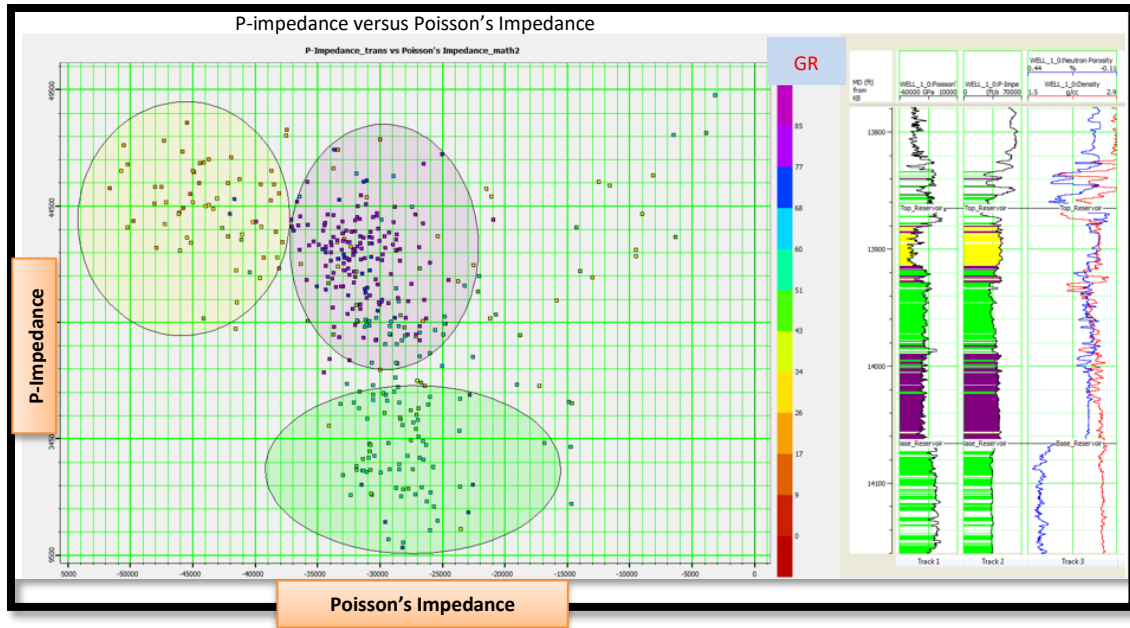
Figure 2.10: Poisson Impedance Vs P-impedance cross plot and cross section. The gas sand has low Poisson's Impedance and high P-impedance.
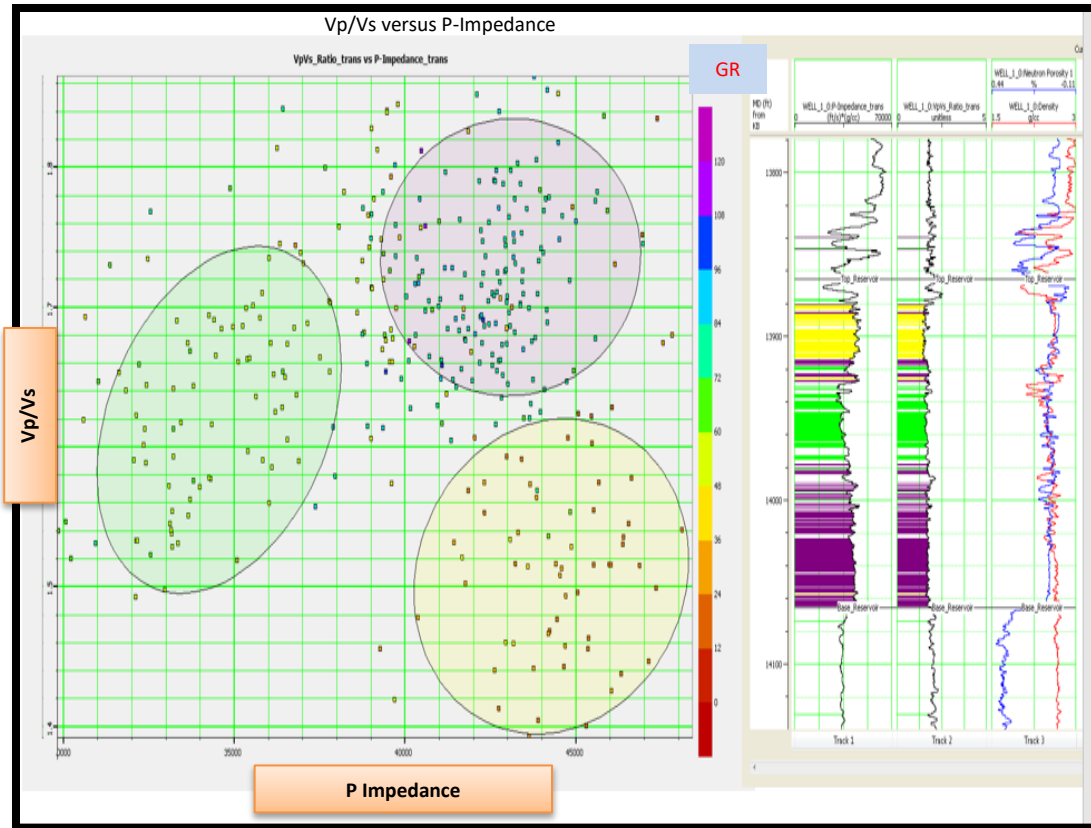
Figure 2.11: P-impedance Versus Vp/Vs cross plot and cross section.The gas sand has low p-impedance and Vp/Vs.
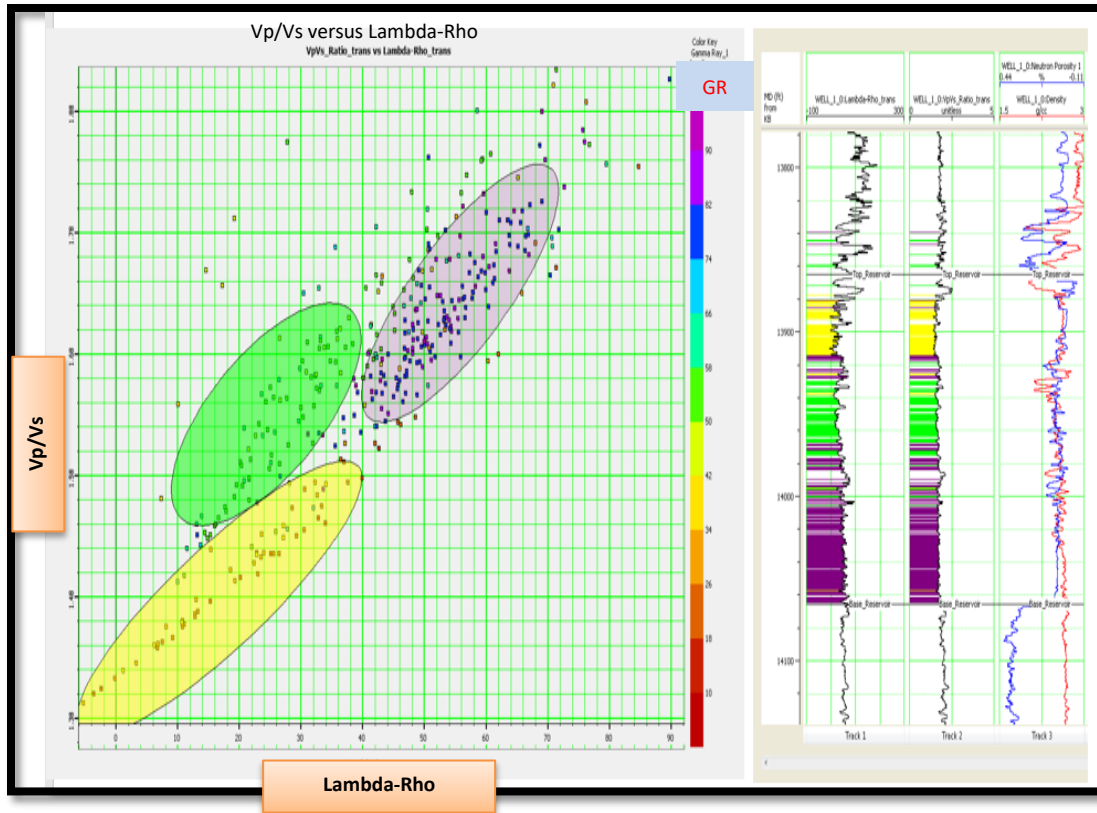
Figure 1.12: Vp/Vs versus Lambda-Rho. The gas sand has low lambda and Vp/Vs. cross-section in the right showed the good sand in well-1.
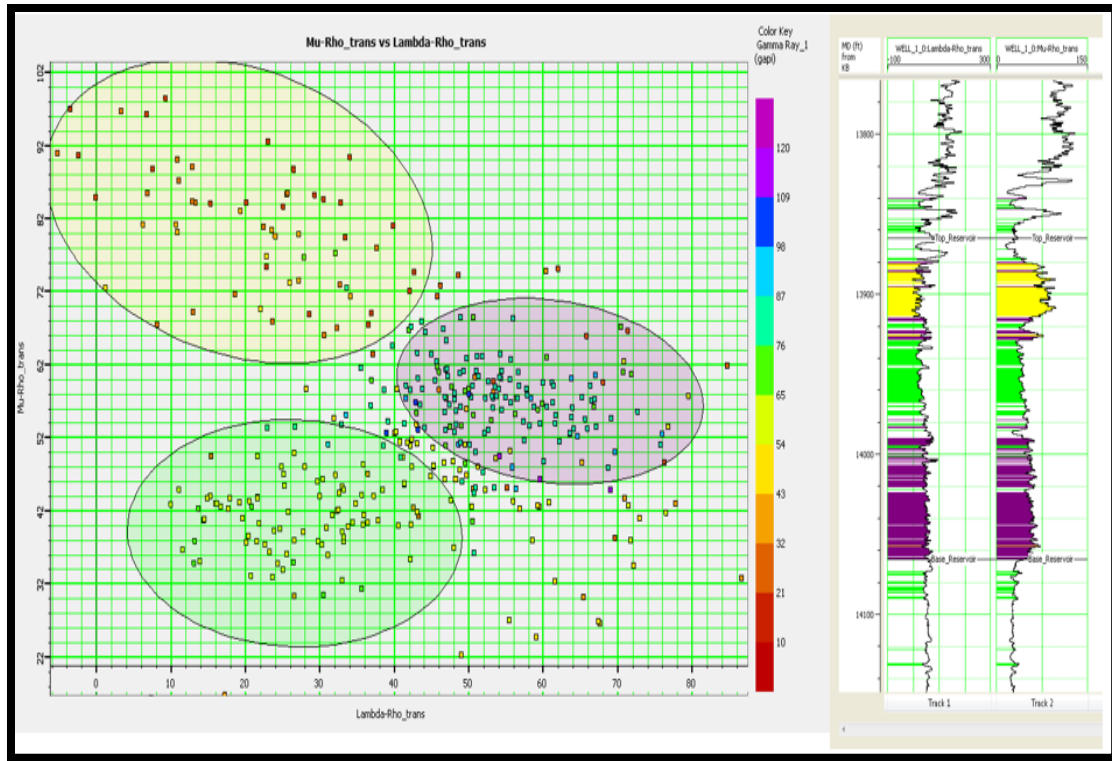
Figure 1.13: Lambda-Rho versus Mu-Rho cross plot and cross section.
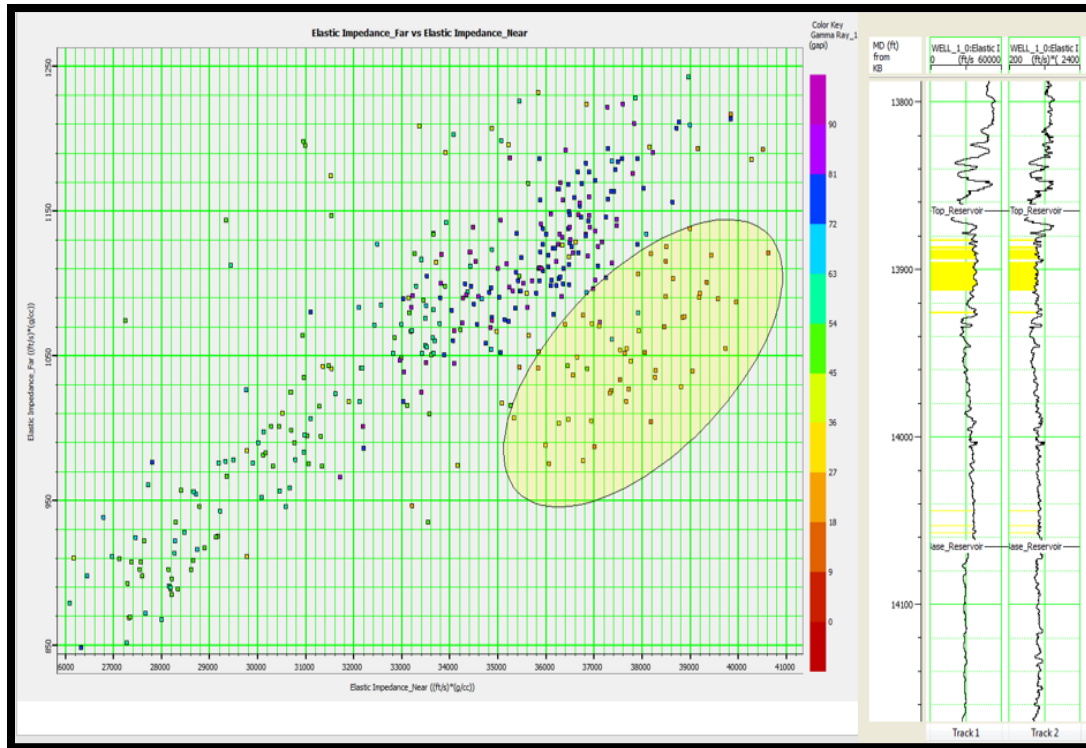
Figure 1.14: Near and far elastic impedance cross plot and cross section for well-1.

CHAPTER 3

AVO MODELING AND ANALYIS

3.1 AVO THEORTICAL BACKGROUND

The amplitude of seismic reflection varies with offset (angles of incidence). Studying the behavior of the amplitude changes with offset can tell us more about the lithology and fluid properties (Castagna and Swan, 1997). The amplitude may show increasing or decreasing with offset/angle of incident based on the rock property contrast (P- and S- velocity, density and Poisson ratio).

Zoeppritz in 1919 was able to come up with complex equations to calculate the angle dependent reflection and transmission coefficients. However, those equations were difficult to be understood and applied in the AVO process. Numerous attempts have been made to find simple approximations to Zoeppritz equations. The famous approximations to Zoeppritz's are summarized in table 3.1. In this research I used Wiggins three terms equation where R (θ) = P-wave reflection coefficient as a function of angle, A (Intercept) = Normal incidence P-wave reflection coefficient, B= gradient and it is dependent in P-wave, S-wave Velocity, density, C= curvature and is neglected at near and medium angles (Ruessell, 1999).

The Intercept (A) is the zero offset reflection coefficient; it depends on the p-wave velocity and density (acoustic impedance) of the overlaying and underlying layers. The gradient (B) is the responsible for the amplitude changes with offset and it depends

48

on the p-wave and S-wave velocity, and density. The curvature (C) is almost zero at low angles (lower than 30 degrees), that's why it might be neglected in some cases (Russell, 1999).

The fact that hydrocarbon affects the acoustic impedance and Poisson's ratio of reservoir sandstone allowed to develop of the AVO attributes to detect these effects. The most famous attributes are (A*B) product, Scaled Poisson ratio change (A+B), shear reflectivity (A-B), and the fluid factor. Cross-plotting of intercept and gradient also can help to distinguish hydrocarbon saturated reservoir from wet background and shale (Foster, 2010).

Rutherford and Williams (1989) classified the gas anomalies of amplitude variation with offset into three classes. In addition, Castagna and Swan added the class 4 (Figure 3.1):

Class 1: High impedance sand with decreasing AVO

Class 2: Near-Zero impedance contrast with increasing AVO

Class 2p: Near-Zero impedance with polarity change

Class 3: Low impedance sand with increasing AVO

Class 4: Low impedance sand with decreasing AVO

Class 1 sands show higher impedance than the encasing shale resulting in positive amplitude at the zero-offset angle. The amplitude decreases with increasing offset. Class 2 has near zero impedance with the encased shale with negative amplitude that starts to increases with increasing offset. Class 2p has also low impedance contrast with positive amplitude that decrease with offset until it changes polarity then it starts to increase. Class 3 is the typical bright spot it has lower impedance than the encasing shale with

large negative values for zero offset reflection coefficient that becomes more negative as offset increases. Class 4 was proposed lately by Castagna and Swan who stated that the same gas saturated sand can produce various AVO behaviors depending on its overlying and underlying media and for that reason it would be inaccurate to classify a reflector based on the property of sand alone. Class 4 has low impedance gas sand with negative amplitude that decreases in magnitude with increasing offset. The four AVO classes were classified based on the position on A-B cross-plot (Figure 3.1, Rutherford and Williams, 1989).

3.2 AMPLITUDE VERSUS OFFSET MODELING

AVO modeling or the seismic forward modeling is the process of creating angle dependent synthetic from the well logs. It helps one to understand and discriminate hydrocarbon-related AVO responses form background lithology responses (Russell, 1999).

Well-2 was used in the AVO modeling to create angle dependent synthetic gathers for both gas and brine cases by using Gassmann equations. Then, I have created the synthetic using both Aki-Richards and Zoeppritz modeling that required the existence of p-wave, S-wave, density, angle dependent wavelet, and water saturation.

I used Hampson Russell software to create the AVO synthetic models through the following process. (1) Seismic well correlation: Since the well data is in depth while the seismic is in time, I needed to create a time depth relationship by using the sonic log and the check shot data (Figure 3.2). Sonic (velocity) well log tool measures discrete transit times of the rock adjacent to the well bore. The transit times are made over a set tool distance for each depth sample, and the interval velocity is derived over that distance.

50

From these velocities, a time-depth curve can be calculated. This resulting time depth relationship will not perfectly match the seismic for many reasons such as:

- The seismic and log datum are usually different.

- Errors in calculating time-depth from logs accumulate.

- The seismic data may have time stretch caused by frequency dependent absorption.

- Surface seismic data are subject to greater dispersion and absorption than the sonic data recorded in the well.

Therefore, check shots are used to improve the depth-time conversion. The check shot correction adapts the sonic log velocities and/or the log time-time curve to match the time depth relationship obtained from surface seismic data (Sheriff, 2002, Figure 3.2).

3.2.1 Synthetic Seismogram generation (Forward modeling)

Seismic forward modeling is basically convolving seismic reflectivity r(t), derived from p-wave, s-wave velocity and density well logs, with a wavelet w(t) extracted from the seismic at the well location (Figure 3.3) to generate a synthetic seismic, s(t). Then correlate this synthetic with the real seismic.

$$S\ (t) = r\ (t) * w\ (t)$$

There are some assumptions when generation the synthetics including: the geological dip is zero, the well bore is vertical, log readings are accurate, and the velocity only varies with depth (Liner, 2004).

3.2.2 Generating a Wavelet

A wavelet is critical key for successful AVO and inversion result. Two main steps were used when creating the wavelet, the first step is to generate a statistical wavelet with

51

constant phase to initially correlate the synthetic with the seismic and after getting a fair correlation I generated another wavelet using the wells to correct for the phase (Russell, 1999).

(1) Extracting Statistical wavelet:

I used the nearby seismic data to extract a zero phase wavelet. The algorithm extracted the wavelet amplitude spectrum by analyzing the autocorrelation of a set of traces over a selected time window. I chose a range of 100 to 2300 ms. the specified parameters to extract wavelet are indicated below:

Taber length (ms): 25

Phase type: constant (zero phase)

Sample rate (ms): 1

Wavelet length (ms): 200

After creating the depth-time relationship, I generate the seismic synthetic from the well logs, particularly by using the density and P-sonic log to create the reflectivity that were convolved with the wavelet to generate a seismic synthetic

(2) Generating a wavelet from the wells

In this step I used well logs to extract a wavelet. The algorithm used both the available wells and the seismic data near those wells. It extracts the wavelets by finding the operator which when convolved with reflectivity from the well, closely approximates the nearby seismic traces. This procure extracted the actual wavelet phase from the data, but it is very sensitive to the quality of the correlation between well logs and seismic data.

3.2.3 Generating synthetic and correlate it to the seismic

Density and sonic logs were used to calculate the impedance that was used to create the reflectivity, then convolved with the statistical wavelet initially to generate the synthetic (Figure 3.6).

3.3 FLUID SUBSTITUTION AND SYNTHETIC GENERATION

I used Hampson Russell fluid replacement modeling to perform fluid replacement. P-wave velocity, S-wave velocity, and density were predicted by Gassmann equations for gas and brine scenarios. Then I used both Zoeppritz equation and Aki-Richards to create angle dependent synthetic gathers with a maximum angle was 6 degree (Figure 3.9)

The created Zoeppritz synthetic for brine and gas cases are showed in (Figure 3.9). The gas sand synthetic showed a class 2p anomaly with a low impedance with positive amplitude that changes polarity with increasing offset while the brine case showed a positive increasing amplitude with increasing offset. This indicate the significant effect of introducing gas to this reservoir. (Figure 3.9)

3.4 AMPLITUDE VERSUS ANGLE (AVA) ANALYSIS

NMO-Corrected angle stacks at well locations were used for the AVO analysis. The Angle stacks showed Class 2p AVO anomaly at the locations (Figure 3.11). Class 2p sand anomaly has near-zero impedance with positive amplitude that decreases with offset until it changes polarity. The changing polarity with increasing offset in the pre-stack gathers caused cancelation of amplitudes when stacking the traces and resulting in dimming out of the reflections in the interest spots in the PSTM (Figure 3.11). The objective of this phase was to determine values for A and B by analyzing real seismic

data, partially, angle stacks, by fitting a regression line to the amplitude picks as a function of the sine of the angle squared (Figure 3.12). The real seismic and the gas scenario synthetic were greatly correlated for both the top and base of the reservoir. The top of the reservoir decreasing and changing polarity with offset while the base of the reservoir starting with negative amplitude and change polarity with increasing offset. The top and base reservoir crosses at angle of about 25 degrees. The intercept and gradient cross plot also showed the class2p anomaly based on the Castagna Murdock line equation and Rutherford classification. (Figure 3.12)

AVO attribute was another important tool to delineate the good reservoir zone. By using the three terms Wiggin's equation to calculate the intercept (A) and the gradient (B) from the angle stack. The results of this calculation were two basic attribute volumes: (1) Intercept (A) volume (2) gradient Volume (B) (Figure 3.13). The raw A and B attribute volumes are rarely used in their forms. Instead other AVO attributes are usually calculated from them. I found that the scaled Poisson's ratio change (A+B) has the best result to outline the gas sand from the background trend (Figure 3.14).

3.5 TABLES AND FIGURES

Table 3.1: Linearized approximation to Zoeppritz Equations

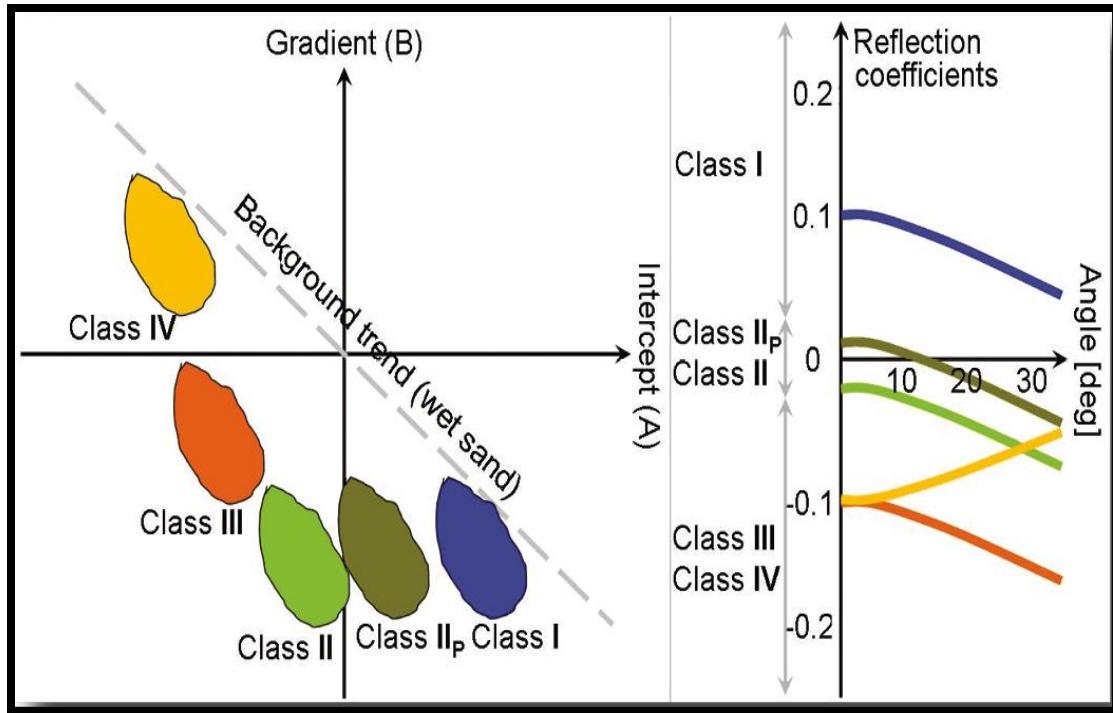| Name	Equation	Weights	Elastic parameters
Aki-Richards	$R_p(\theta) = a\dfrac{\Delta Vp}{2Vp} + b\dfrac{\Delta Vs}{2Vs} + c\dfrac{\Delta\rho}{2\rho}$	a, b, c	Vp, Vs, P Elastic inversion
Wiggins et al. (ABC method)	$R_p(\theta) = A + B\sin^2\theta + C\tan^2\theta\sin^2\theta$	$1, \sin^2\theta, C\tan^2\theta\sin^2\theta$	A, B, C AVO equation
Fatti et al	$Rp(\theta) = C_1 R_p(0°) + C_2 R_s(0°) + C_3 R_D$	c1, c2, c3	$R_p(0°), R_s(0°), R_D$ AVO Inversion
Shuey	$R_p(\theta) = A + (2.25\Delta\sigma - A)\sin^2\theta$	$\sigma = 1/3 \Rightarrow (\frac{Vp}{Vs} = 2)$	Vp, ρ, σ Scaled Poisson's Ratio

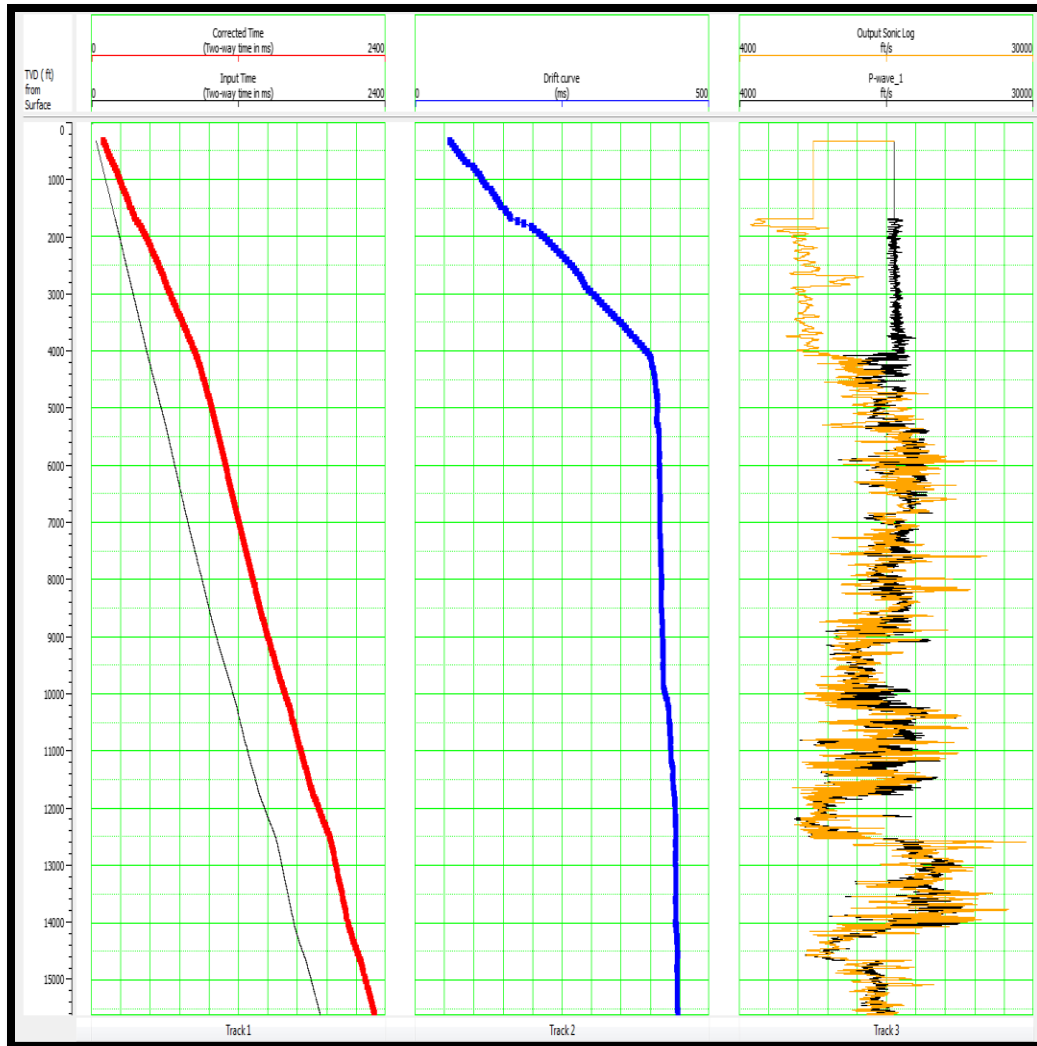Figure 3.1: AVO classification in AVO graph and in the A-B cross-plot.

Figure3.2: track1 shows the input (black) and corrected (red) depth/time curve; track 2 shows the dirt curve (the correction curve); track 3 shows the input (black) and corrected sonic log (yellow)
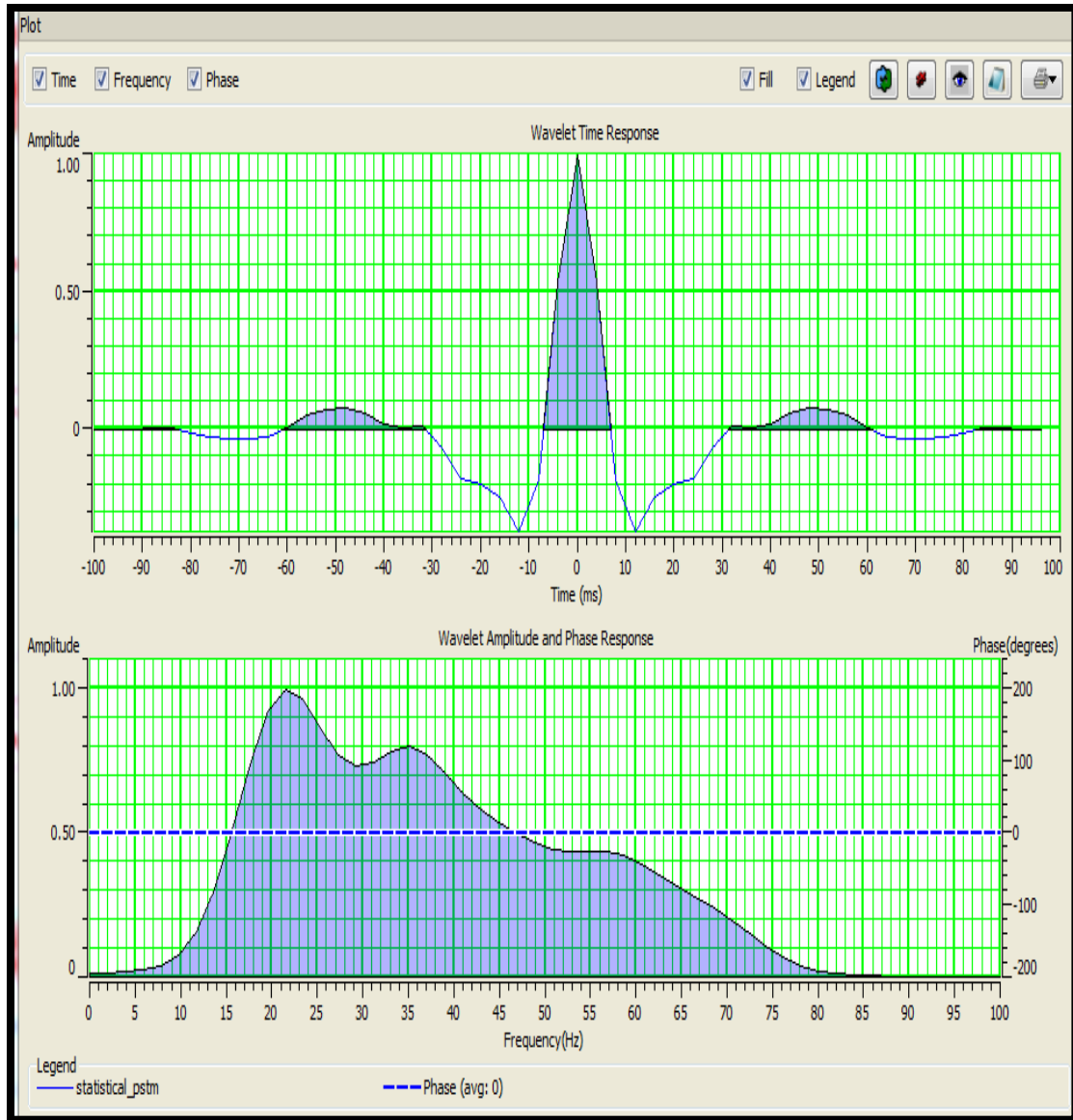
Figure 3.4: zero-phase wavelet extracted from near-stack seismic around well-1 and well-2
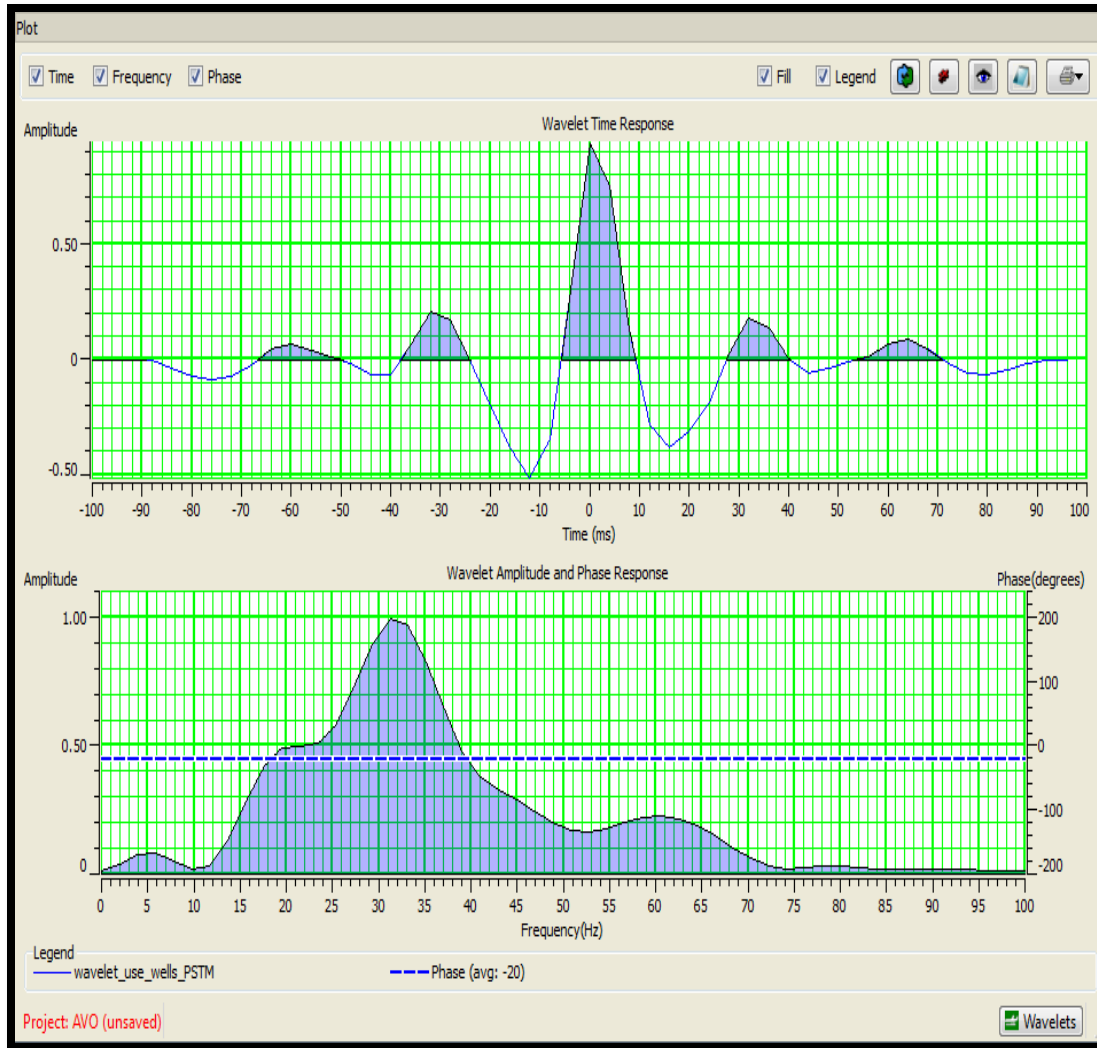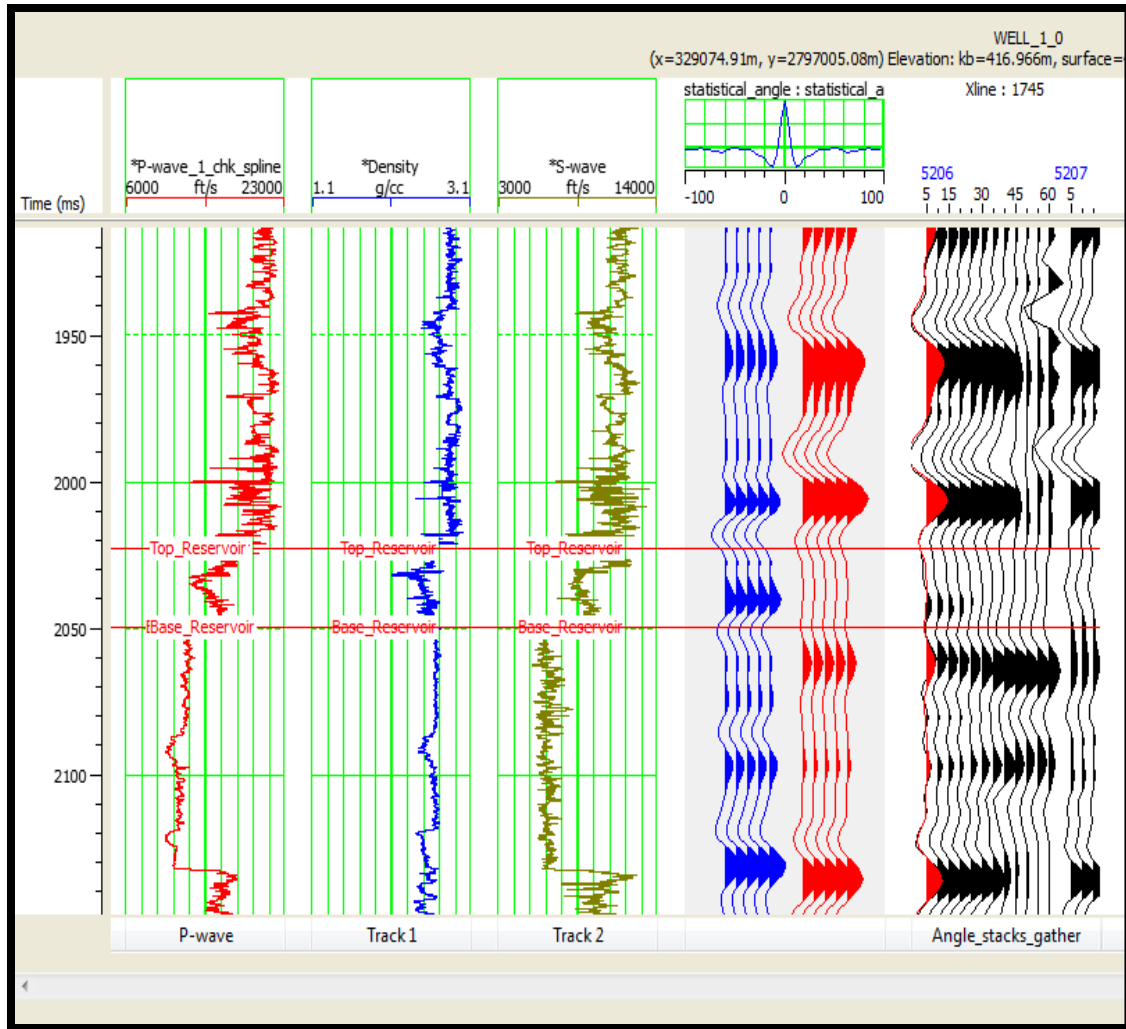
Figure3.5: wavelet using the wells

Figure 3.6: well seismic correlation. Correlation of 60 % between the synthetic and the seismic after applying 10 ms shift.
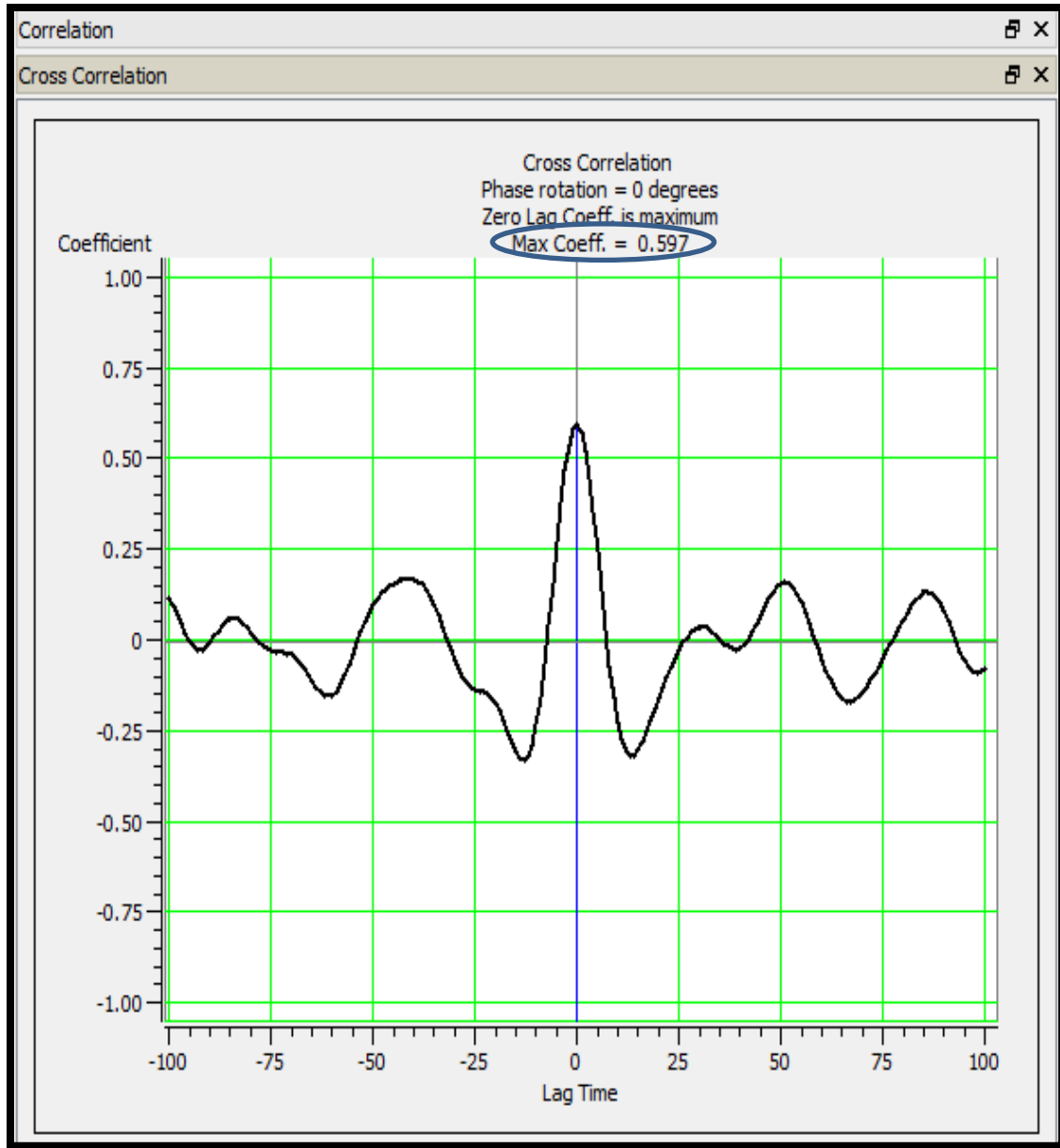
www.manaraa.com

Figure 3.7: correlation of 0.6 between the seismic and the wells after using the wavelet from the wells.
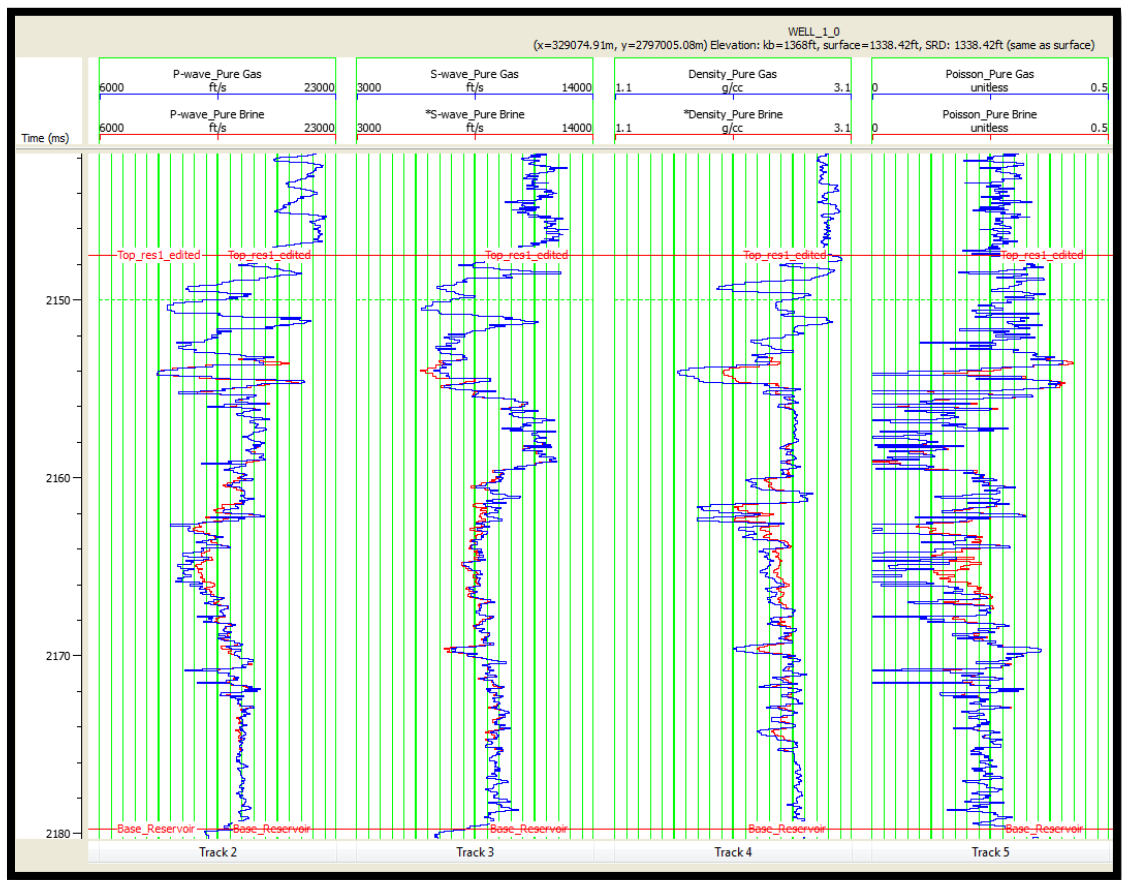
)

Figure 3.8: Gas and brine scenario logs calculated by Gassmann equations with reasonable petrophysical assumptions. The blue curve is for the gas scenario and the red curve for the brine curve.
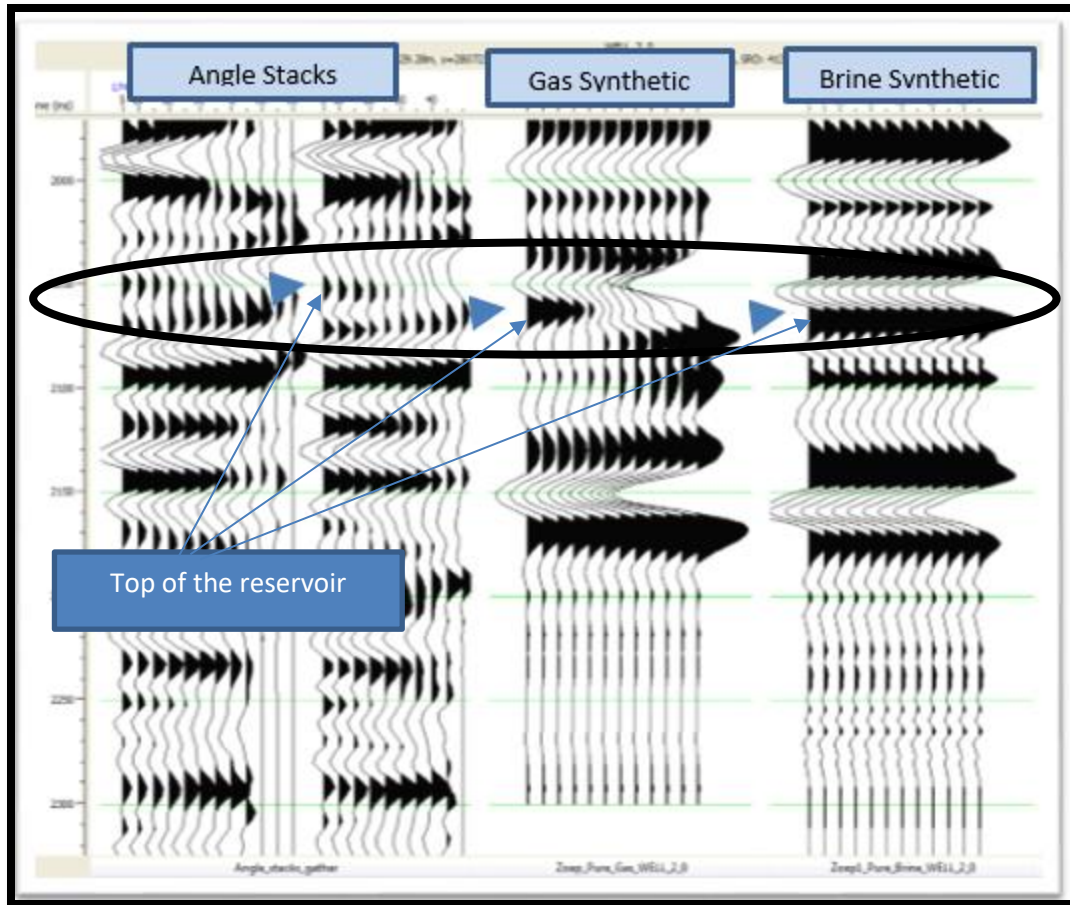
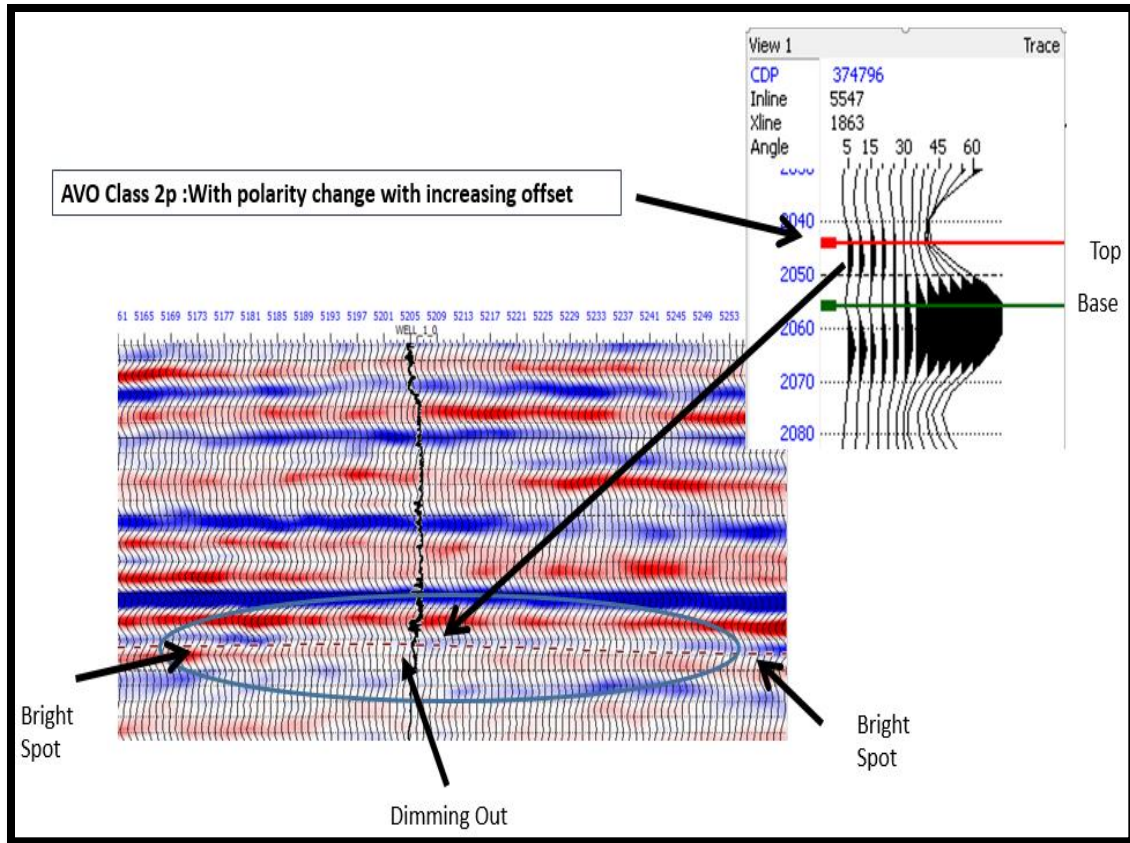Figure 3.9: Angle dependent synthetic for gas and brine and the real angle stack.

Figure 3.11: Angle gather at well-1 showed class2p anomaly with low impedance and polarity changing with offset, resulting in dimming out in the Post stack section.
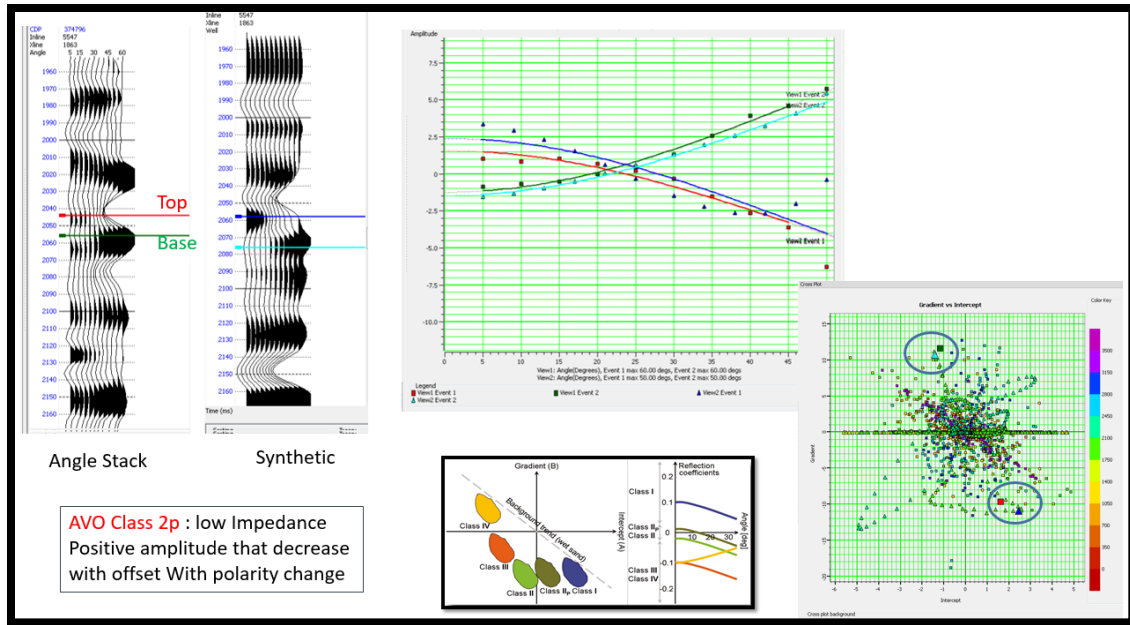
Figure3.12: Left: real seismic angle stack and gas saturated synthetic. Middle: gradient analysis for both top and base of the reservoir in the real and synthetic case. Right: AVO intercept (A) versus gradient (B) cross plots indication both top and base of the reservoir.
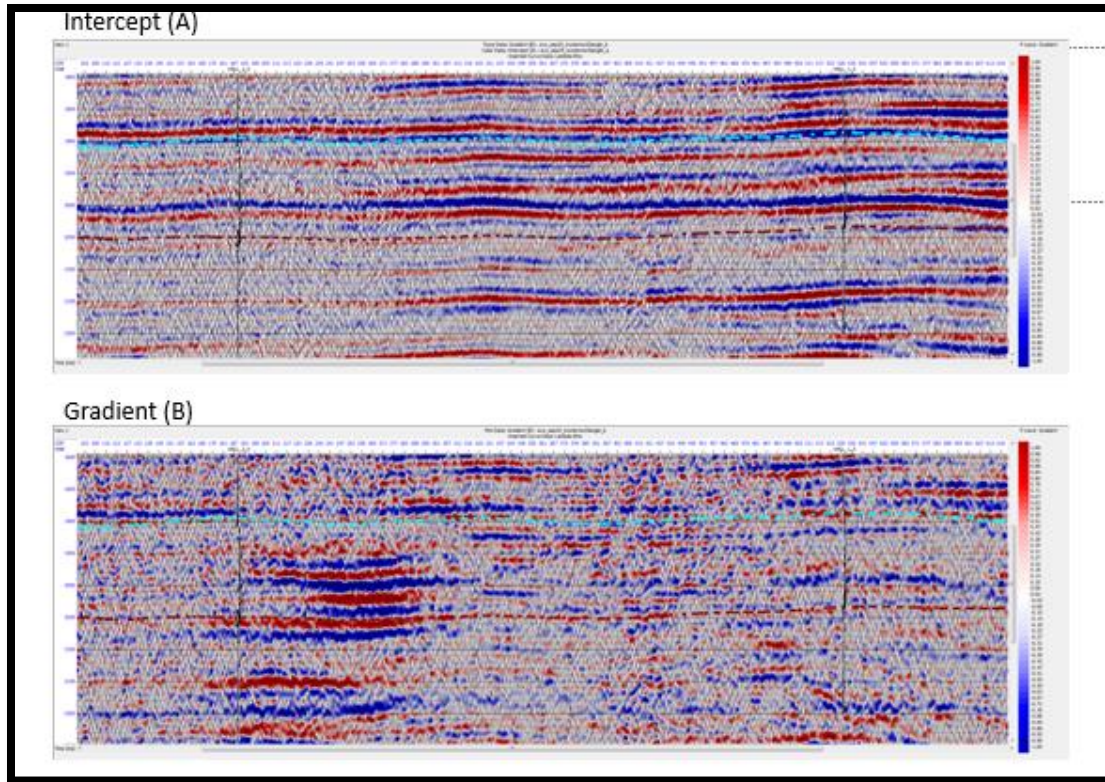
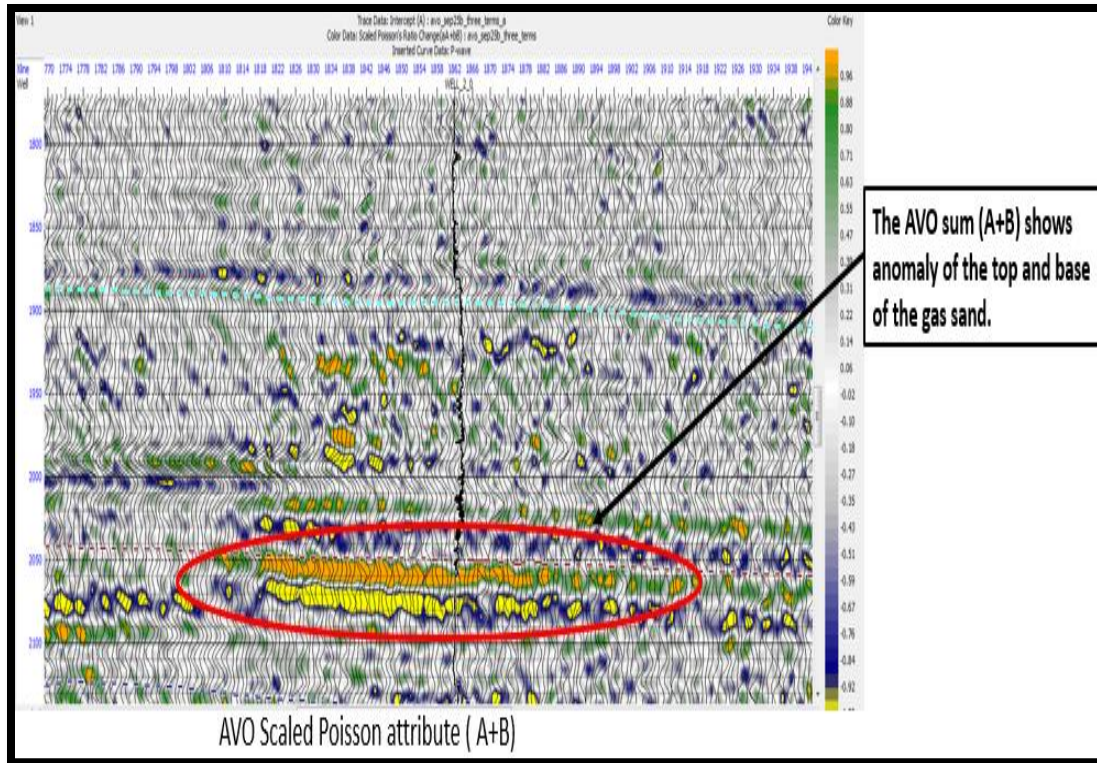Figure 3.13: the intercept (A) and Gradient (B) volumes.

Figure 3.14: AVO Scaled Poisson attribute (A+B).

CHAPTER 4

SEISMIC INVERSION

4.1 INVERSION INTRODUCTION

Seismic inversion is the process of inverting the seismic data to impedance by removing the effect of a wavelet (Russell, 2010). Extracting the Impedance, which the product of the velocity and density, could help to estimate other properties such as porosity.

Impedance contains essential data from the logs and seismic. Unlike seismic data which is an interface property, acoustic impedance is a rock property which shows geology layer and is also related to reservoir properties such as lithology, porosity, and hydrocarbon saturation (Veeken, 2007). Two different inversion approaches were applied in this thesis (1) Elastic impedance inversion (2) Simultaneous inversion

4.2 ELASTIC IMPEDANCE

4.2.1 Introduction

The elastic impedance concept was developed by Connolly 1999. He used the Aki-Richards equation, which relates reflection amplitude to incidence angle. The workflow I used in this approach as following:

- I initially calculated the near and far elastic impedance from the well logs and I noticed the lowering of the values of the far elastic impedance at the gas zones (Figure 4.1).

- I generated two seismic stacks from the angle gathers (Near seismic stack and far seismic stack) (Figure 4.2)

- I created low frequency model for each stack by using the impedance logs and the intercept horizons.

- I also generated a statistical zero-phase wavelet for each stack.

- I finally run an inversion on each stack to create two impedance volumes (Figure 4.3).

4.2.2 Results

By looking at near and far elastic impedance volumes, we noticed a decreasing in the far elastic impedance volume well-2 locations. Also by crossplot them I was able to differentiate the gas cluster from the background trend (Figure 4.4)

4.3 SIMULTANEOUS INVERSION

4.3.1 Introduction

The simultaneous inversion procedure involves building an initial model using the well logs and the interpreted horizons which helps to interpolate for all traces over the whole seismic volume (Figure 4.3).

Inversion analysis was then carried out at well locations. Angle dependent wavelets were extracted and used to enhance the seismic scaling with help of cross-plots from well information (4.6 and 4.7). A good fit between inverted log and basic logs with a correlation of about 0.9 was obtained showing that inversion parameters are optimum.

Once I was confident with the inversion analysis, a simultaneous inversion was ran on the angle stacks to create the following volumes the P-impedance volume, S-impedance volume, Density, and Vp/Vs volume (Figure 4.7). Also Lambda-Mu-Rho

69

attribute were calculated from the simultaneous inversion through Goodway equation (Figure 4.8).

4.3.2 Results

I was able to generate six important elastic volumes from seismic. (1) P-impedance, (2) S-Impedance, (3) Density, (4) P-wave velocity, (5) S-wave Velocity, and (6) Vp/Vs ratio (Figure 4.8).Those volumes were interpreted by creating cross sections, cross-plots, and data slices. The gas sand was characterized by high impedance, low Vp/Vs, low lambda-rho and high Mu-rho from the well logs. The same characteristics were tracked in the seismic-derived elastic volumes (Figure 4.8). The volumes showed high P- , S- Impedance, low density, and low Vp/Vs surrounding well-2 and extending to the east of the well-2. Data slices were taken from those volumes at 20 ms above and below the reservoir horizon. I was able to outline the good sand reservoir from those slices to be around well-2 (Figure 4.9). In addition cross-plotting the seismic-derived elastic properties showed the extension of the excellent gas sand away from well-2 (Figure 4.10).Lambda-Rho and Mu-Rho were Important elastic properties that were found to be effective in the well petrophysical analysis .Goodway in 1997 was able to derived the lambda-rho and mu-rho from the P-impedance and S-Impedance using (equations 4.1 and 4.2). I was able to generate the lambda-rho and Mu-rho volumes (Figure 4.11).then, I interpreted the volumes and cross-plots of the Lambda-rho and Mu-rho in which they helped to confirm the extension of the excellent gas sand (Figure 4.12 and Figure 4.13).

$$\mu\rho = Z_S^2 \quad \text{------▶ Equation 4.1}$$

$$\lambda\rho = Z_P^2 - 2 Z_S^2 \quad \text{---▶ Equation 4.2}$$
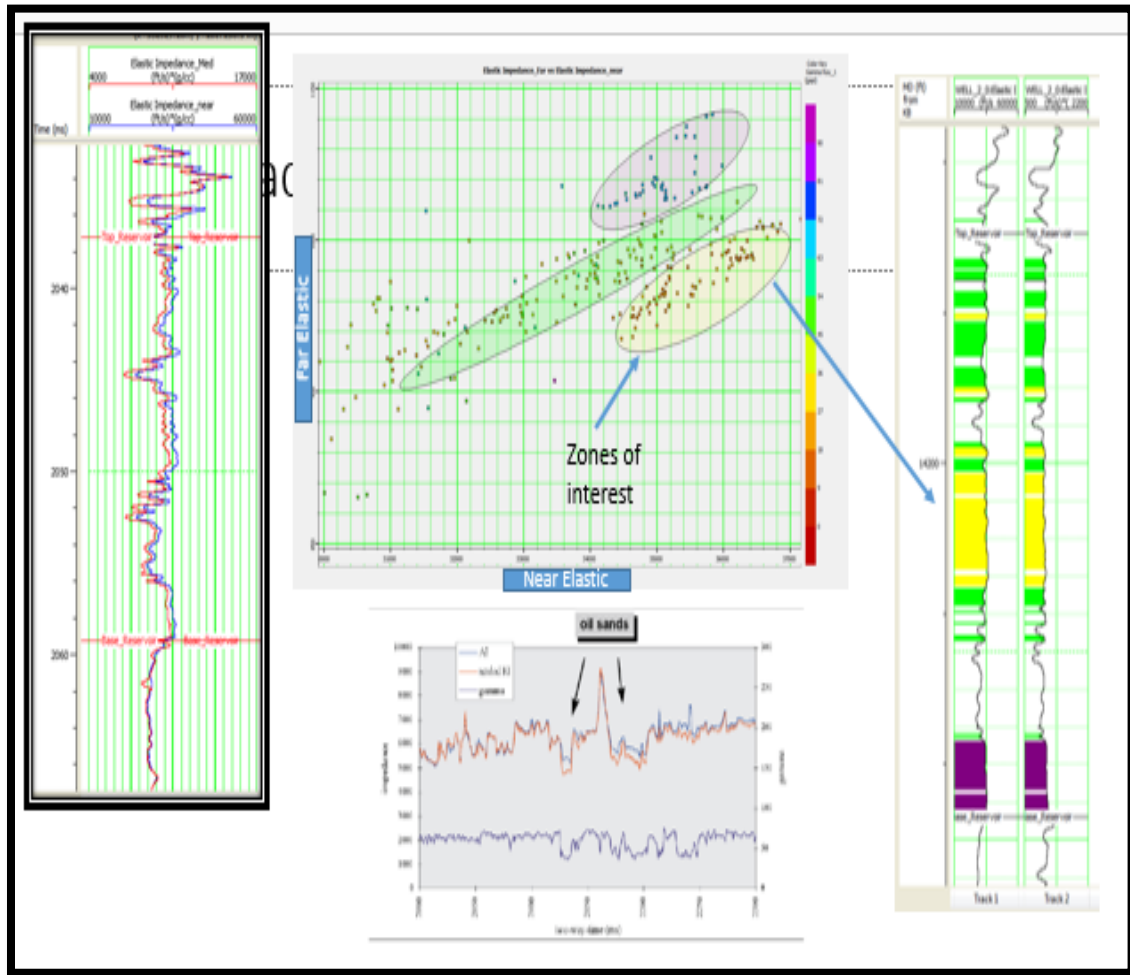
4.4 TABLES AND FIGURES

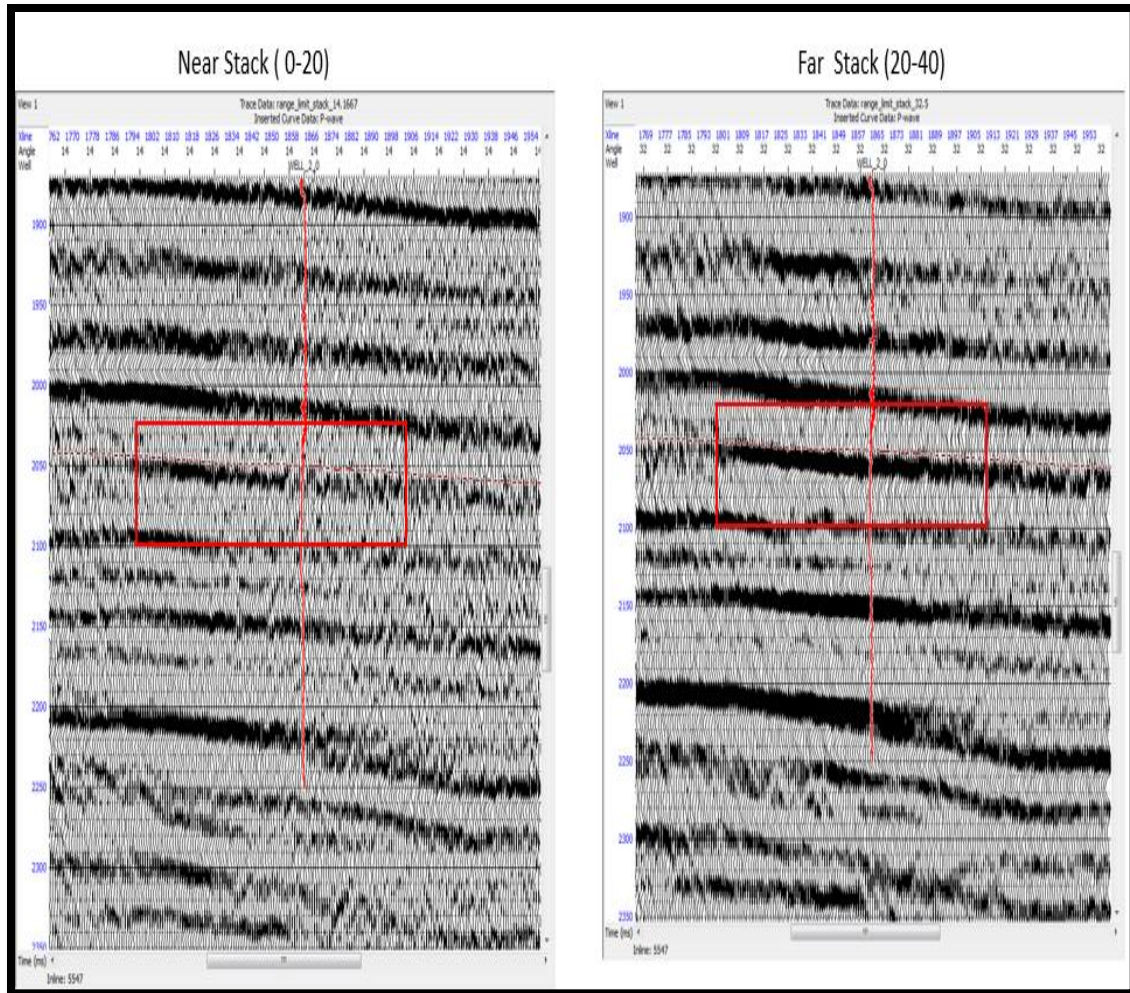Figure 4.1: Near and far elastic impedance from the logs
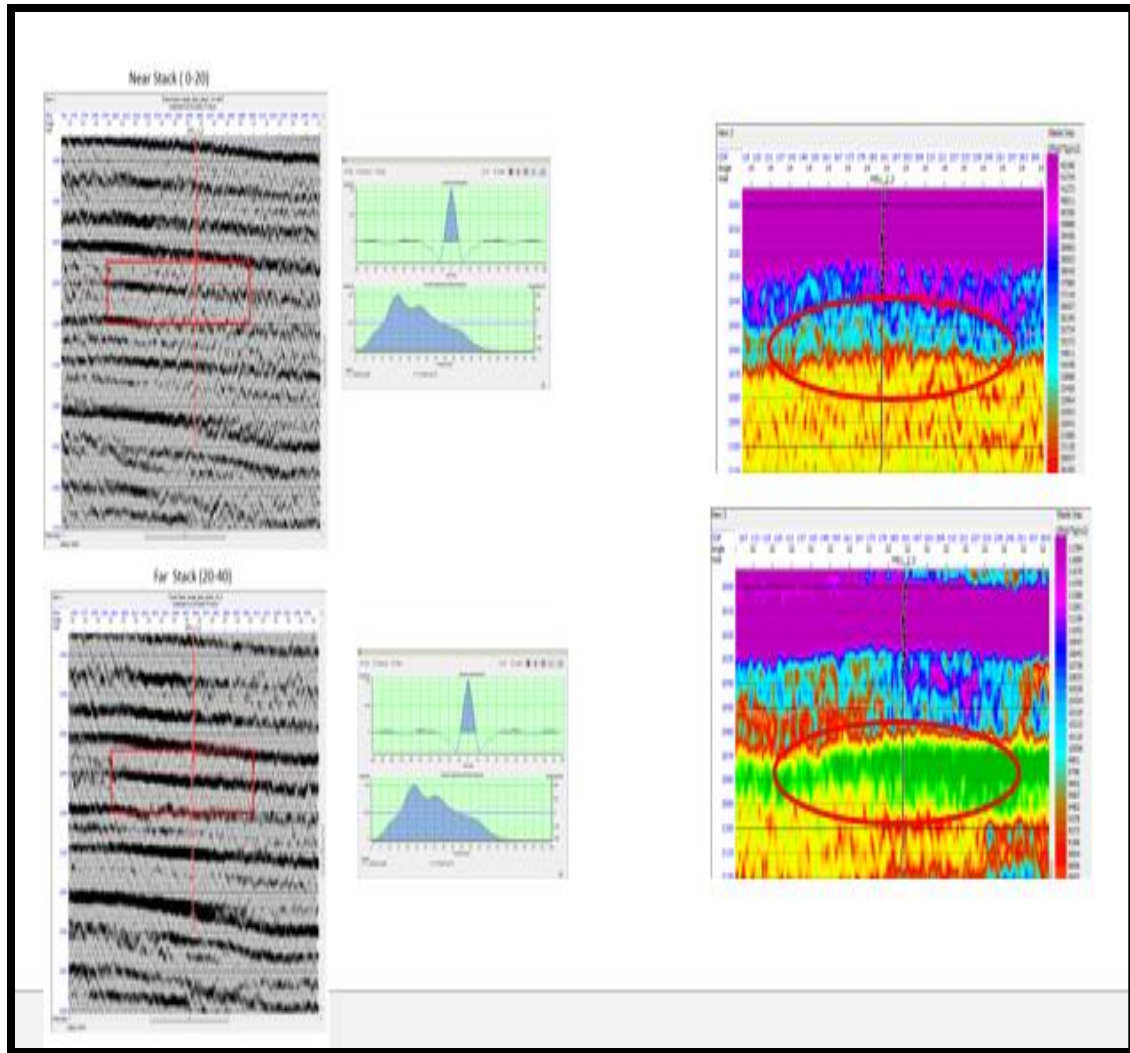
Figure 4.2: near and far seismic stacks.

Figure 4.3: Left: Near and far seismic stack, Middle: an extracted wavelet from each stack. Left: near and far elastic impedance.
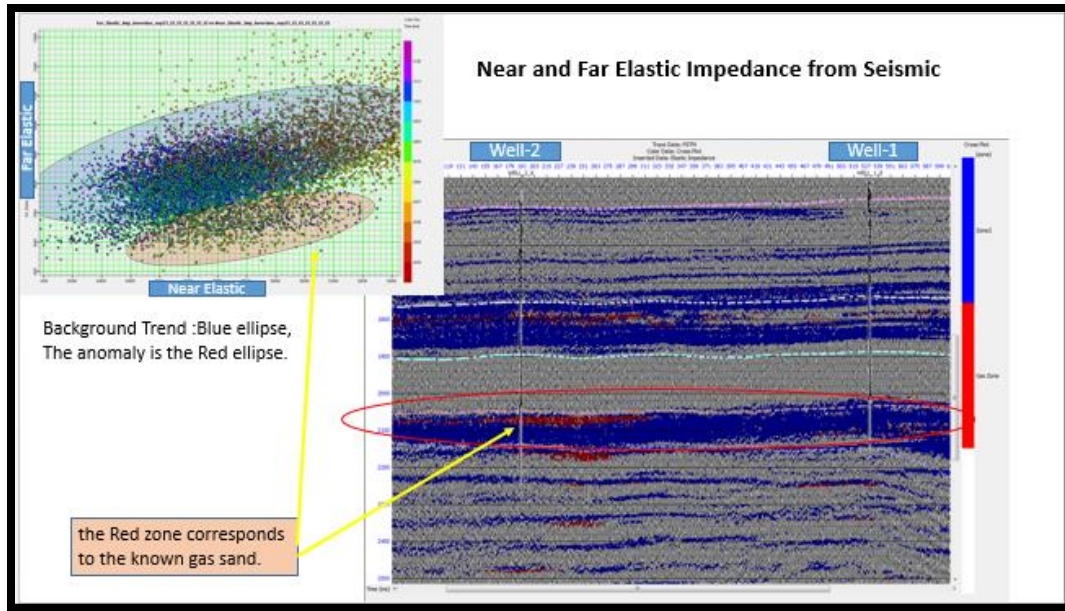
Figure 4.4: Left: Cross-plot of the far and near elastic impedance. Right the selected clusters are showing in the seismic.
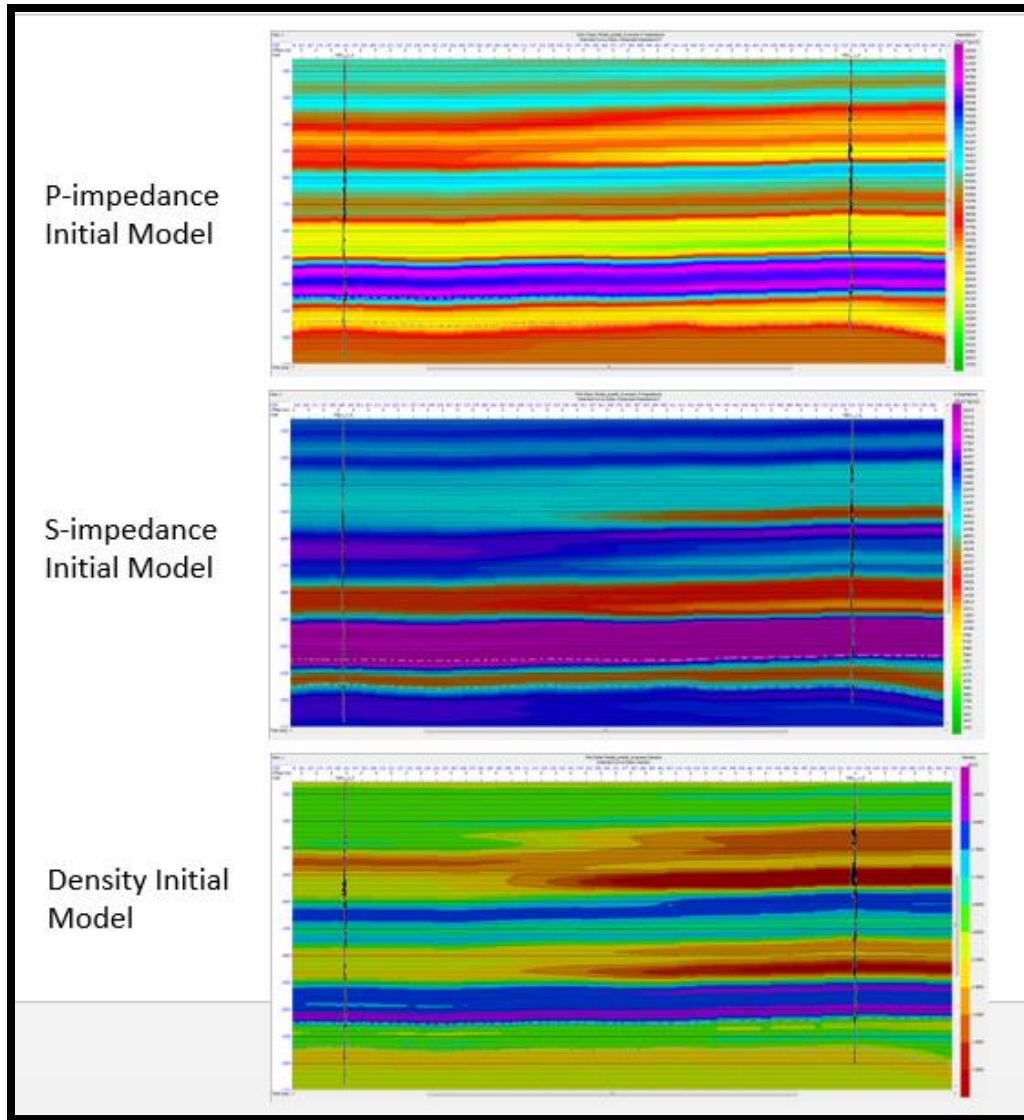
Figure 4.5: Initial models for the P-impedance, S-impedance, and density.
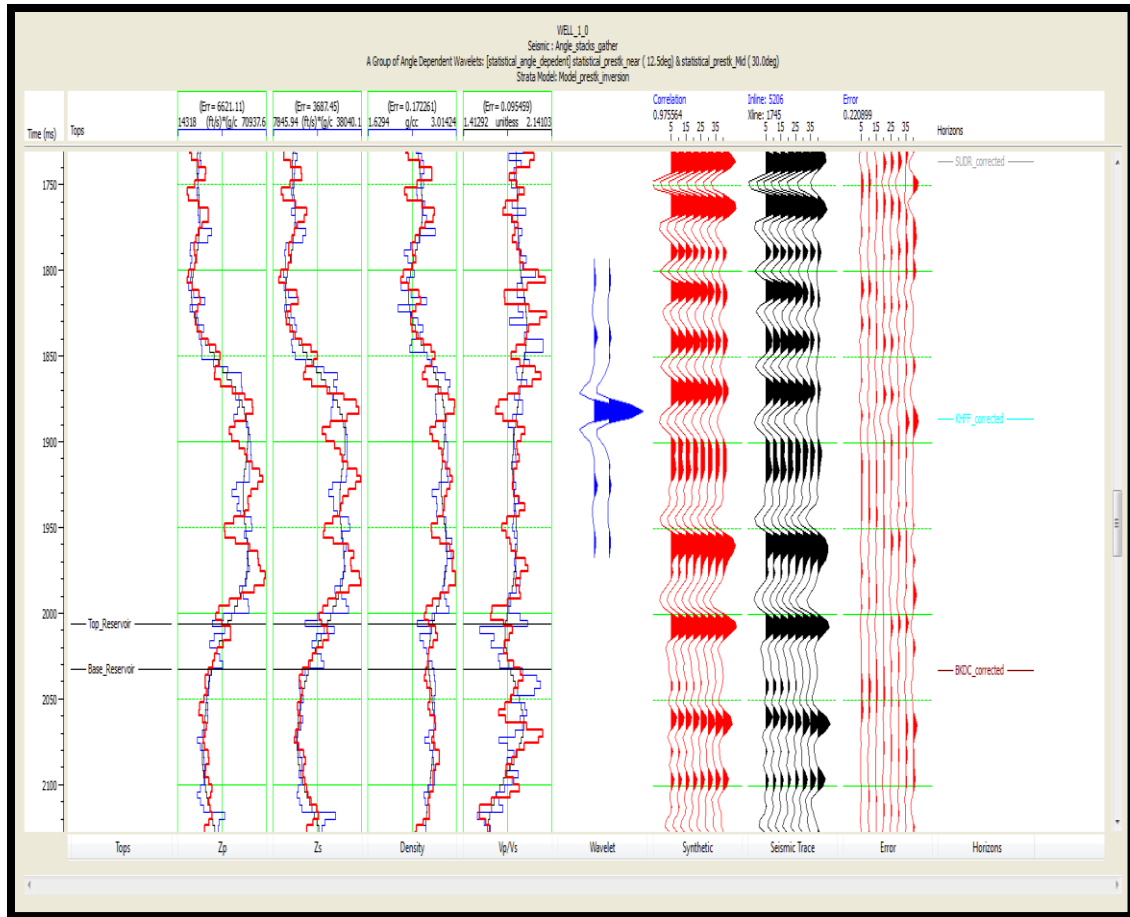
Figure 4.6: Inversion analysis at the well locations
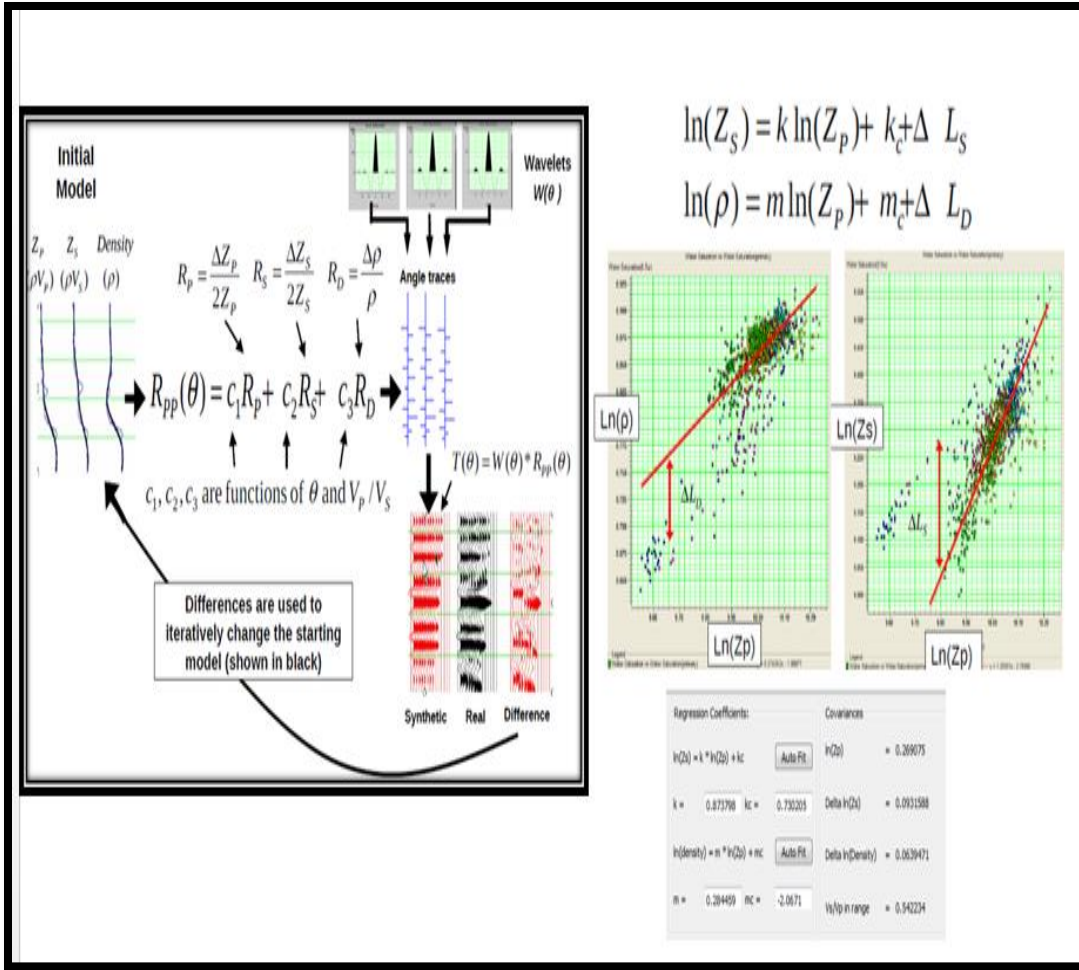
Figure 4.7: summarize workflow of the simultaneous inversion.
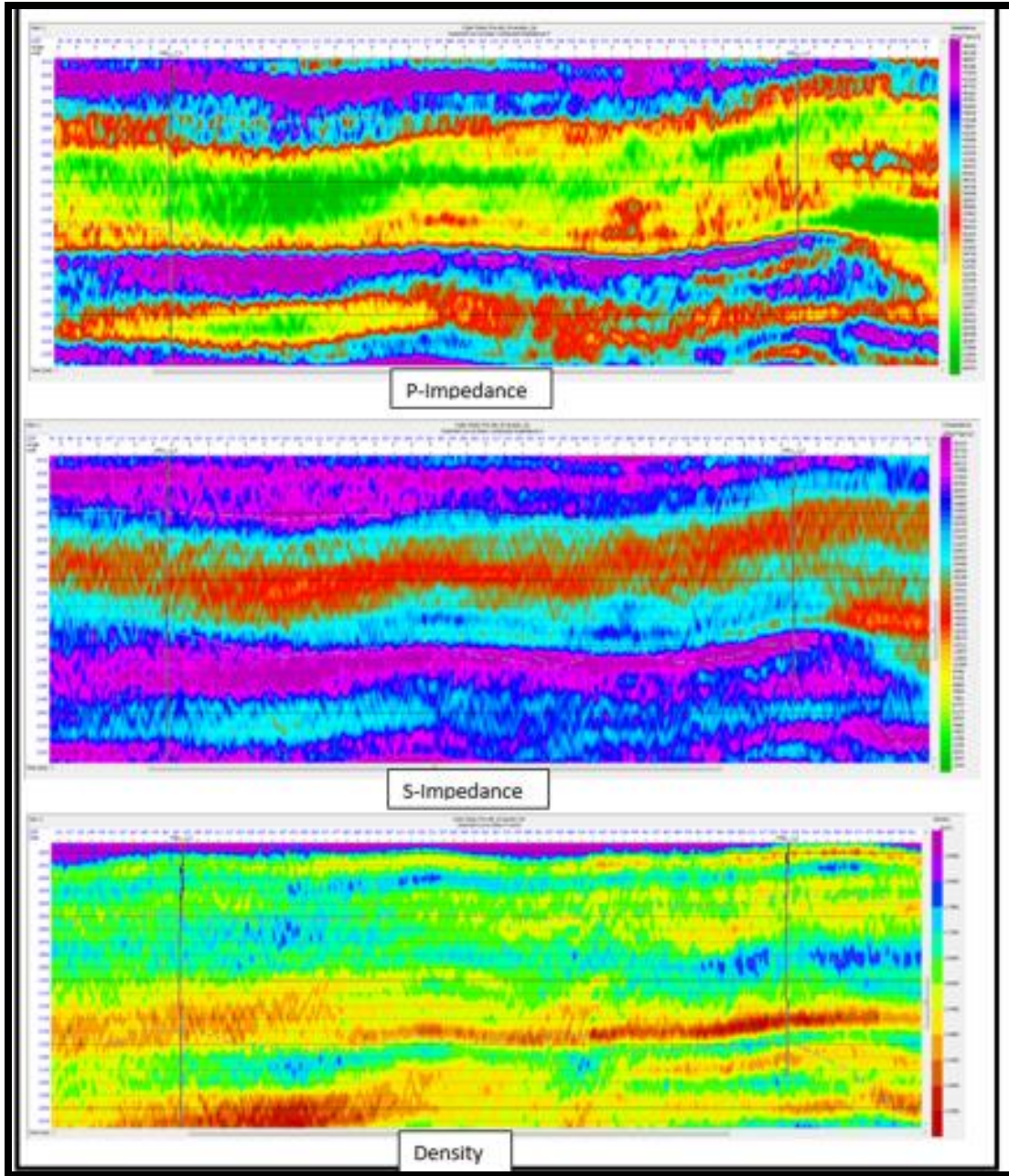
Figure 4.8: Simultaneous Inversion volumes
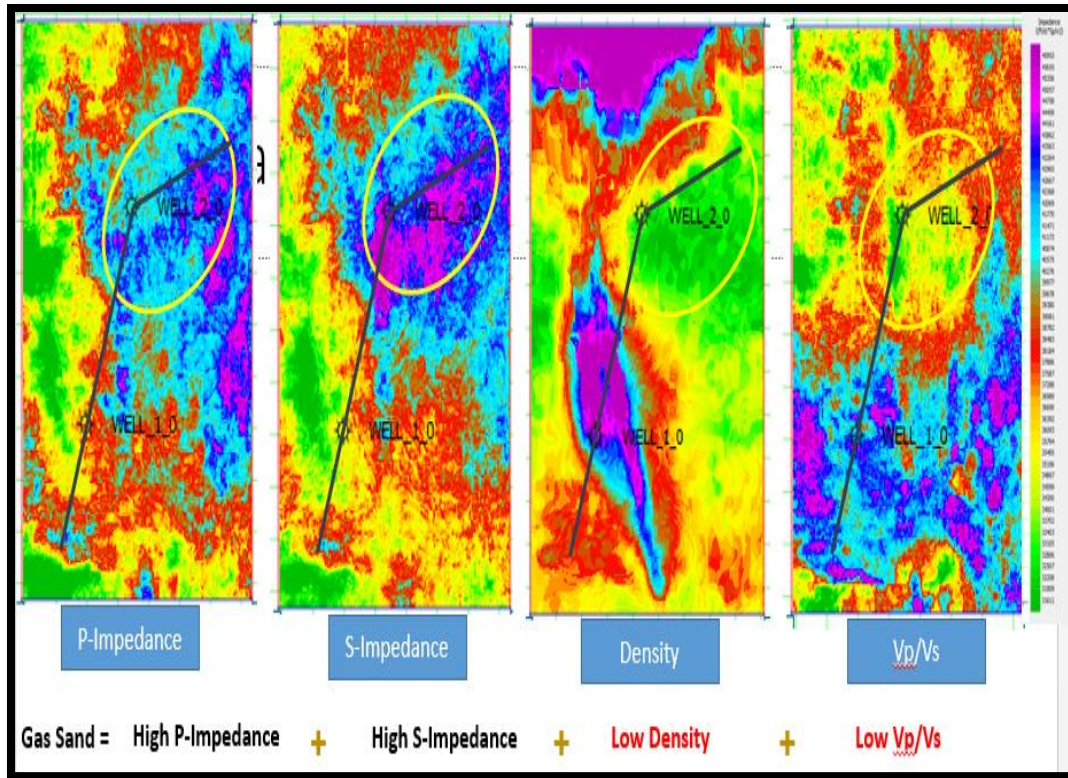
Figure 4.9: Data horizon slices from the simultaneous inversion volumes.
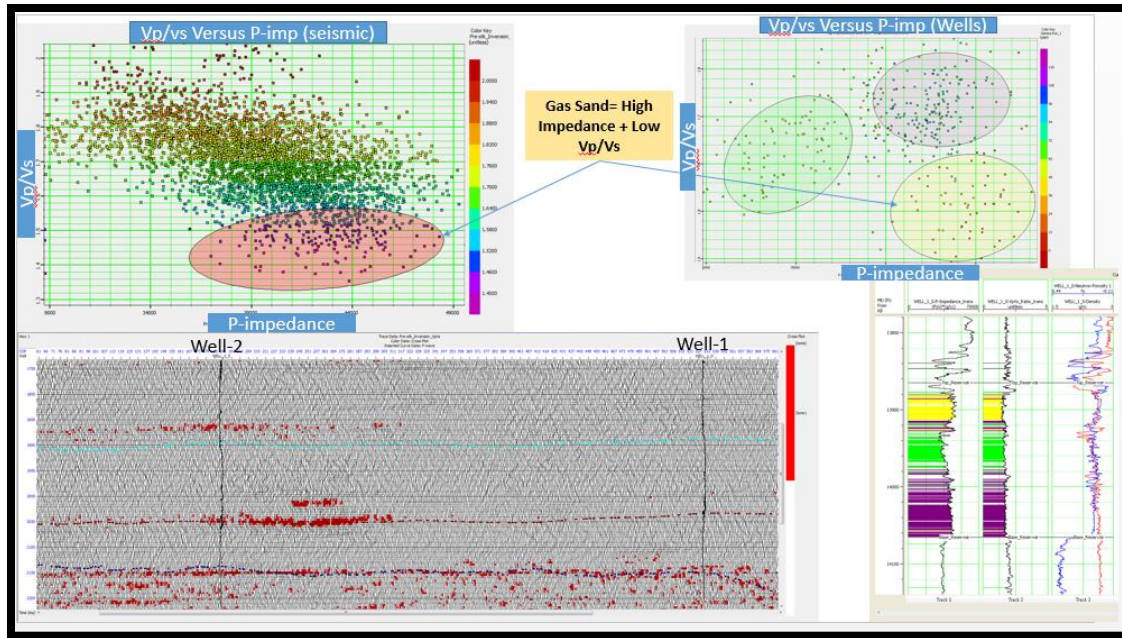
Figure 4.10: Vp/Vs versus P-impedance cross-plot from both wells and seismic. Both showed low Vp/Vs ratio and high P-impedance value at the excellent reservoir sand.

Figure 4.11: LMR volumes transformed from the P- and S- Impedance.

Figure 4.12: Lambda Vs Mu cross plot from well-2.

Figure 4.13: Lambda-Rho Vs Mu-Rho cross-plot from seismic and cross section showing the selected zones

CHAPTER 5

DISCUSSION AND CONCLUSION

In this research, Majhol field data (well-logs and seismic) have been investigated for hydrocarbon using cross-plot analysis, AVO modeling and analysis, Elastic inversion, and Simultaneous inversion methods.

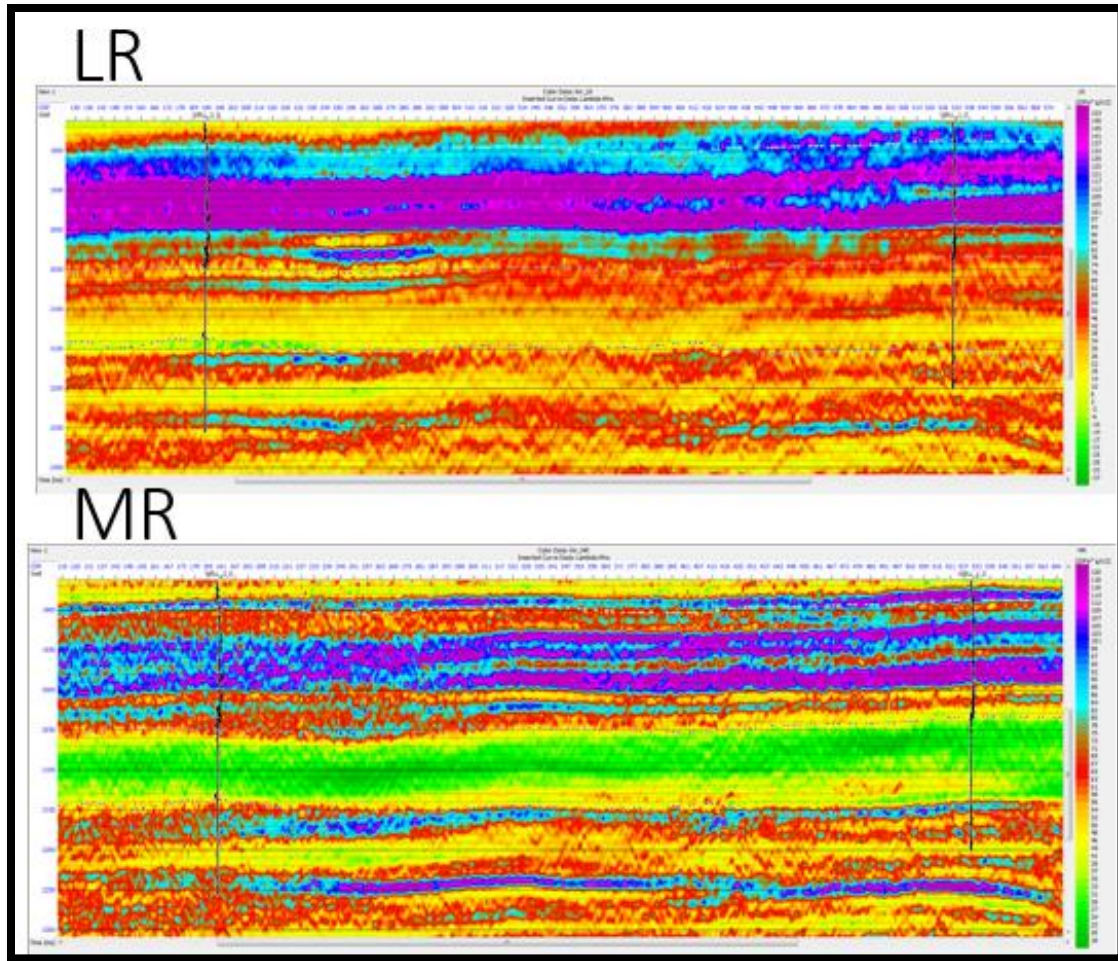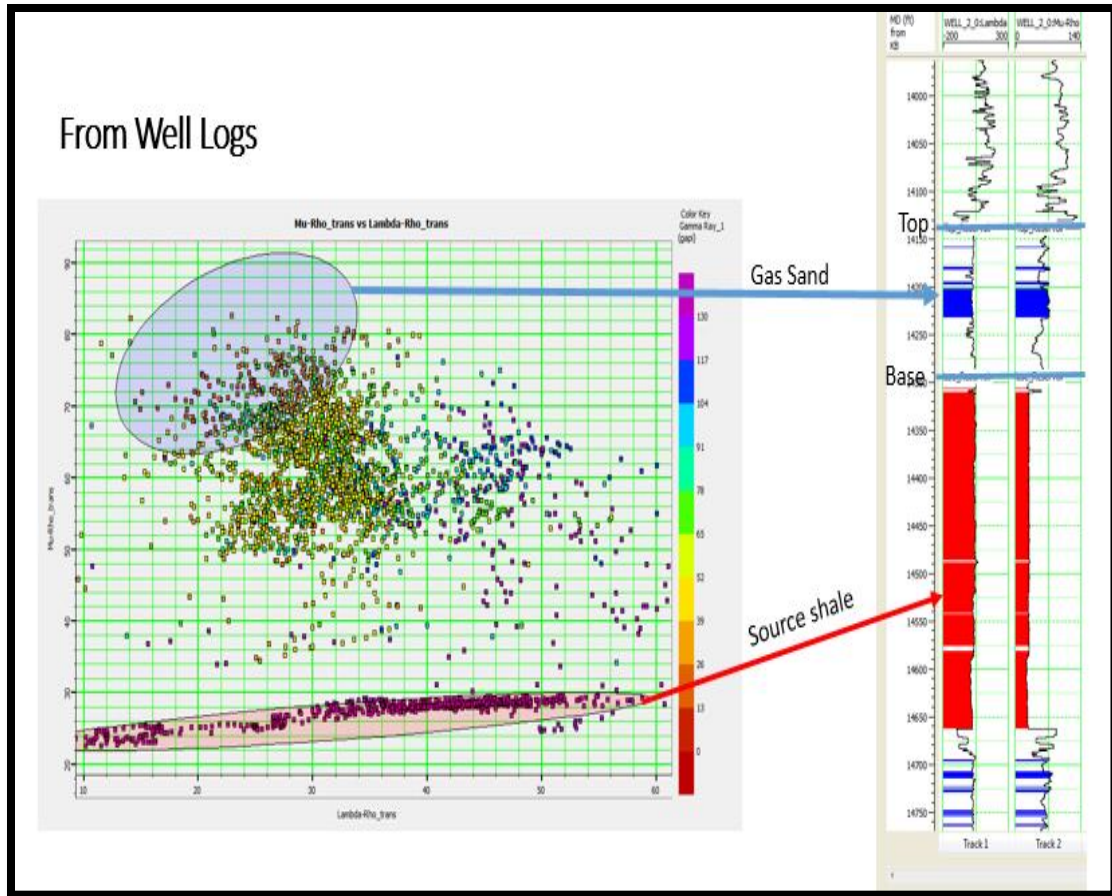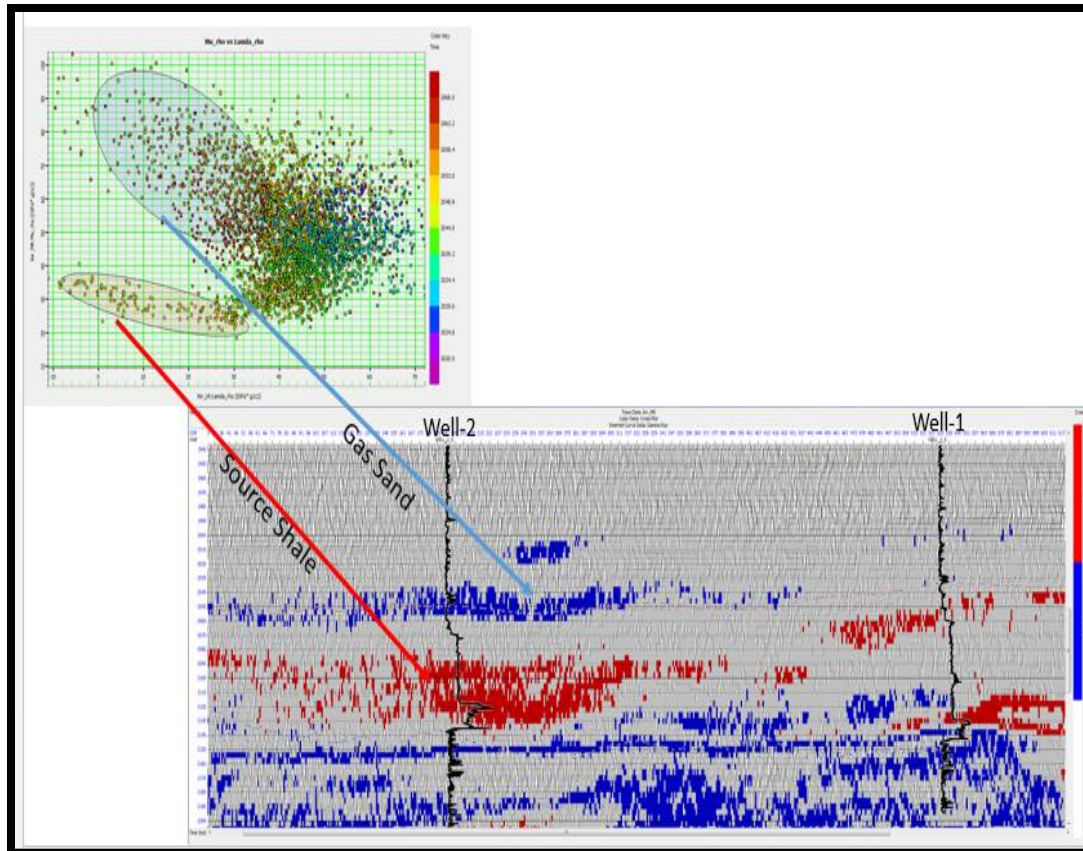The cross-plot analysis from wells assessed the discrimination between fluids and lithology effect in the area as well as the reservoir identification. The reservoir sand at well 1 has a gross thickness of 201 feet, net reservoir thickness of 17 feet, and average porosity 7 %.while the thickness of the gross reservoir at well-2 159 feet, net reservoir thickness of 95 ft , and average porosity 12% . The reservoir sand for both wells have three clear facies clusters that match the facies that were identified from the cores. (1) Aeolian sand dunes (2) Sand sheet sand (3) Sand intredune and playa.

The Aeolian sand dunes are characterized by low gamma ray, high impedance, high porosity, low Vp/Vs, and low lambda-Rho. Also the sand dune facies is considered to have the best reservoir quality and holding the gas. The sand sheet characterized by medium gamma ray, lower p-impedance, medium S-impedance, medium density and medium Vp/Vs values. The playa facies is siltstone characterized by high gamma ray, high p-impedance & S-impedance, high Vp/Vs, and high lambda-rho. Extracting information about the impedance alone was not enough to discriminate the facies since the sand dune facies and the playa siltstone facies has almost the same p-impedance. More elastic properties were important for outline the different facies. The cross-over

84

effect of the neutron porosity and density porosity logs indicates that the reservoir is a gas saturated sand. The acoustic impedance logs for both wells couldn't clearly differentiate the gas sands form the surrounding siltstone and shale; hence I cross-plotted other elastic properties Lambda-Rho vs Mhu-Rho and density vs Vp/Vs were the most effective elastic properties to distinguish the gas sand from other facies.

The fluid replacement modeling revealed how the reservoir properties change with different fluids. The addition of brine to the reservoir increases the p-impedance but slightly decreases the S-impedance. The AVO modeling for the gas scenario showed a decrease in amplitude with offset and changing the polarity. The result observed from the AVO modeling confirmed that Majhol reservoir has a class 2p AVO anomaly in which the reflection has a near-zero impedance with a positive amplitude that decreases and changes the polarity. When stacking the gathers, the reflections dimming out at the gas zones due to the cancelation of the near and far amplitude. Estimating the intercept (A) and the gradient (B) from the pre-stack seismic is another tool that were used in the cross-plotting and calculating the scaled Poisson's ratio (A+B) attribute both cross-plot and AVO attribute confirm the class 2p anomaly and outline the extension of the gas sand.

Elastic impedance inversion was carried out on the partial seismic stacks (near and far stacks). The far angle stack shows a bright amplitude at the reservoir and that is because of the construction amplitude that generated from base of the reservoir. Those reflection stacks were inverted separately by building initial model and statistical wavelet for each one. A near and far impedance volume was generated and cross-plotted against each other's. The gas zone showed a deviation of the gas sand cluster from the background trend in the cross-plot.

Simultaneous inversion was run on the angle stack to generate P-impedance, S-impedance, and density volumes that were directly compared to the well logs. Simultaneous inversion helped to delineate reservoir using sonic log obtained after the seismic to well tie and also mapped horizons from the 3D interpretation. Initial low frequency model was built prior to inverting the whole seismic data, as this was required because of the disparity in frequency contents for well-log and seismic data. Inversion analysis carried out showed a good fit between inverted logs and basic logs, the inversion was then carried out to generate the different volumes that were used in the interpretation by cross-plot them against each other and making horizon slices with average time window of 20 ms bellow and above.

P-impedance and S-impedance volumes were used to calculate the lambda-Rho and Mu-Rho volumes too. In general, the log and seismic were correlated and showed the same properties for the good reservoir. The thick gas sand is extended around well-2 and doesn't extend all the way to well-1. The extension of the reservoir would never be detected without making such advance investigation on the pre-stack seismic.

REFERENCES

Aki, K., and Richards, P. G. (1980), Quantitative Seismology, 932.

Asquith, G. B., Krygowski, D., and Gibson, C. R. (2004), Basic well log analysis (Vol. 16). Tulsa: American Association of Petroleum Geologists.

Castagna, J. P., and Swan, H. W. (1997), Principles of AVO crossplotting. The leading edge, 16(4), 337-344.

Castagna, J. P., Swan, H. W., and Foster, D. J. (1998), Framework for AVO gradient and intercept interpretation. Geophysics, 63(3), 948-956.

Connolly, P. (1999). Elastic impedance. The Leading Edge, 18(4), 438-452.

Darling, T. (2005). Well logging and formation evaluation. Elsevier.

Foster, D. J., Keys, R. G., and Lane, F. D. (2010), Interpretation of AVO anomalies. Geophysics, 75(5), 75A3-75A13.

Goodway, B., Chen, T., and Downton, J. (1997), Improved AVO Fluid Detection And Lithology Discrimination Using Lamé Petrophysical Parameters;"λρ" μρ λμ Fluid Stack" From P And S Inversions. In 1997 SEG Annual Meeting

Halliburton Course Notes(2001), Basic petroleum geology and log analysis, 87 p.

Konert, G., Afifi, A.M., Al-Hajri, S.A., and Droste, H.J. (2001), Paleozoic stratigraphy and hydrocarbon habitat of the Arabian Plate: GeoArabia, v. 6, p. 407–442.

Larionov, V. V. (1969), Borehole Radiometry. Nedra, Moscow.

Liner, C. L. (2004), Elements of 3D Seismology (2ndedition): PennWell Corporation, 608 p.

Ostrander, W. (1984), Plane-wave reflection coefficients for gas sands at nonnormal angles of incidence. Geophysics, 49(10), 1637-1648.

Pollastro, R. M., and Geological Survey (U.S.) (2003), Total petroleum systems of the Paleozoic and Jurassic, Greater Ghawar Uplift and adjoining provinces of Central Saudi

Arabia and Northern Arabian-Persian Gulf (Version 1.0.). [Reston, Va.]: U.S. Dept. of the Interior, U.S. Geological Survey.

Russell, B. (2005), Strata workshop: Theory and exercises in seismic inversion and AVO, unpublished lecture notes.

Russell, B., and Hampson, D. (1999), AVO theory, Hampson-Russell software services limited, 69 p.

Russell, B., and Hampson, D. (2006), The old and the new in seismic inversion: CSEG Recorder, 5-11.

Rutherford, S.R., and Williams, R.H. (1989), Amplitude versus offset variations in gas sands, Geophysics, Vol. 54, No. 6, 680 - 688.

Senalp, M., and Al-Duaiji, A.(1995), Stratigraphy and sedimentation of the Unayzah reservoirs, Central Saudi Arabia, in Al-Husseini, M.I., ed., Geo-94, Middle East Petroleum Geosciences Conference: Gulf Petrolink, Manama, Bahrain,v. 1, p. 837–847.

Sheriff, R. E. (2002), Encyclopedic Dictionary of Applied Geophysics (4th edition), SEG, 429

Shuey, R. T. (1985), A simplification of the Zoeppritz equations. Geophysics, 50(4), 609-614.

Veeken, P. C. H. (2007), Seismic stratigraphy, basin analysis and reservoir characteristics, in Helberg, K., and Treitel, S., eds., Handbook of Geophysical Exploration, Seismic Exploration Vol. 37, 509 p.

Zeigler, M.A. (2001), Late Permian to Holocene paleofacies evolution of the Arabian Plate and its hydrocarbon occurrence: GeoArabia, v. 6, p. 445–504.